

LEO SATELLITES: ATTITUDE DETERMINATION AND  
CONTROL COMPONENTS ; SOME LINEAR ATTITUDE  
CONTROL TECHNIQUES

A THESIS SUBMITTED TO  
THE GRADUATE SCHOOL OF NATURAL AND APPLIED  
SCIENCES  
OF  
MIDDLE EAST TECHNICAL UNIVERSITY

BY

CEREN KAPLAN

IN PARTIAL FULFILLMENT OF THE REQUIREMENTS  
FOR  
THE DEGREE OF MASTER OF SCIENCE  
IN  
ELECTRICAL AND ELECTRONICS ENGINEERING

APRIL 2006

Approval of Graduate School of Natural and Applied Sciences

\_\_\_\_\_  
Prof. Dr. Canan ÖZGEN  
Director

I certify that this thesis satisfies all the requirements as a thesis for the degree of Master of Science.

\_\_\_\_\_  
Prof. Dr. İsmet ERKMEN  
Head of Department

We certify that we have read this thesis and that in our opinion it is fully adequate, in scope and quality, as a thesis for the degree of Master of Science.

\_\_\_\_\_  
Prof. Dr. Erol KOCAOĞLAN  
Supervisor

**Examining Committee Members**

Prof. Dr. Mübeccel DEMİREKLER (METU, EEE) \_\_\_\_\_

Prof Dr. Erol KOCAOĞLAN (METU, EEE) \_\_\_\_\_

Prof Dr. Kemal LEBLEBİCİOĞLU (METU, EEE) \_\_\_\_\_

Prof. Dr. Aydan ERKMEN (METU, EEE) \_\_\_\_\_

Gökhan YÜKSEL (M.Sc) (TÜBİTAK , BİLTEN) \_\_\_\_\_

**I hereby declare that all information in this document has been obtained and presented in accordance with academic rules and ethical conduct. I also declare that, as required by these rules and conduct, I have fully cited and referenced all material and results that are not original to this work.**

Name, Last name : Ceren KAPLAN

Signature :

## **ABSTRACT**

### **LEO SATELLITES: ATTITUDE DETERMINATION AND CONTROL COMPONENTS ; SOME LINEAR ATTITUDE CONTROL TECHNIQUES**

Kaplan, Ceren

M.Sc., Department of Electrical and Electronics Engineering

Supervisor: Prof. Dr. Erol Kocaođlan

April 2006, 129 pages

In this thesis, application of linear control methods to control the attitude of a Low-Earth Orbit satellite is studied. Attitude control subsystem is first introduced by explaining attitude determination and control components in detail. Satellite dynamic equations are derived and linearized for controller design. Linear controller and linear quadratic regulator are chosen as controllers for attitude control. The actuators used for control are reaction wheels and magnetic torquers. MATLAB-SIMULINK program is used in order to simulate satellite dynamical model (actual nonlinear model) and controller model. In simulations, the satellite parameters are selected to be similar to the actual BILSAT-1 satellite parameters. In conclusion, simulations obtained from different linear control methods are compared within themselves and with nonlinear control methods, at the same time with that obtained from BILSAT-1 satellite log data.

Key Words: Low-Earth Orbit Satellite, Attitude Determination and Control Components, Linear Controller, Linear Quadratic Regulator.

# ÖZ

## ALÇAK YÖRÜNGE UYDULARI: KONUM BELİRLEME VE DENETLEME ELEMANLARI ; BAZI DOĞRUSAL KONUM DENETLEME TEKNİKLERİ

Kaplan, Ceren

Yüksek Lisans, Elektrik –Elektronik Mühendisliği Bölümü

Tez Yöneticisi : Prof. Dr. Erol Kocaođlan

Nisan 2006, 129 sayfa

Bu tezde alçak yörünge Dünya uydusunun davranış hareketini denetlemek amacıyla doğrusal denetim yöntemlerinin uygulanması üzerinde çalışılmıştır. İlk olarak, davranış denetim alt sistemi, davranış belirleme ve denetim elemanları detaylı bir şekilde anlatılarak tanıtılmıştır. Denetleyici tasarımı için, uydunun dinamik denklemleri çıkarılmış ve doğrusallaştırılmıştır. Davranış denetimi için doğrusal denetleyici ve doğrusal kuadratik regülatör denetleyiciler olarak seçilmiştir. Denetimi sağlamak amacıyla tetikleyici olarak reaksiyon tekerleri ve manyetik tork vericiler kullanılmıştır. Uydunun dinamik (asıl doğrusal olmayan model) ve denetleyici modellenmesi MATLAB-SIMULINK programı kullanılarak gerçekleştirilmiştir. Simülasyonlarda kullanılan uydu modelinin özellikleri gerçek BİLSAT-1 uydu parametreleri ile benzer olacak şekilde seçilmiştir. Sonuç olarak, farklı denetim yöntemlerinden elde edilen simülasyonlar birbirleriyle ve doğrusal olmayan denetim yöntemleriyle, aynı zamanda BİLSAT-1 uydu kayıt bilgisinden elde edilen verilerle karşılaştırılmıştır.

Anahtar Kelimeler: Düşük Yörünge Dünya Uydusu, Davranış Belirleme ve Denetim Elemanları, Doğrusal Denetleyici, Doğrusal Kuadratik Regülatör.

***TO MY WONDERFUL FAMILY***

***&***

***MY FRIENDS***

## **AKNOWLEDGEMENTS**

The author wishes to express her deepest gratitude to her supervisor Prof. Dr. Erol Kocaođlan and Gökhan Yüksel (M.Sc., Tübitak, Bilten) for their guidance, advice, criticism, encouragements and insight throughout the research.

# TABLE OF CONTENTS

<b>PLAGIARISM .....</b>	<b>iii</b>
<b>ABSTRACT .....</b>	<b>iv</b>
<b>ÖZ.....</b>	<b>v</b>
<b>DEDICATION .....</b>	<b>vi</b>
<b>ACKNOWLEDGEMENTS.....</b>	<b>vii</b>
<b>TABLE OF CONTENTS.....</b>	<b>viii</b>
<b>LIST OF TABLES .....</b>	<b>xiv</b>
<b>LIST OF FIGURES .....</b>	<b>xv</b>

## CHAPTERS

<b>1. INTRODUCTION.....</b>	<b>1</b>
1.1 Low Earth Orbit Satellites and BILSAT-1 Attitude Determination and Control Subsystem .....	1
1.2 Previous Background .....	8
1.3 Scope of This Thesis .....	12
1.4 Outline of The Thesis.....	13
<b>2. ATTITUDE DETERMINATION AND CONTROL COMPONENTS .....</b>	<b>14</b>
2.1 Attitude Sensors .....	15
2.1.1 Sun Sensors .....	16

2.1.1.1	Analog Sensors .....	16
2.1.1.2	Sun Presence Sensors.....	19
2.1.1.3	Digital Sensors .....	20
2.1.2	Horizon Sensors .....	24
2.1.2.1	Sensor Components.....	26
2.1.3	Magnetometers.....	29
2.1.3.1	Sensor Components.....	30
2.1.4	Star Sensors.....	32
2.1.4.1	Sensor Components.....	33
2.1.4.2	Sensor Types .....	34
2.1.5	Rate Sensors (Gyroscopes) .....	36
2.1.5.1	Sensor Types .....	38
2.2	Attitude Actuators .....	42
2.2.1	Momentum and Reaction Wheels .....	42
2.2.1.1	Momentum Wheels .....	43
2.2.1.2	Reaction Wheels .....	44
2.2.2	Magnetic Torquers .....	50
2.2.3	Gravity Gradient Boom.....	52
2.2.4	Gas Jets .....	53
2.3	Summary .....	54

### 3. ATTITUDE DYNAMICS AND SOME LINEAR CONTROL

<b>TECHNIQUES</b> .....	<b>55</b>
3.1 Mathematical Definitions .....	55
3.1.1 Keplerian Orbits .....	55
3.1.2 Reference Frames .....	57
3.1.2.1 Earth-Centered Inertial (ECI) Frame .....	57
3.1.2.2 Earth-Centered Earth Fixed (ECEF) Frame .....	58
3.1.2.3 Earth-Centered Orbit Frame .....	58
3.1.2.4 Orbit Frame .....	58
3.1.2.5 Body Frame .....	59
3.2 Attitude Representation .....	59
3.2.1 Representing Attitude Information .....	59
3.2.1.1 Euler Angle Representation .....	60
3.2.1.2 Unit Quaternions .....	61
3.3 Rotation Matrix .....	61
3.3.1 Transformation Between Different Frames .....	63
3.3.1.1 Transformation from Earth-Centered Orbit to ECI and ECEF Frame .....	63
3.3.1.2 Transformation from ECEF to ECI Frame .....	63
3.3.1.3 Transformation from ECI to Orbit Frame .....	64
3.3.1.4 Transformation from Orbit to Body Frame .....	65
3.4 Inertia Matrix .....	65
3.5 Modelling the Earth's Magnetic Field .....	66

3.5.1	The Earth's Magnetic Field.....	67
3.5.1.1	Mathematical Model .....	67
3.5.1.2	IGRF Model .....	68
3.5.1.3	Dipol Model .....	68
3.6	Modelling Environmental and Actuator Torques .....	69
3.6.1	Mathematical Models for Environmental Disturbance Torques.....	70
3.6.1.1	Gravity Gradient Torque .....	71
3.6.1.2	Solar Radiation Pressure .....	72
3.6.1.3	Aerodynamic Drag.....	73
3.6.1.4	Magnetic Disturbance Torque.....	74
3.6.2	Reaction Wheel Torque .....	75
3.7	General Mathematical Modelling of a Satellite .....	82
3.7.1	Dynamic Model of a Satellite .....	82
3.7.2	Kinematics for Satellite Model .....	84
3.8	Linearization of Mathematical Model.....	85
3.8.1	Linearization of Kinematic Equations .....	85
3.8.2	Rotation Matrix Linearization.....	86
3.8.3	Angular Velocity Linearization.....	86
3.8.4	Linearization of Gravitational Torque .....	87
3.8.5	Magnetic Torquer Linearization .....	87
3.8.6	Linearization of the Reaction Wheel .....	87
3.8.7	Linearization of the Satellite Mathematical Model with	

Magnetic Torquer as Actuator .....	88
3.8.8 Linearization of the Satellite Mathematical Model with Reaction Wheel as Actuator.....	89
3.9 Some Linear Control Techniques Applied for Attitude Control.....	90
3.9.1 Attitude Control .....	90
3.9.2 Some Linear Control Techniques .....	92
3.9.2.1 Controllability .....	92
3.9.2.2 Linear Controller.....	93
3.9.2.3 Linear Quadratic Regulator.....	95
3.10 Summary .....	97
<b>4. SIMULATION RESULTS.....</b>	<b>98</b>
4.1 Satellite Model with Magnetic Torquers as Actuators.....	99
4.2 Satellite Model with Reaction Wheels as Actuators .....	100
4.3 Simulation Results with Reaction Wheels as Actuators .....	101
4.3.1 Linear Controller.....	101
4.4 Simulation Results with Magnetic Torquers as Actuators.....	115
4.3.1 Linear Quadratic Regulator.....	115
4.5 Sensitivity Analysis.....	119
<b>5. CONCLUSION AND FUTURE WORK .....</b>	<b>123</b>
<b>REFERENCES.....</b>	<b>127</b>

<b>APPENDIX A</b> .....	<b>130</b>
<b>APPENDIX B</b> .....	<b>149</b>
<b>APPENDIX C</b> .....	<b>156</b>
<b>APPENDIX D</b> .....	<b>174</b>

## LIST OF TABLES

Table 2.1 : Reference Sources Used in Attitude Determination.....	15
Table 2.2 : Typical Performance Ranges and Technical Properties of Sensors ....	41
Table 2.3 : The Accuracy of Different Types of Sensors .....	41
Table 2.4 : Typical Actuators and Their Technical Properties .....	54
Table 4.1: BILSAT-1 Satellite Properties.....	98
Table 4.2 : Initial Values of the Parameters.....	102
Table 4.3 : Command Table for BILSAT-1.....	113
Table 4.4 : Initial Values of the Parameters.....	115
Table 4.5 : Sensitivity of the System Response to Control Parameter Changes for Linear Quadratic Regulator.....	121
Table 4.6 : Sensitivity of the System Response to Control Parameter Changes for Linear Controller.....	122
Table 4.7 : Comparison of the System Response for Different Control Methods.	125

## LIST OF FIGURES

Figure 1.1 : BILSAT Satellite Launched on Sept. 27,2003 .....	2
Figure 1.2 : ADCS Block Diagram of BILSAT-1 .....	4
Figure 1.3 : Four Wheels in a Tetrahedral Configuration.....	4
Figure 1.4 : Illustration of 30 Degree Slewing About Pitch Axis.....	5
Figure 1.5 : Propulsion System on the Satellite .....	6
Figure 1.6 : SSTL Altair HB Star Camera (Processing Unit and Camera Head) ..	7
Figure 1.7 : MEMS Gyros as Rate Sensors .....	7
Figure 1.8 : The SSTL SGR-20 GPS Receiver Determines the Attitude with .....	
Position Information .....	8
Figure 2.1 : Cosine Detector Sun Sensor .....	17
Figure 2.2 : Two Cosine Detectors Combined to Provide Wide Sun Angle.....	
Measurement Range .....	18
Figure 2.3 : Summation of the Outputs from Two Sensors . The Solid.....	
Line Represents the Summed Output .....	18
Figure 2.4 : Simple Shadow Bar Sun Sensor .....	19
Figure 2.5 : Two Slit Sun Presence Detector .....	19
Figure 2.6 : Sun Angle as a Function of Spin Angle for Typical Solar.....	
V-Beam Sensor with 45-Deg Tilt .....	20
Figure 2.7 : A Simple Digital Sensor .....	21
Figure 2.8 : Field of View of Sun Sensor Command Component .....	21
Figure 2.9 : Sun Sensor Measurement Component Detail and Output .....	22
Figure 2.10 : Plot of Output From Photocells Versus Sun Angele for Adcole.....	
Digital Sensor .....	23
Figure 2.11 : Barnes 13-517 Sun Sensor.....	24
Figure 2.12 : Barnes 13-470-RH Horizon Sensor and Technical Properties .....	25
Figure 2.13 : Ithaco Horizon Crossing Indicator .....	25
Figure 2.14 : Ithaco Type Scanwheel Model .....	26
Figure 2.15 : SEASAT Scanwheel Operating Principle .....	27

Figure 2.16 : Output of Scanning Horizon Sensor .....	28
Figure 2.17 : Generalized Magnetometer Block Diagram .....	30
Figure 2.18 : Dual-Core Fluxgate Magnetometer with Primary and Secondary Induction Coils. ....	30
Figure 2.19 : Fluxgate Magnetometer Operating Principle and Output .....	
Configurations .....	32
Figure 2.20 : Simplified Version of a Star Sensor Hardware .....	33
Figure 2.21 : Gimbaled Star Sensor .....	35
Figure 2.22 : A Cutaway Diagram of a Fixed-Head Star Tracker .....	35
Figure 2.23 : Different Types of Star Trackers and Characteristics of These.....	
Sensors .....	36
Figure 2.24 : Basic Single-Degree-of-Freedom Gyroscope Construction.....	
Geometry .....	37
Figure 2.25 : Configuration of Control Moment Gyros in Three Axes .....	40
Figure 2.26 : Different IMU Configurations and Their Technical Data .....	40
Figure 2.27 : A Typical Momentum Wheel Configuration.....	43
Figure 2.28 : Typical Reaction Wheel Configuration.....	45
Figure 2.29 : Ithaco Type Reaction Wheel Configuration and Physical.....	
Properties .....	45
Figure 2.30 : Typical Tetrahedral Configuration of Reaction Wheels.....	46
Figure 2.31 : A Slew Rotation about z Axis in the Inertial Space: x axis has .....	
to absorb additional momentum when moving to its location at $t_2$ ....	47
Figure 2.32 : Duty Cycle, $X_{dc}$ , as a Function of Control Voltage, $V$ .....	48
Figure 2.33 : Applied Torque as a Function of Wheel Speed.....	49
Figure 2.34 : Magnetic Torquer with Resultant Force Vector .....	52
Figure 2.35 : SSTL Weitzman GM Deployable Boom.....	52
Figure 2.36 : Cold Gas Jet.....	53
Figure 3.1 : Configuration of Kepler's First Law .....	56
Figure 3.2 : Configuration of Kepler's Second Law .....	56
Figure 3.3 : Configuration of Kepler's Third Law.....	57
Figure 3.4 : The Body and Orbit Reference Frames .....	59

Figure 3.5 : The Distribution of Earth’s Magnetic Field .....	67
Figure 3.6 : Disturbance Torques as a Function of Altitude .....	70
Figure 3.7 : Example for the Tetrahedral Configured Reaction Wheels.....	76
Figure 4.1 : Generalized Satellite Model with Magnetic Torquer .....	99
Figure 4.2 : Generalized Satellite Model with Reaction Wheels.....	100
Figure 4.3 : Satellite Euler Angles and Angular Velocity in the Body Frame.....	103
Figure 4.4 : Outputs of the Reaction Wheels And Regulator .....	104
Figure 4.5 : Satellite Desired Euler Angles and Angular Velocity with.....	
Noise Effect.....	105
Figure 4.6 : Outputs from the Regulator and Reaction Wheels with .....	
Noise Effect.....	106
Figure 4.7 : Satellite Desired Euler Angles and Angular Velocity When .....	
Wheel 2 is Disabled .....	107
Figure 4.8 : Outputs from the Regulator and Reaction Wheels When .....	
Wheel 2 is Disabled .....	108
Figure 4.9 : Satellite Euler Angles and Angular Velocity When Wheel .....	
2 and 3 are Disabled.....	109
Figure 4.10 : Outputs from the Regulator and Reaction Wheels When Wheel.....	
2 and 3 are Disabled.....	110
Figure 4.11 : Satellite Euler Angles and Angular Velocity with .....	
Pitch Angle= $30^0$ .....	111
Figure 4.12 : Outputs of the Regulator and Reaction Wheels with .....	
Pitch Angle = $30^0$ .....	112
Figure 4.13 : Pitch Angle vs. Time Graph According to Commands Taken.....	
From Table 4.3.....	113
Figure 4.14 : Zoomed Pitch Angle vs. Time Graph.....	114
Figure 4.15: Satellite Desired Euler Angles and Angular Velocity.....	
of the System.....	116
Figure 4.16 : Torque from Magnetic Torquer and Magnetic Moment .....	117
Figure 4.17 : Satellite Desired Euler Angles and Angular Velocity .....	
of the System for Case 2 .....	118

Figure 4.18 : Torque from Magnetic Torquer and Magnetic Moment .....	
for Case 2 .....	119
Figure A.1 : Relationship Between the Keplerian Elements.....	141
Figure A.2 : Tetrahedral Configuration .....	143
Figure A.3 : Geometric Relationship Between the Angle $\varphi$ and the Sides .....	144
Figure A.4 : Geometric Relationship Between the Sides a and x .....	144

# CHAPTER I

## INTRODUCTION

This chapter, briefly describes the Low\_Earth Orbit satellites. BILSAT-1 satellite and its attitude determination and control subsystem is introduced in order to give an example for Low-Earth Orbit (LEO) satellites. Literature survey on the attitude control of satellites is also a subject of this chapter. Generally, this work is about the attitude determination and control subsystem components of a satellite and linear control techniques designed for attitude control.

### **1.1 Low-Earth Orbit Satellites and BILSAT-1 Attitude Determination and Control Subsystem**

In 21<sup>th</sup> century, the use of Low-Earth Orbit (LEO) satellites has increased with the great development of space technology. These satellites, ranging from micro to mini types, are now popular mostly for telecommunication, weather forecasting, taking images of Earth, ship movement surveillance, obtaining digital elevation maps of disaster areas, environmental tracking of some animals for scientific research and so on. LEO satellites fly between 600 km. and 1000 km. above the Earth. Unlike geostationary satellites, they travel across the sky. A typical LEO satellite takes less than two hours to orbit the Earth. A single satellite is in view of ground equipment for only a few minutes.

Turkish researchers in the fields of near Earth space technologies have started the microsatellite project, BILSAT-1, in August 2001 in order to perform some of the missions described above with a satellite belonging to Turkey. Also this project was a first step in planning to produce its own satellites from design to in-orbit operation

for Turkey. BILSAT-1 was manufactured within a Know-How Transfer and Training ('KHTT') program between Surrey Satellite Technology Limited (UK) and TUBITAK-BILTEN (Turkey). The satellite was launched by a COSMOS 3M launch vehicle from the Plesetsk Cosmodrome in Russia on September 27, 2003.

BILSAT-1 is an Earth observation satellite in a sun synchronous Low-Earth orbit at a 686 km. altitude and has a mass of 129 kg. The orbit is called **sun synchronous** because the orientation of the orbit plane will remain nearly fixed relative to the sun as Earth moves in its orbit. Thus, the spacecraft will continuously view the surface of the earth at the same local time at any given latitude. BILSAT-1 has an average orbit period of about 97.7 minutes. It spends nearly 32 minutes in Earth eclipse. This orbit gives a contact time of about 40 minutes per day, divided into four equal portions of about 10 minutes each during the day. BILSAT-1 is followed up successfully via ground control station at TUBITAK-BILTEN. BILSAT-1 is a member of DMC (Disaster Management Constellation) which is an international consortium of which the member countries are UK, Algeria and Nigeria. The DMC satellites share the same orbit and are separated from each other with a phase angle of 90 degrees. This constellation guarantees to image any location on the globe at least once per day. Figure 1.1 shows BILSAT-1 microsatellite.

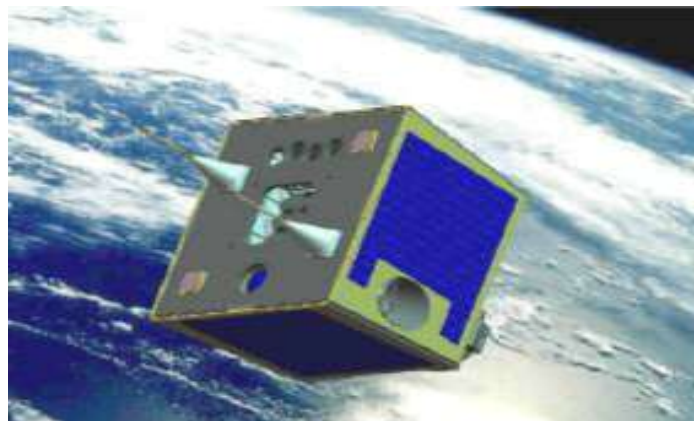


**Figure 1.1:** BILSAT-1 Satellite Launched on Sept. 27, 2003.

Attitude determination and control subsystem (ADCS) plays an important role in the design steps of a satellite. Attitude determination process simply determines the orientation of the spacecraft with respect to a reference frame. The data taken from the sensors of the satellite helps to determine the location of the satellite. Attitude control mechanism works in cooperation with attitude determination process to maintain and achieve the determined orientation in space. This work basically is about the attitude control of a Low-Earth Orbit satellite. Satellite attitude dynamics and kinematics are modelled in order to determine the angular velocity and position of a satellite with respect to Earth. The equations used in this thesis include disturbances due to Earth's gravitational field and aerodynamic torque. Since the simulations in this work are based on the real parameters taken from the BILSAT-1, the ADCS subsystem of BILSAT-1 is explained briefly in the following paragraphs.

The attitude determination and control subsystem of BILSAT-1 is composed of four sun sensors, four rate sensors, two magnetometers and two star cameras as sensors. Four reaction wheels, three torque rods, and a gravity gradient boom are designed to act as the actuators. A block diagram of this system is shown in Figure 1.2 [1], [2], [3].

Actuators and sensors provides full three-axis control to the satellite. Control accuracy of  $\pm 0.02$  degrees shall be maintained, along with attitude knowledge of  $\pm 0.006$  degrees during this control mode according to BILSAT-1 mission requirements.

The reaction wheels of BILSAT-1 are arranged in a tetrahedral formation, with one of the wheels being mounted in line with the pitch axis. The wheels will run with a momentum bias, but the overall momentum of the system will be zero which means that the satellite will operate with zero momentum bias. Configuration of the wheels is shown in Figure 1.3 [1], [2], [3].

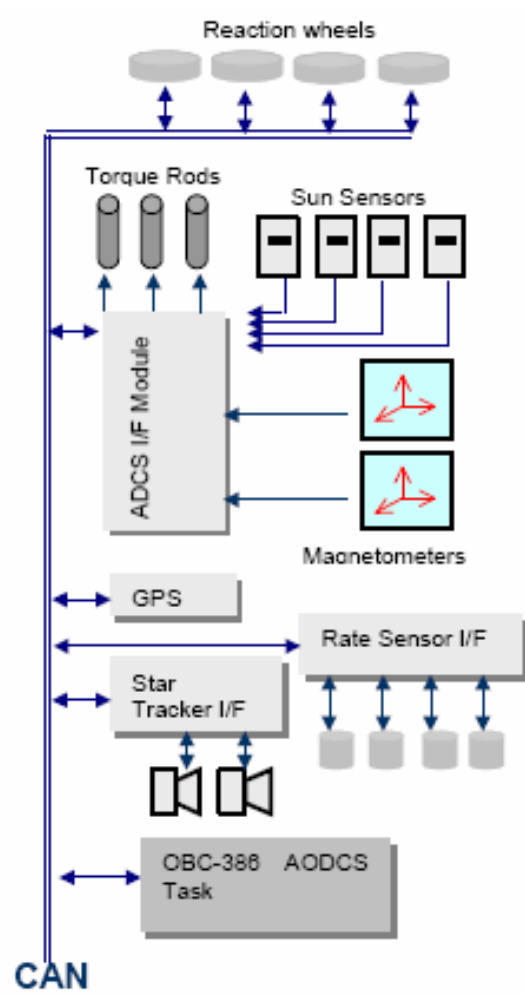


**Figure 1.2 :** ADCS Block Diagram of BILSAT-1.



**Figure 1.3 :** Four Wheels in a Tetrahedral Configuration.

Each wheel is capable of delivering a torque around 6-7 mNm in air, up to 10 mNm in vacuum.

The three-axis control mode gives the satellite the ability to slew about a defined axis. The satellite is also able to slew up to  $\pm 30$  degrees around the pitch axis to take pictures of a defined location on earth from different angles. This is shown in Figure 1.4 [1], [2], [3]:

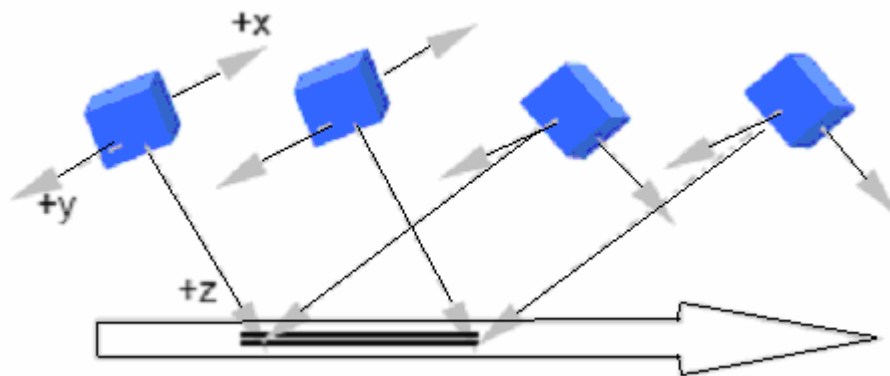


**Figure 1.4** : Illustration of 30 Degree Slewing about Pitch Axis. Arrow Illustrates the Movement Direction on Ground. (+x=roll , +y=pitch , +z=yaw axes).

The reaction wheels on the satellite are expected to operate for a minimum of five years. Gravity-gradient boom will be deployed after this period. The satellite will perform a nadir pointing mission with  $\pm 0.3$  degrees pointing accuracy during the remaining life time period. This mode will effect the spacecraft's three axis control capabilities like thrust vector alignment which helps slewing operation, stereoscopic imaging and off-track imaging. On the other hand, it can still take images in nadir pointing direction.

Torque rods are used to dump the excess momentum, which is caused by the external disturbances, accumulated on the wheels . The momentum on the wheels will reach saturation because of which their angular velocity can no longer be

increased. Before saturation occurs, magnetic torquers supply torque to bring the angular velocity of the wheels back to normal operating values.

To perform orbital maneuvers, BILSAT has a propulsion system which is shown in Figure 1.5 [1], [2], [3].



**Figure 1.5:** Propulsion System on the Satellite.

In the propulsion system, "butane" is used as the propellant. It can supply a thrust of around 50 Nm.

There are two SSTL Altair HB star cameras on the spacecraft as given in Figure 1.6 [1], [2], [3]. Processed attitude information is provided to the ADCS by these cameras, which can be used to compute the attitude.

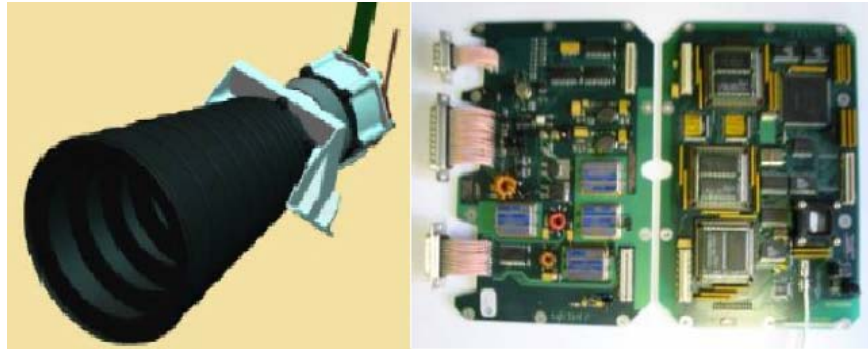


**Figure 1.6 :** SSTL Altair HB Star Cameras (Processing Unit and Camera Head)

The satellite is equipped with four micro-electro-mechanical systems (MEMS) gyros in order to be employed as rate sensors in fast attitude manoeuvres. They are the complements of star cameras.

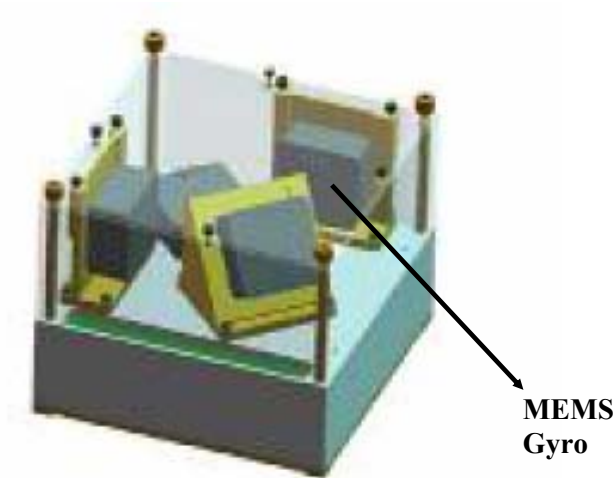


**Figure 1.7 :** MEMS Gyros as Rate Sensors, [1], [2], [3].

When Star tracker fails to give rate information during high slew rates above 0.5 deg/sec., rate gyros are essential sources of reference for rate information. Because of this reason, the rate gyros on BILSAT-1 are particularly important during stereoscopic imaging maneuvers.

The GPS receivers on the satellite, are capable to supply a position knowledge of +/- 50 m. There are four GPS antennas on the satellite. It is possible to determine the attitude up to +/- 1 degree.

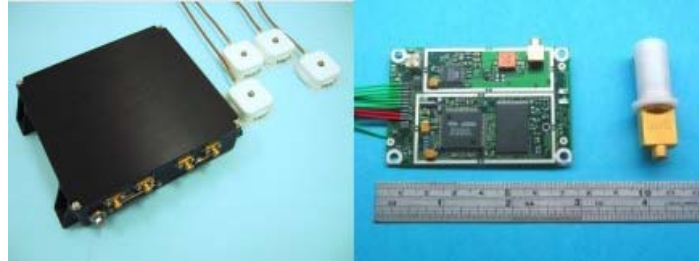


**Figure 1.8:** The SSTL SGR-20 GPS Receiver Determines the Attitude with Position Information, [1], [2], [3].

In summary, the satellite makes the maximum use of imaging capability installed on board. There are star cameras and reaction wheels to control the satellite in three axis mode with an attitude control accuracy of  $\pm 0.02$  deg. and with an attitude knowledge of  $\pm 0.006$  deg. SGR-10 GPS receiver is used in order to determine its orbital position to within  $\pm 50$ m. The spacecraft is equipped with a set of solid-state data recorders to store the images generated by the imaging subsystem, linked to the RF communications and imaging systems by very high speed data links. Some of the data sheets of the components explained above are given in Appendix B. For more information on the BILSAT-1, see References [1], [2], [3].

## 1.2 Previous Background

This section summarizes the recent knowledge on attitude dynamics and control of satellites. The publications from 1990 up to 1996 have been investigated from the thesis written by Özge Uslu, [15] and Hakkı Özgür Derman, [9].

This paragraph simply summarizes the work done for the development of the satellite technology. The next paragraphs give information about the thesis searched in order to design the controller plant for the satellite system. Hughes (1986) and Wie (1998) are well-known references on spacecraft dynamics. Wie, Weiss and Arapostathis (1989) prove that a PD controller stabilizes a spacecraft in a manner of attitude control. In their work, spacecraft model is taken as a classical one with no moving parts. In 1997, Hall investigated that reaction wheels can be used in energy storage. After this investigation, Hall (2000) control the spacecraft by using reaction wheels as actuators. In 2001, Hall, Tsiotras and Shen use modified Rodrigues parameters to describe the attitude of a spacecraft and model the nonlinear attitude control system with thrusters and reaction wheels. Lee, Park and Park (1993) propose a nonlinear sliding mode controller. The use of Euler parameters or unit quaternions in attitude control problems, is started by Fjellstad and Fossen (1994), but they apply the results to underwater vehicles sliding mode controller. Show, Juang and Jan (2003) present a nonlinear attitude controller based on a linear matrix inequality method. This historical summary for the studies on attitude control is also mentioned in Reference [20].

James R. Wertz [8] explains nearly all of the topics regarding the design of attitude determination and control subsystems in his book named as spacecraft attitude determination and control. He gives information about attitude geometry, attitude hardware, attitude determination, attitude dynamics and control. His book is very useful for understanding the design steps for attitude control and determination systems of the satellites. Mission analysis of different satellite applications can also be found in his book.

Özge Uslu [15] worked on the orbit dynamics, attitude dynamics and control of a geostationary satellite. She simulated the translational and rotational motion of TURKSAT 1-B. She developed control laws for pitch, which uses momentum wheel and for roll, which uses thrusters as actuators. In her thesis, she also gives literature survey on attitude dynamics and control which helped us to follow the historical development of the attitude control schemes.

Hakkı Özgür Derman [9] demonstrated the 3-axis attitude control of a geostationary satellite. He introduced the attitude control of a satellite platform similar to TURKSAT-1B. He applied PD controller for pitch attitude with strapdown momentum wheels and he designed an integral plus full state-feedback controller for yaw/roll regulation. In his thesis, he used pole placement technique and tested the effects of various pole locations to the control scheme. Pulse width modulated thrusters were used as actuators. He worked on tuning the activation period of thrusters for fuel consumption. Similar to Özge Uslu, he gives literature survey which describes several different control algorithms applied through the period from 1990 to 1999.

Emre Yavuzoğlu [29] presents the singularity problem on the steering laws for control moment gyroscope systems used in spacecrafts. He describes different steering laws to avoid singularity problems in angular momentum trajectory of the maneuver for control moment gyroscope systems.

At the Norwegian University of Science and Technology (NTNU), Soglo (1994), Kristiansen (2000), Fauske (2002), Busterud (2003), Ythreus (2003), Overby (2004), have studied attitude control of small satellites with magnetic coils and reaction wheels as actuators. They apply their investigations to the NCUBE, NSAT-1 satellite projects.

Bjorn Even Busterud [21] studies the mathematical model and attitude control for microsatellites. He proposes linear quadratic regulator and energy based regulator for attitude control with magnetic torquers as actuators. In magnetic field modelling, he uses two different methods which are IGRF (International Geomagnetic Reference Field) and DIPOL modelling. He simulates his foundations for two satellites, NCUBE and NSAT-1.

The implementation of reaction wheels as actuators in satellite design can be found in the thesis of Geir Ythreus [23]. He models the reaction wheels in tetrahedral configuration. He introduces reference model for obtaining smooth trajectory of controlled parameters. The ideas presented in his work are used in this thesis with

modifications. He designs a linear regulator according to linearization principles. Sliding mode controller and nonlinear regulator are applied according to the results of the Lyapunov analysis. His simulations are based on the NSAT-1 environment.

The effect of environmental disturbances and noise is studied in the thesis of Eli Jerpseth Overby [7]. Mathematical modellings of Earth's magnetic field and disturbance torques are described in his thesis. Stabilization of linear and nonlinear systems are defined. Energy based angular velocity feedback controller and energy based attitude feedback controller are introduced as nonlinear controllers and linear quadratic optimal gain is given as linear controller. He compares the linear and nonlinear controllers in his simulations for NCUBE. He recommends to use Wisniewski [22] controller for stabilization. Magnetic torquers are the actuators of the design.

Stian Sondersrod Ose [17] presents an attitude determination system for satellites. He implements a Kalman filter to produce the estimated states needed by the controller. His thesis is useful for obtaining some definitions and notations about sensors, reference models, mathematical modelling and attitude representations.

Nonlinear control of the microsatellite European Student Earth Orbiter (ESEO) is studied by Mortar Pedersen Topland [20]. He derived two linear and four nonlinear controllers as a result of his studies about linearization and Lyapunov theory. These controllers also work for different inertia matrix values applied to the system. The fourth nonlinear controller is the sliding mode controller. A bang bang controller with dead zone is used for thruster modelling. He also applies reaction wheels as actuators and states that reaction wheels are actively used in the nonlinear controllers.

Oyvind Hegrenaes [30] connects the controller within a closed loop with nonlinear system and checks the effectiveness through simulations. In his thesis, model predictive control problem is formulated and explicit model predictive control controller is derived. He uses linear control techniques such as PD control and linear quadratic regulator with the purpose of comparing these with other techniques.

Wisniewski [22] suggests a new controller which is shown to be locally and globally stable for the 3-axis attitude control based on magnetic torquing applied in Orsted satellite.

This thesis is based on the previous work done on the ADCS which is accomplished by the Surrey Space Center (SSC), in conjunction with Surrey Satellite Technology Ltd. (SSTL) and TUBITAK (Technical Research Council of Turkey) –BILTEN (The Information Technologies and Electronics Research Institute). The knowledge obtained from the literature survey is used on the design of linear controllers when magnetic torquers and reaction wheels are selected as actuators. Also mathematical equations and assumptions to derive satellite's dynamical and kinematic equations are studied from the theses written by the researchers mentioned above.

### **1.3 Scope of this Thesis**

This thesis gives a presentation of the attitude determination and control components of a satellite system in detail. It does also inform us about the linear attitude control design of a spacecraft using different actuators such as magnetic coils and reaction wheels. A nonlinear mathematical model of a spacecraft is developed with the assumption that the satellite is a rigid body. Linearization is used to derive linear controllers. Throughout this thesis, linear regulator is applied for attitude control when reaction wheels are the actuators of the satellite system and linear quadratic regulator is selected as controller when magnetic torquer behaves as the actuator of the system. Controllers are tested in MATLAB/SIMULINK environment. System performance is evaluated by the help of the simulations. The results of the simulations are also compared with the results obtained from the nonlinear control techniques explained in the thesis of Soner Karataş [26] and simulations taken from BILSAT-1 ground station. The satellite parameters are selected similar to the actual BILSAT-1 satellite platform and are also used in simulations. BILSAT-1 attitude determination and control subsystem is described briefly. This thesis does also focus on evaluation of environmental forces that influence the orientation of the spacecraft.

## **1.4 Outline of the Thesis**

In Chapter II, attitude determination and control components are described in detail. It explains several types of sensors and actuators. It also briefly describes the main properties of the actuators and sensors. Mathematical modelling of the satellite is given in Chapter III. Linearization of the satellite model and information about the environmental and internal torques effecting the attitude control of the satellite is also given in this chapter. Linear control techniques applied in the present study are explained in Chapter III. Simulation results are shown in Chapter IV. Lastly, Chapter V includes the conclusion of the thesis and future work to improve the controllers or satellite model similar to BILSAT-1 environment.

Lastly, it is worth mentioning that the controllers and attitude control system are designed and simulated in MATLAB 7.0 and SIMULINK 6.0 R14.

## CHAPTER 2

### ATTITUDE DETERMINATION AND CONTROL COMPONENTS

Attitude determination is the process of determining the orientation and location of the spacecraft relative to some reference frame, [8]. The most commonly used reference vectors are the unit vectors directed toward the Sun, the center of the Earth, a known star, or the magnetic field of the Earth. An **Attitude sensor** measures the orientation of a given reference vector relative to the spacecraft reference frame, [8]. Sun sensors, rate sensors, magnetometers, Star cameras, Star sensors are different types of sensors which can be used in attitude determination [8]. The orientation of the spacecraft relative to the reference vectors can be computed after the orientation of these vectors are determined relative to the spacecraft frame [8].

The process of achieving and maintaining an orientation in space is called attitude control. Spacecraft is reoriented from one attitude to another with attitude maneuvering process. After reorientation or an action that causes a change in attitude, the existing attitude shall be maintained relative to some defined reference frame. This is defined as attitude stabilization. **Actuators** are used for attitude control, stabilization or maneuvering actions, [8]. They supply the desired control torque needed to perform actions defined above.

Different types of sensors and actuators are explained in the sections given below. Advantages and disadvantages of various reference sources is given in Table 2.1, [8].

**Table 2.1 : Reference Sources Used in Attitude Determination.**

<b>REFERENCE</b>	<b>ADVANTAGES</b>	<b>DISADVANTAGES</b>
<b>SUN</b>	Bright, low power and weight. Shall be known for solar cells and equipment protection.	May not be visible during parts of the orbit. Accuracy limitation to 1 arc minute.
<b>EARTH OR OTHER CENTRAL BODY</b>	Available for nearby satellite. Bright, necessary for many sensor and antenna coverage, easy analysis.	Requires scan motion to sense. Horizon sensors must be protected from sun. Resolution limited to 0.1 deg.
<b>MAGNETIC FIELD</b>	Economical, low power requirements. Available for LEOs	Poor resolution. Good only near Earth. Limited by field strength and modelling accuracy, sensitive to biases.
<b>STARS</b>	High accuracy, available anywhere in sky, orbit independent	heavy, complex, and expensive sensoes. Identification of stars is complex and time consuming, usually requires second attitude system for initial attitude estimates.
<b>INERTIALSPACE (MAGNETOMETERS, ACCELEROMETERS)</b>	Requires no external sensors, orbit independent, high accuracy for limited time intervals	Senses change in orientation only- no measurement; Subject to drift. Relatively high power and large mass.

## 2.1 Attitude Sensors

Throughout this part, different types of sensors used in attitude determination are explained. The mechanisms behind these sensors are mentioned briefly. This section is a simple guide for the selection of sensors in the design phase of the spacecraft system.

## 2.1.1 Sun Sensors

Sun sensors are one of the most widely used attitude determination sensors. They are also used to protect Star trackers, to provide a reference for attitude control, and to position solar arrays. Brightness of the sun permits the use of simple, inexpensive, reliable equipment with minimal power requirements. In summary, Sun sensors are basically required in spacecraft operations since most missions require solar power and have sun-sensitive equipment which needs protection against sunlight or sun heat.

There are wide range of Sun sensors with Fields Of View (FOV) ranging from several square arc-minutes ( $10^{-7}$  sr) to 128 by 128 degrees( approximately  $\pi$  sr) and resolutions of several degrees to less than arc-second. Solid angle or steradian (sr) is the area of the spherical triangle measured on the curved surface of the unit sphere. In order to convert  $\text{deg}^2$  to sr unit, the value in degrees is calculated by  $(\pi/180)^2$ . Angular separation between two objects as seen from the spacecraft is measured in arc minute unit and 1 arc minute is equal to the  $1/60$  th of 1 degree. The conversions between all the units dealt in this section and the other sections can be found in Reference [8] in detail. The accuracy range of Sun sensors changes from 0.25 degrees to 6 degrees depending on the type and number of sun sensors applied.

Three main types of sun sensors are analog sensors, sun-presence sensors and digital sensors.

### 2.1.1.1 Analog Sensors

Analog sensors are sometimes called cosine detectors since their working principle is based on the sinusoidal variation of the output current of a silicon solar cell as a

function of the sun incidence angle, [8]. Typical cosine detector sun sensor is shown in Figure 2.1, [8].

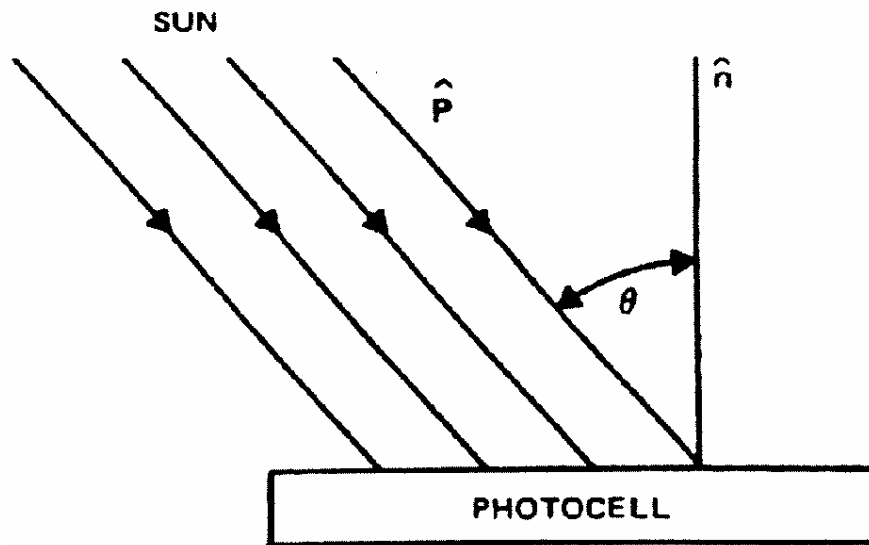


**Figure 2.1 :** Cosine Detector Sun Sensor.

The output current of one photocell is proportional to the cosine of the angle of incidence of solar radiation as given in Equation 2.1. When a solar cell is exposed to light at a certain frequency, it produces power. The amount of current depends on the light's frequency and brightness.

$$I(\theta) = I(0) \cos \theta \quad (2.1)$$

To achieve accuracy over a wide angular range, several cosine detectors can be combined such that each gives a summed output as shown in Figure 2.2, [8] and Figure 2.3, [8].

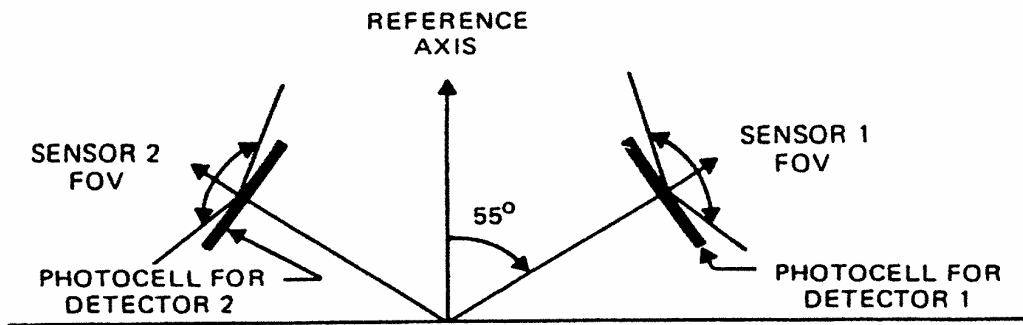


**Figure 2.2 :** Two Cosine Detectors Combined to Provide Wide Sun Angle Measurement Range.

Figure 2.3 shows the output of the two cosine detectors located as given in Figure 2.2.

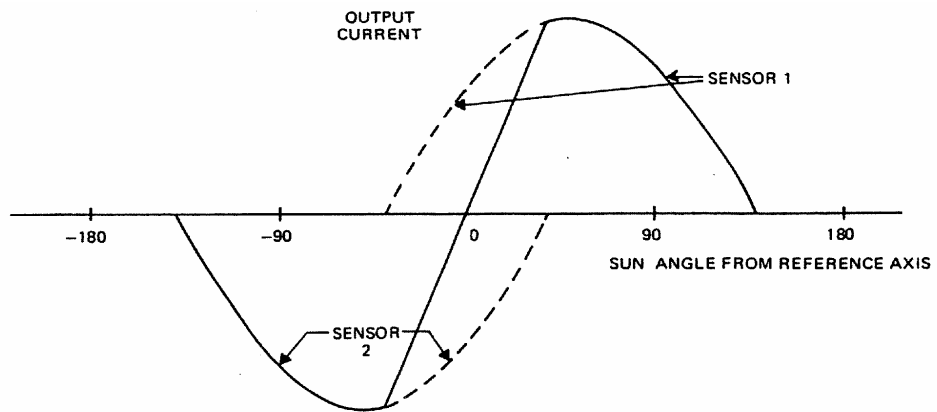


**Figure 2.3 :** Summation of the Outputs from Two Sensors. The Solid line Represents the Summed Output.

Unlike other sensors, analog sensors use onboard solar cells of the satellite without the need of additional hardware. But they are extremely inaccurate with 1° accuracy in Field Of View (FOV) of 30°.

### 2.1.1.2 Sun Presence Sensors

Sun presence detectors generate a step function response whenever the Sun is within the FOV of the detector. These sensors are generally used to protect instrumentation and to position the spacecraft. There are different applications of Sun presence sensors. A typical shadow bar detector shown in Figure 2.4, [8] has a steep output slope with a limited FOV and 1-arc-minute accuracy. When sunlight enters to the region limited by the help of shadow bars in an appropriate angle, photo cells sense the presence of sunlight.

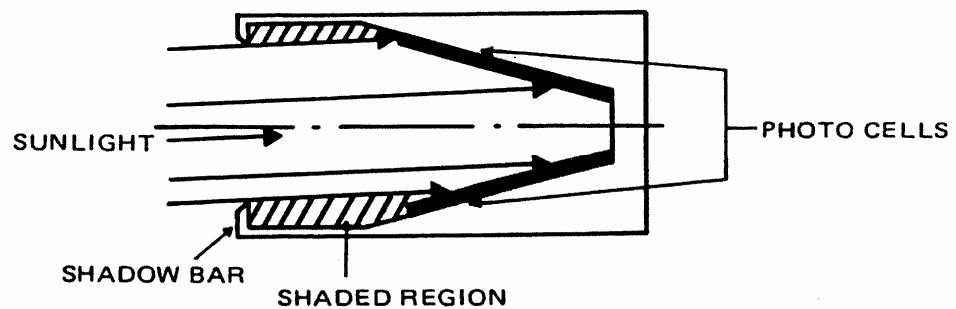


Figure 2.4: Simple Shadow Bar Sun Sensor.

Some spacecraft sometimes employ one or more Sun presence detectors composed of two slits and a photocell as shown in Figure 2.5, [8].

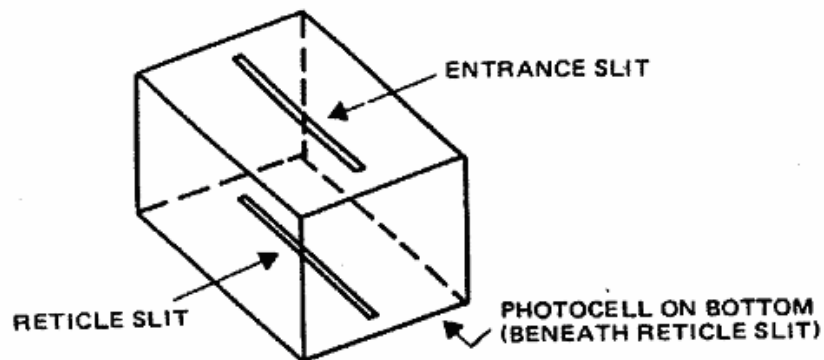
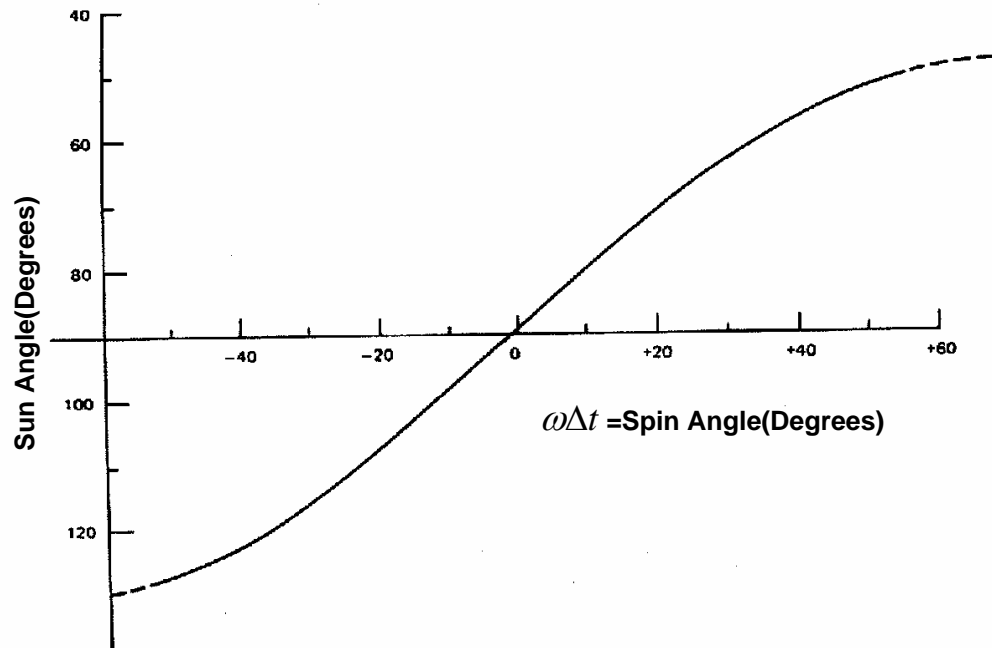


Figure 2.5: Two Slit Sun Presence Detector.

When Sun lies in the plane formed by the entrance and reticle slits with the required angle, the photocell will indicate the Sun presence. When two sensors are combined in a V shaped position, the time between sun pulses is a measure of the Sun angle, as shown in Figure 2.6, [8].

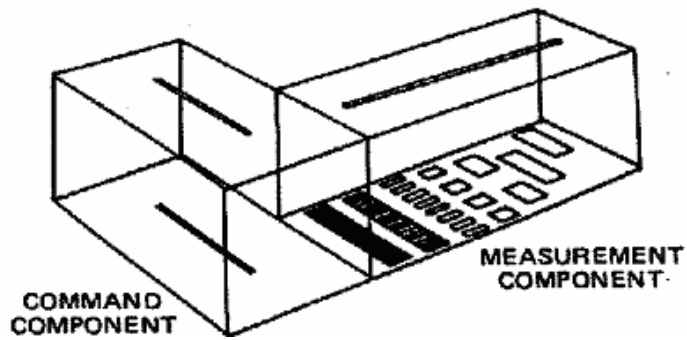


**Figure 2.6:** Sun Angle as a Function of Spin Angle for Typical Solar V-Beam Sensor with 45-Deg Tilt.

### 2.1.1.3 Digital Sensors

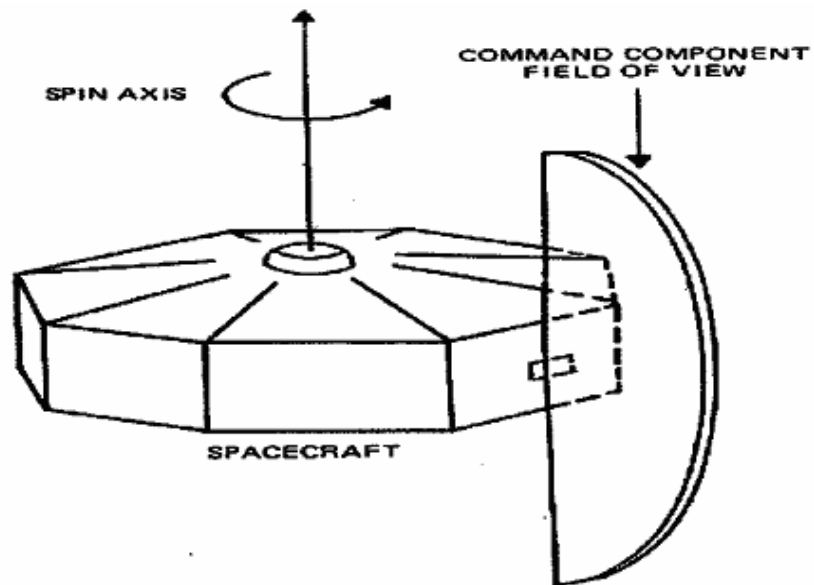
Digital Sun sensors are commonly composed of two parts: the command unit and the measurement unit as given in Figure 2.7, [8].

The command unit basically acts as a Sun presence detector, and the measurement unit provides a digital output which is a representation of the Sun incidence angle relative to the normal of the sensor face whenever the Sun is in the FOV of the command unit.



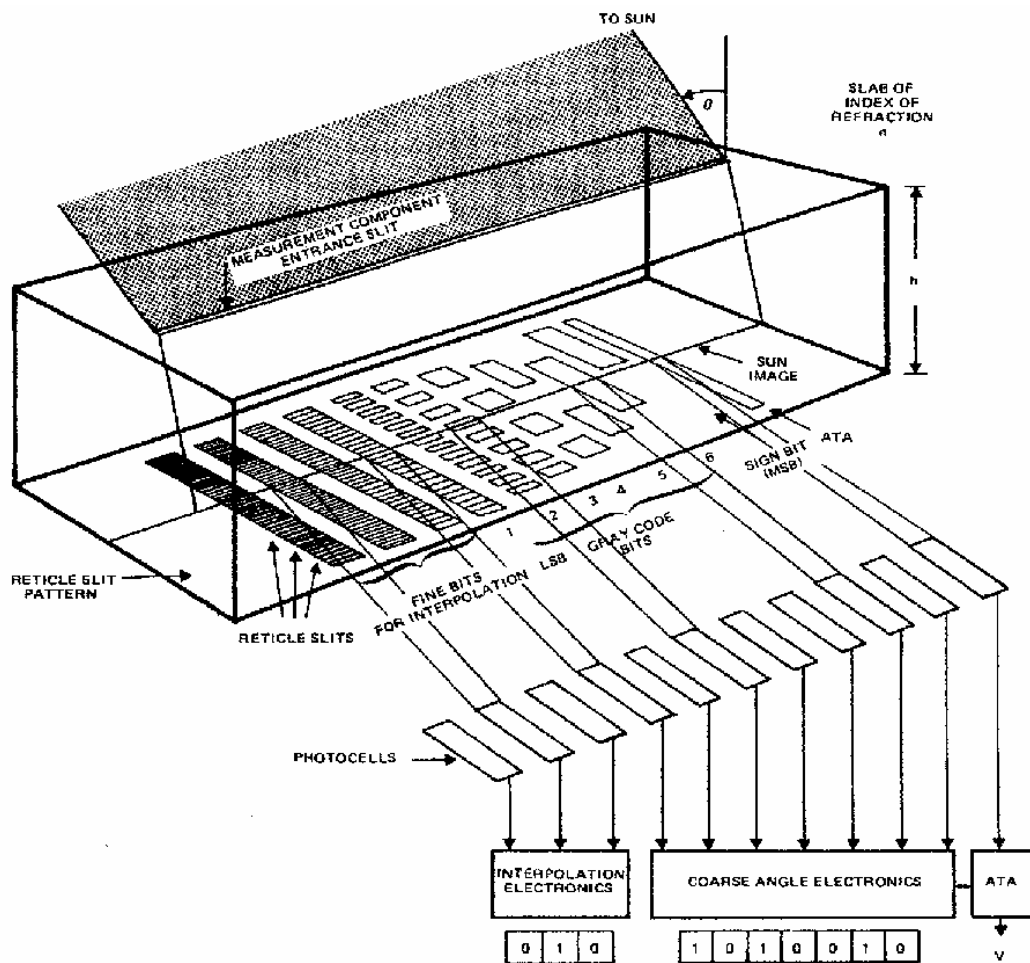
**Figure 2.7:** A Simple Digital Sensor.

Figure 2.8, [8] gives an illustration of the Sun sensor command component FOV for spinning spacecraft.



**Figure 2.8:** Field of View of Sun Sensor Command Component.

Meanwhile, Figure 2.9, [8] shows in detail how the digital Sun sensor generates its output in binary and gray codes.



**Figure 2.9:** Sun Sensor Measurement Component Detail and Output, [8].

The Sun image, after sunlight goes through the measurement component entrance slit, is refracted and illuminates a pattern of slits. There are photocells beneath each row of slits which essentially generate a digital output. The four groups of slits include an automatic threshold adjust (ATA), a sign bit, encoded bits, and fine bits. Reticle patterns can be illustrated with different coding schemes such as gray code or binary code.

Also, Figure 2.10, [8] illustrates plot of output from photocells versus Sun angle for Adcole digital Sun sensors.

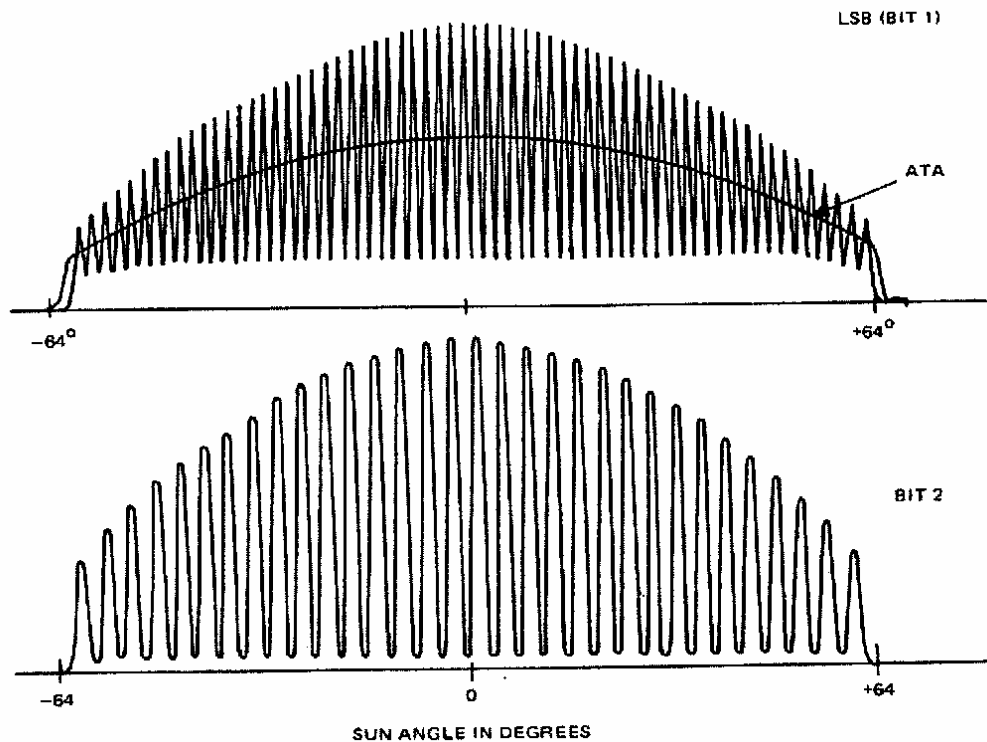


**Figure 2.10:** Plot of Output from Photocells Versus Sun Angle for Adcole Digital Sensor.

In digital sensors, almost a Sun angle with accuracy of 0.125 degree can be computed. If the nominal FOV for digital sensors, for example, is limited to  $\pm 64$  deg., full 180 degree coverage can be accomplished by mounting two or more sensors in such a way that their FOVs overlap to increase the total FOV area.

In summary, Figure 2.11 is introduced to give an example for a Sun sensor. The basic properties of the Barnes 13-517 coded Sun sensor is illustrated below the figure.



**Barnes 13-517 Sun Sensor**  
5.1" x 2.4" x 1.9", <15 oz.  
<.03 Watts S/C Conditioned  
Field-of-View: 128° x 168°  
Radiation: 100 krad  
Parts Level: S-Level Accuracy: 0.3° EOL (3-sigma)  
Reliability: 0.997 Non-Redundant; 0.99999 Redundant Over 15 Years

**Figure 2.11:** Barnes 13-517 Sun Sensor.

## 2.1.2 Horizon Sensors

The essential way for directly determining the attitude of a spacecraft relative to the Earth is to use horizon sensors (Earth sensors), [8]. For payloads like attitude determination and control, communications or weather forecasting, determining the attitude of spacecraft relative to Earth has an extreme importance. Earth covers about 40% of the sky for near Earth orbit satellites so Earth can not be treated as a point source like the Sun. Hence most sensors are designed to detect the Earth's horizon instead of Earth. Horizon sensors use the Earth's horizon to determine the orientation of the spacecraft with respect to Earth. They are infrared devices that detect a temperature contrast between deep space and the Earth's atmosphere. The main difficulty encountered in horizon sensors includes setting triggering thresholds to distinguish between the true horizon and the edge of the atmosphere. Sun rejection capability which is provided by redundant sensors or optical systems is important when horizon sensors are used for

onboard control. Reference [8] includes detailed information about horizon sensors.

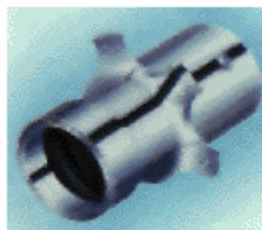
Figure 2.12 and Figure 2.13 show different types of horizon sensors.



**Barnes 13-470-RH Horizon Sensor**

7.5" D x 4.8" deep, 38.7 oz. (per 3 telescope assembly)  
600 mW typical,  $\pm 14.3$  Volts DC (+0.6V/-0.8V)  
Accuracy:  $\pm 0.2^\circ$  (3-sigma) with two out of three  
telescopes operating  
Operating Range:  $10^\circ$  around nadir  
Temperature Range:  $-40^\circ\text{C}$  to  $+40^\circ\text{C}$  (oper.)

**Figure 2.12:** Barnes 13-470-RH Horizon Sensor and Technical Properties.



**Ithaco Horizon Crossing Indicator (HCI)**

5.9 d x 9.9 cm, 0.65 kg  
0.7 W, 28 +/- 4 V  
Field-of-View:  $1^\circ \times 1^\circ$  rectangular  
Accuracy:  $0.1^\circ$   
Designed for spinners with 1-200 rpm spin rate

**Figure 2.13:** Ithaco Horizon Crossing Indicator.

### 2.1.2.1 Sensor Components

A scanning mechanism, an optical system, a radiance detector, and signal processing electronics are the basic components of horizon sensor. Horizon sensors are usually classified by the method they use to search the celestial sphere which is also called scanning mechanism. The simplest method used for scanning mechanism is to attach the sensor to the body of the spinning spacecraft. That's the sensor is fixed to the body of the spinning spacecraft and this spin provides the scanning action. The body-mounted horizon sensor and the wheel-mounted horizon sensor work with the principle explained above. Another way of performing scanning action is to rigidly attach the sensor to a momentum wheel of the spacecraft so that the rotation of the wheel provides the scanning mechanism. The latter way, however, consists of integrated systems, such as scanwheels. They include a momentum wheel, horizon sensor, and the electronics, all in one unit. They can be used both in attitude determination and control. Figure 2.14 gives an example illustration for scanwheels.

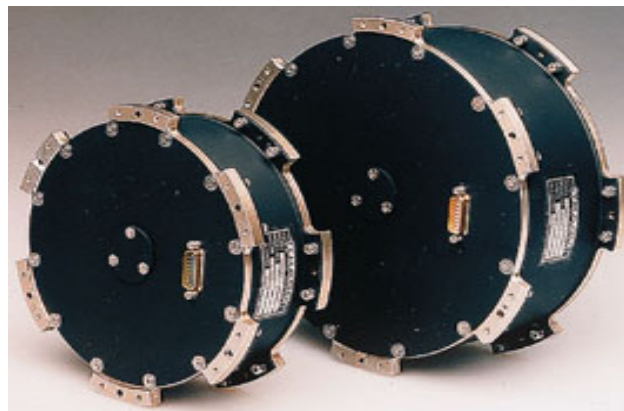


**Figure 2.14:** Ithaco Type Scanwheel Model.

Figure 2.15, [8] shows an example operating schematic of a scanwheel.

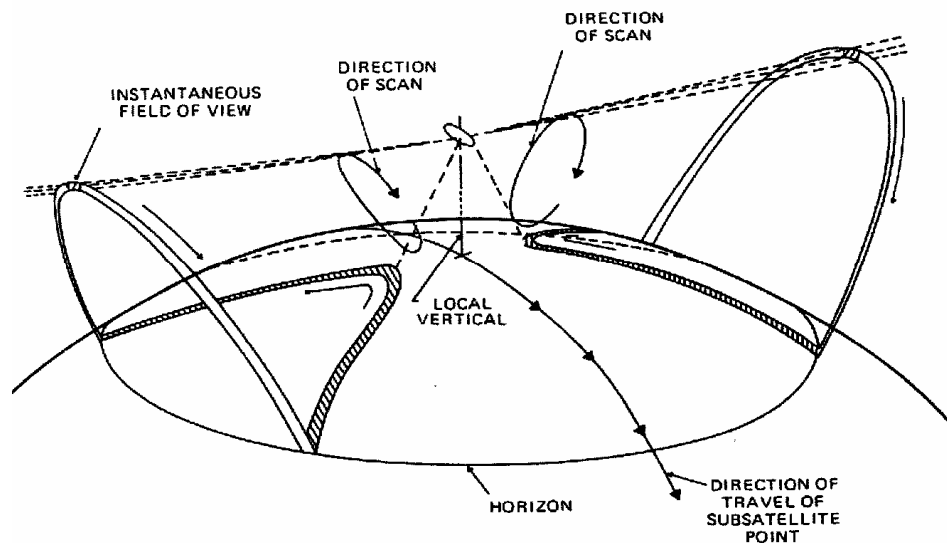


**Figure 2.15:** SEASAT Scanwheel Operating Principle.

The optical system includes a filter that limits the observed spectral band and a focusing lens which focuses the target image on the radiance detector.

Radiance detectors detect the presence of a horizon. Energy radiated from the scanned body is focused by the optical system on the radiance detector which in turn produces a voltage. Photodiodes (which respond to visible light), thermistors, thermo-couples, and pyroelectric crystals (which all respond to red or infrared part of the light spectrum), and bolometers (a very sensitive resistance thermometer) are some types of radiance detectors classified according to their region of spectral sensitivity. The detailed information about these systems can be obtained from Reference [8].

Wertz [8] gives the possible output responses obtained from a horizon scanner as stated below. The output from a scanning horizon sensor is a measure of the time between the sensing of a reference direction and the electronic pulse generated when the radiance detector output reaches or falls below a selected threshold. The reference direction for a body-mounted sensor is generally a Sun pulse from a

separate sensor, meanwhile wheel-mounted sensors typically uses a magnetic pickoff fixed in the body. An increase in the detector output voltage over the threshold indicates a dark-to-light transition. This is called acquisition of signal (AOS), also referred to as in-crossing or in-triggering. A decrease in the output voltage, on the other hand, over the threshold indicates a light-to-dark transition. This is called loss of signal (LOS), also referred to as out-crossing or out-triggering. The percentage of the scan period that the radiance is above threshold is the duty cycle. Knowledge of the scan rate or duty cycle allows the conversion from time to angle either onboard or in ground. The horizon crossing times depend on the sensor FOV, the radiance profile of the scanned body, the transfer function, which is the relation between the radiation pulse incident on the detector, the electronic output of the horizon sensor, and locator, which is an electronic technique used to define the threshold for horizon detection. Locator can significantly affect the overall attitude accuracy of the system. Illustrations of various possible outputs are given in Figure 2.16, [8] where the reference to AOS time ( $t_I \equiv t_{AOS} - t_{REF}$ ), the reference to LOS time ( $t_O \equiv t_{LOS} - t_{REF}$ ), the Earthwidth ( $t_W \equiv t_{LOS} - t_{AOS}$ ), and the reference to midscan time ( $t_M \equiv (t_{LOS} + t_{AOS})/2 - t_{REF}$ ) can be provided by various electronic systems.

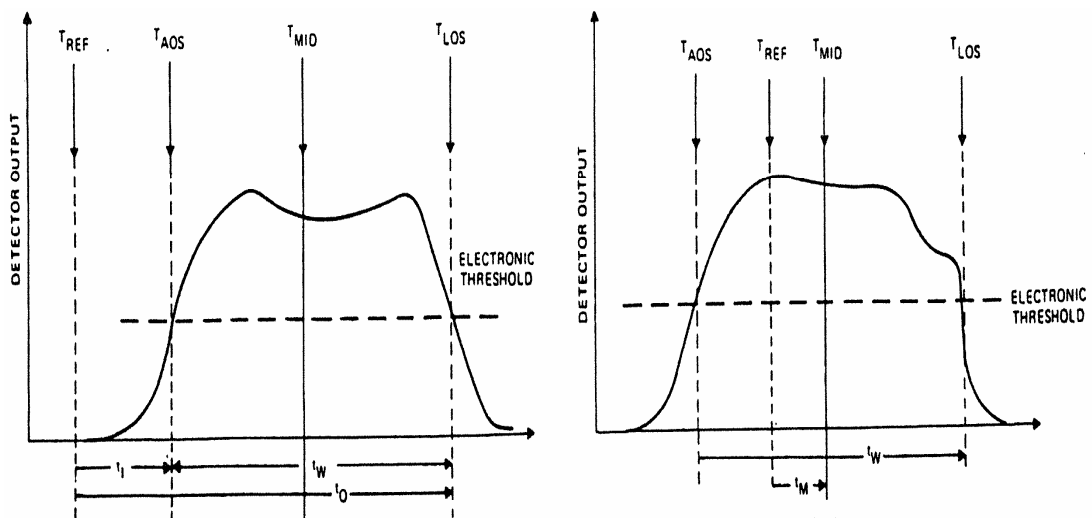


Figure 2.16: Output of Scanning Horizon Sensor.

Signal Processing Electronics process the time signals generated as above to be used in attitude determination software to generate attitude data.

### **2.1.3 Magnetometers**

Magnetometers are vector sensors which measure the strength and direction of the Earth's magnetic field to determine the orientation of a spacecraft with respect to the local magnetic field. Magnetometers are widely used as attitude sensor since they are inexpensive, lightweight, have low power requirements, can operate over a wide range of temperatures and lastly, they have no moving parts. On the other hand, magnetometers are not accurate inertial attitude sensors since they are reliable up to some altitude. Due to a lack of complete knowledge of the magnetic field model, the predicted direction and magnitude of the field at the spacecraft's position are subject to errors. The measurements are limited by the strength of the local field strength, as well as the accuracy of the magnetic field model. For altitudes above 1000 km. where magnetic field strength becomes small enough, errors become substantial (magnetic field strength is inversely proportional to the cube of the distance from the center of Earth). They often have poor resolution and do not give good results if they are far from the Earth.

A magnetometer has two parts: a magnetic sensor and an electronics unit for signal processing. Figure 2.17, [8] shows the general magnetometer block diagram.

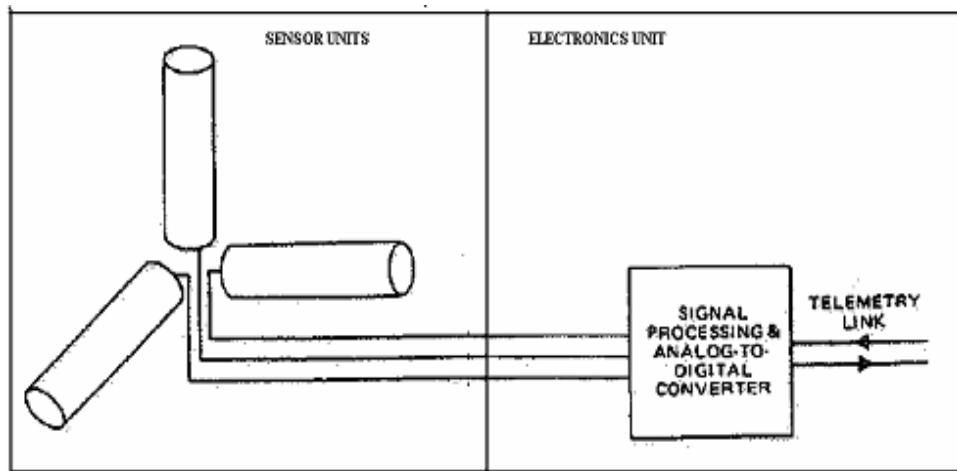


**Figure 2.17:** Generalized Magnetometer Block Diagram.

### 2.1.3.1 Sensor Components

As shown in Figure 2.17, magnetometers are basically composed of two parts: a magnetic sensor and an electronics unit that transforms the sensor measurement into a usable format. Quantum magnetometers, which utilize fundamental atomic properties such as nuclear magnetic resonance; and induction magnetometers, which are based on Faraday's Law of Magnetic Inductance; are two main categories of magnetic field sensors. There are also two types of induction magnetometers: search-coil magnetometer and fluxgate magnetometer. Figure 2.18, [8] shows a dual-core fluxgate magnetometer.

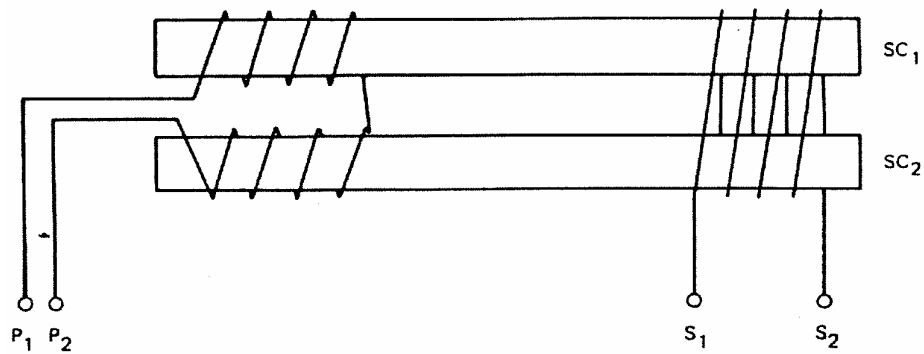


**Figure 2.18:** Dual-Core Fluxgate Magnetometer with Primary and Secondary Induction Coils.

The presence of any ambient magnetic field may be observed as the second harmonic of the current induced in the secondary coil with leads S1 and S2. Two saturable cores wound in opposite directions for secondary coil to be insensitive to the primary frequency.

Figure 2.19, [8] illustrates the operating principle of the fluxgate magnetometer where, frequency of the primary coil's voltage is  $2\pi/T$  ; amplitude of resultant magnetic intensity is  $H_D$  ; Saturation flux density of core elements is  $\pm B_s$  when the magnetic intensity reaches  $\pm H_C$  ; and secondary coil's induced EMF,  $V_s$ , consists of pulses of width  $K_1T$ , separated by time intervals  $K_2T$ .  $K_1T$  and  $K_2T$  are computed by the relations between  $H_D$  and  $H_C$ . These definitions are taken from Wertz [8], pages 182 and 183.

Once the magnetic field sensor signals are processed by the electronics unit, they are transferred to the attitude determination subsystem. These signals are compared with the predicted magnetic field data (based on the location of the spacecraft) and the orientation of the spacecraft can then be determined.

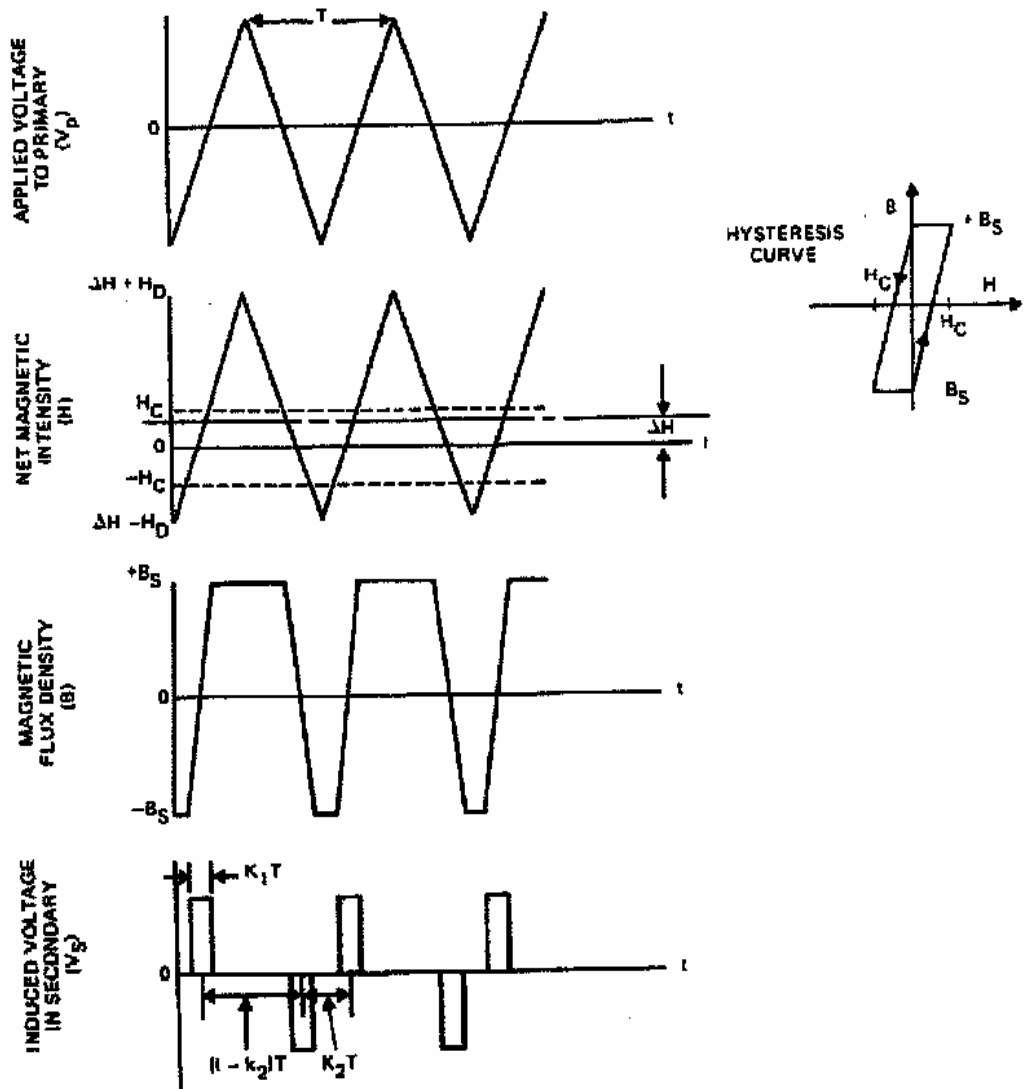


Figure 2.19: Fluxgate Magnetometer Operating Principle and Output Configurations.

### 2.1.4 Star Sensors

James R. Wertz, at his book, *Spacecraft Attitude Determination And Control*; defines the star sensors as given below, [8]:

*Star sensors measure the star coordinates in the spacecraft frame and provide attitude information when these observed coordinates are compared with known star directions obtained from star catalog.*

Star sensors are heavy, expensive, require more power, and subject to interference from Sun, Earth, and other bright light sources. In spite of these disadvantages, they are the most accurate means of attitude determination with accuracies down to arc seconds.

### 2.1.4.1 Sensor Components

Regardless of the type, a Star sensor commonly has the following components: Sun shade, optical system, image definition device, detector, and electronics assembly. Gimbaled Star trackers have gimbal mounts for angular positioning in addition to the above mentioned components. Figure 2.20, [8] shows a simple version of Star sensor hardware.

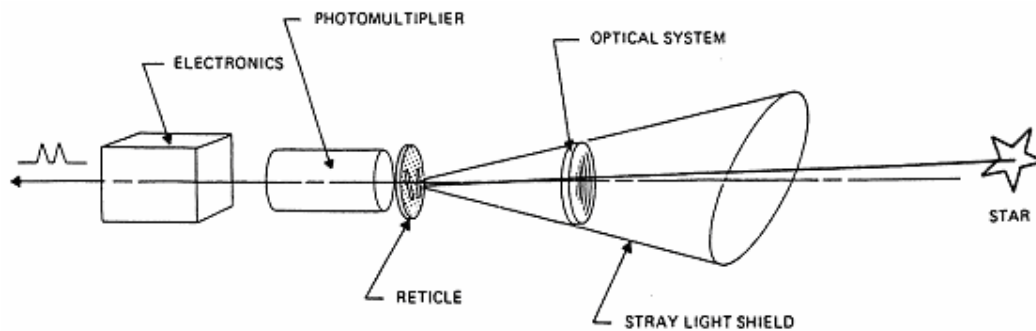


**Figure 2.20:** Simplified Version of a Star Sensor Hardware.

Star sensors are very sensitive to stray light. Sun shades are designed to improve sensor performance by protecting the optical system from sunlight and scattered light reflected by dust particles, jet exhaust particles, and other parts of the spacecraft itself. The optical system mainly consists of a lens. This lens projects the star image on the focal plane. The image definition device selects a small portion of the sensor's FOV (called instantaneous field of view, IFOV) which contains the star image. This can

either be a retile on an opaque plate or an image dissector tube. In an image dissector tube, IFOV electronically scans the FOV. The detector (for instance, a photomultiplier) transforms the optical signal (light) to an electronic signal. The electronics assembly receives the signal from the detector and processes it before sending it to the attitude determination software.

#### **2.1.4.2 Sensor Types**

There are generally three types of Star sensors; Star scanners, which use the spacecraft rotation to provide searching and sensing function; gimbale Star trackers, which search out and acquire stars using mechanical action; fixed head Star trackers, which have electronic searching and tracking capabilities over a limited field of view. All Star sensors must be protected from bright objects by use of a bright object sensor which closes a shutter as long as the object is present in the FOV.

The simplest Star sensors are the Star scanners used on spinning spacecraft. The spacecraft's spinning motion results in the scanning of the celestial sphere by the sensor.

As shown in Figure 2.21, [8], a gimbale Star tracker typically has a very small FOV (usually less than one degree) and through the gimbal assembly it maintains a centered star image. The gimbale angle read-out position is used to determine the star's direction. They are usually used by the spacecraft whose mission requires operation in a variety of attitude positions. The disadvantage of these sensors is that the mechanical motion of the gimbal assembly limits their long-term use and accuracy. Typical accuracies range from one to sixty arc-seconds.

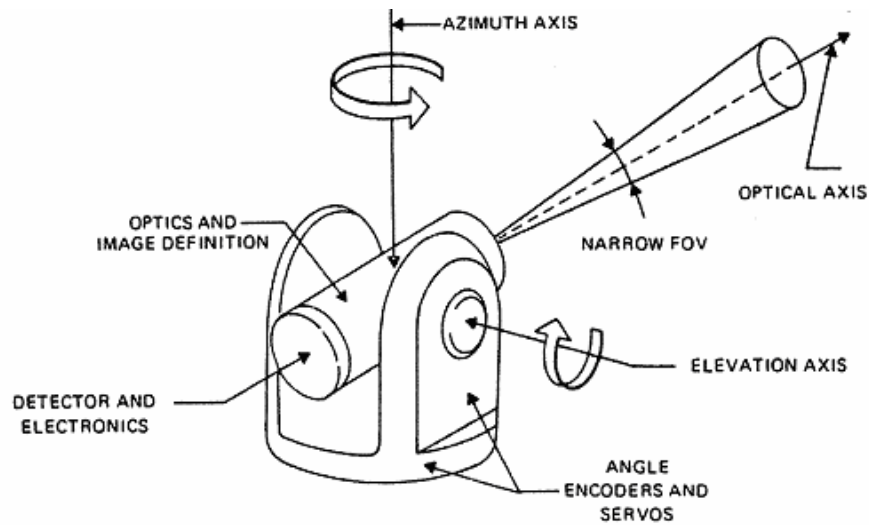


**Figure 2.21:** Gimballed Star Tracker.

A fixed head Star tracker has no moving parts and is typically smaller and lighter than the gimballed Star trackers. In this sensor, IFOV scans the sensor FOV in a search pattern using electronics. After acquiring a Star, IFOV tracks it until either the Star moves out of the FOV or IFOV is commanded to resume searching for another star. Figure 2.22, [8] shows a simplified diagram of a fixed-head Star tracker.

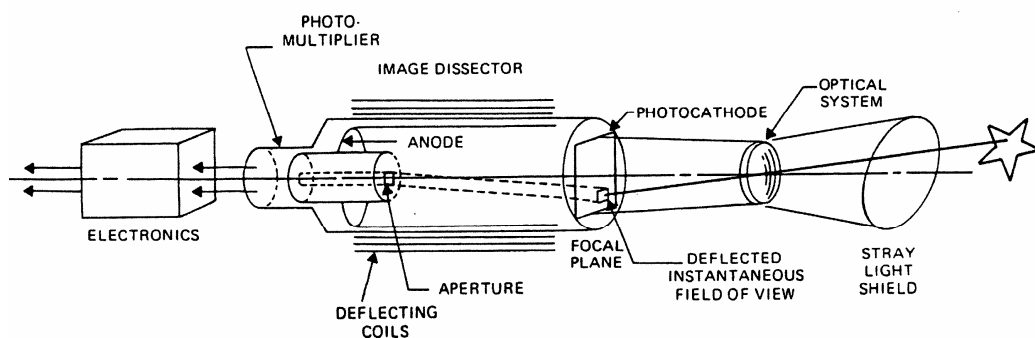


**Figure 2.22:** Cutaway Diagram of a Fixed-Head Star Tracker.

A disadvantage of this tracker is that the image dissector is subject to errors due to stray in electric and magnetic fields. The choice of Star brightness sensitivity and FOV size are mission dependent. Typical FOV size for fixed-head Star

trackers using image dissectors range from 16 arc-minute circle to 8 x 8 degree squares.

Figure 2.23 shows different types of star trackers and characteristics of these sensors.



**Figure 2.23:** Different Types of Star Trackers and Characteristics of These Sensors.

### 2.1.5 Rate Sensors (Gyroscopes)

Rate sensors determine the attitude by measuring the rate of rotation of the spacecraft. They are located internal to the spacecraft and work at all points in an orbit. Since they measure a change instead of absolute attitude, gyroscopes must be used along with other attitude hardware to obtain full measurements. They are subject to drift, and since they have moving parts, they are more complex instruments.

Three basic types of gyroscopes are; rate gyros (RGs), rate-integrating gyros (RIGs), control moment gyros (CMG). RGs and RIGs are attitude sensors used to measure changes in the spacecraft orientation while CMGs are used to generate control torques to change and maintain spacecraft's orientation. Figure 2.24, [8] shows the construction geometry of mechanical gyros.

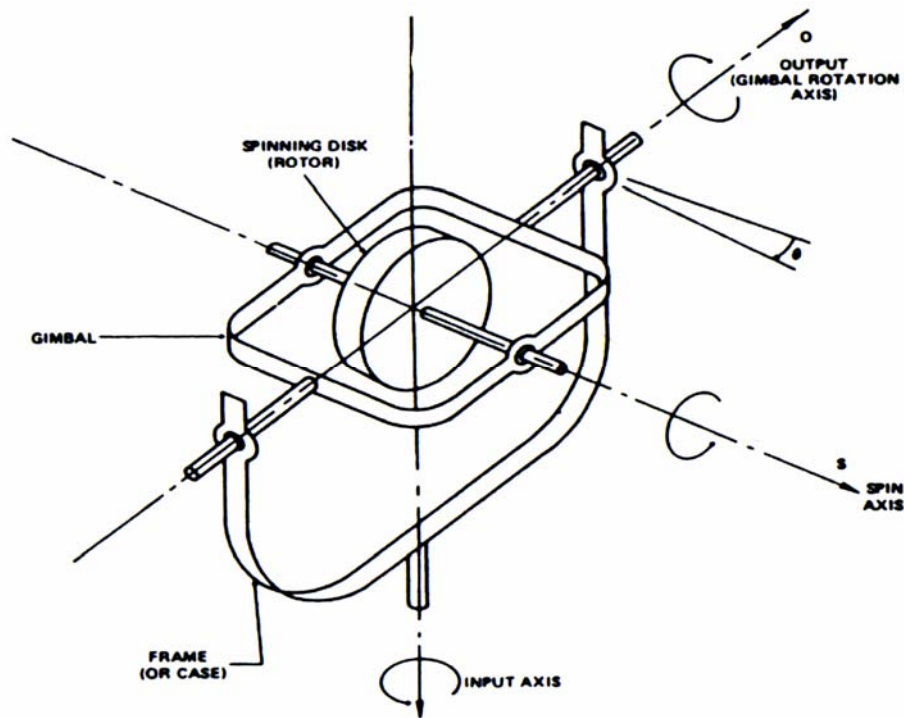


**Figure 2.24:** Basic Single-Degree-of-Freedom Gyroscope Construction Geometry.

The angular momentum of a gyro, in the absence of an external torque, remains constant in magnitude and direction in space. Therefore, any rotation of the spacecraft about the gyro's input axis results in a precession of the gimbal about the output axis. Motion of the gimbal about the output axis will then cause an output signal from the RG or RIG. If a gyro spin axis is supported by only one gimbal, it is sensitive in only one direction, and hence it is a single degree of freedom (SDOF) gyro. Figure 2.24 is an example of such a gyro. If, however, the spin axis is supported by two gimbals, the sensor sensitivity is supported in two directions, it is a two degree of freedom, or TDOF, gyro. Three

or more SDOF gyros or two or more TDOF gyros provide attitude information about all three axes.

### **2.1.5.1 Sensor Types**

Rate Gyros measure spacecraft's angular rates and frequently part of a feedback system for either spin rate control or attitude stabilization. If the spacecraft rotates about the RG input axis, the gimbals rotate about the output axis and hence the gyros generate an output signal. This output is proportional to the spacecraft rotation rate about the gyro input axis. That's the output of a rate gyro is obtained by measuring the rotation of the gimbal about the rotation axis. The relationship between the rate about the input axis and the angular displacement,  $\theta$ , about the output axis may be derived by the total angular momentum,  $H$ , of the gyro system, [8]. The related mathematical equations can be found in Appendix A.

Rate gyros are simplest and least expensive gyros and their accuracy is usually good enough for spin rate control. But their integrated output requires frequent correction for precise attitude determination using other sensors such as Sun sensors or Star trackers. Although RGs only provide rotation rate information, their output could be fed into on board computers and integrated to give angular displacement from some reference time or position.

Rate integrating gyros have high accuracy and low drift characteristics. Therefore, they are more frequently used in spacecraft attitude determination. The output of a RIG is not an angular rate but an angular displacement. This output is proportional to the spacecraft angular displacement about the sensor input axis relative to some reference position. Different mechanical or electrical methods can be used to measure the rotation of the spacecraft about the input axis. As in RGs, Star tracker data can be used to calibrate and correct RIG output periodically. Since RIG output is an angular displacement, small angular

displacements over small time intervals are measured electronically and divided by the time increment to obtain an average rotation rate over that time interval.

Control moment gyros (CMG) are not attitude sensors like RIG but are used to generate attitude control torques in response to onboard or ground command. Control moment gyros operates essentially in reverse manner when compared to RGs or RIGs. A commanded displacement of the gimbal and the resultant change in the angular momentum vector causes a control torque about the gyro's input axis. The magnitude of this torque depends on the speed of the rotor and the gimbal rotation rate. Gimbal rotation rates must not exceed specified maximum values so a partitioning among several CMGs is often required. If undesirable momentum configurations result in momentum dumping, an auxiliary control system (e.g. gas thrusters) must be added to the system design. CMGs work much like reaction wheels. They may be used in conjunction with RGs or RIGs. Because their weight and expense, they are generally used on large spacecrafts. Two, three or more gyros can be used to provide control and sensing about all three axis. So complete three-axis information is provided. Figure 2.25 shows an example of configuration of control moment gyros.

Sometimes, several (up to four) RIGs are applied together to sense position and velocity more accurately. The combination of these RIGs are called as Inertial Reference Unit (IMU) and they work with accelerometers. Figure 2.26 gives examples for these units.

Gyroscope's mathematical model and calculation of angular velocity can be found in Appendix A in detail.

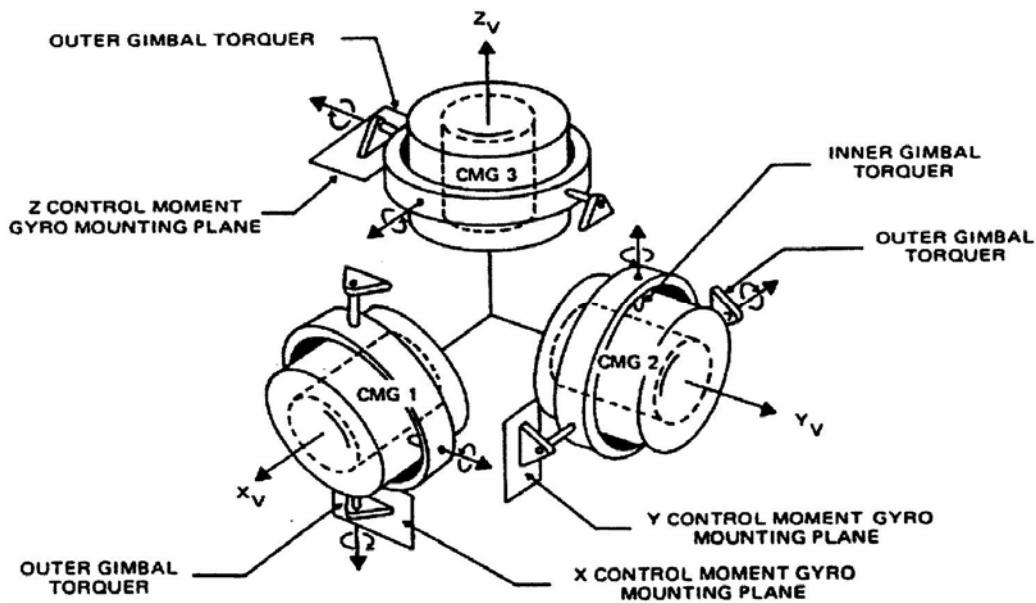


**Figure 2.25:** Configuration of Control Moment Gyros in Three Axis.



**Litton LN-200S IMU**

Uses Fiber Optic Gyro (FOG)

3.5 by 3.4 inches, 1.65 pounds  
 12W nominal, regulated 5 Vdc and 15Vdc  
 Survival Temperature Range: -62deg. to +85deg. C  
 Performance Temperature Range: -54deg. to +71deg.  
 Vibration (survival): 15g rms random  
 Shock: 400g/100 Hz; 1,500g/1000 Hz



**Litton SIRU-Core\***

Uses Hemispherical Resonator Gyro (HRG)

12.8 by 8.6 by 4.5 inches, 12 pounds  
 22W, 28 or 70 Vdc  
 Survival Temp Range: -34 to +71 degrees C  
 Performance Temp Range: -24 to +55 degrees C  
 Vibration (survival): 20g rms  
 Shock: Pyrotechnic  
 Radiation Hardness: 100 krad

**Figure 2.26:** Different IMU Configurations and Their Technical Data.

In conclusion, Table 2.2 [25] gives typical performances and technical properties of some sensor types.

**Table 2.2:** Typical Performance Ranges and Technical Properties of Sensors.

Sensor	Typical Performance Range	Weight (kg)	Power(W)
<b>Inertial Measurement Unit (Gyros and accelerometres)</b>	Gyro Drift=0.003 deg/hr to 1 deg/hr	2 to 25	10 to 2000
<b>Sun Sensors</b>	0.005 deg to 3 deg	0.5 to 2	0 to 3
<b>Star Trackers (scanners and mappers)</b>	0.000278 deg to 0.0167 deg	3 to 7	5 to 20
<b>Horizon Sensor Scanners</b>	0.1 deg to 1 deg	2 to 5	5 to 10
<b>Fixed Head</b>	(-0.1)deg	2.5 to 3.5	0.3 to 5

Accuracy of different types of sensors are given in Table 2.3 [8].

**Table 2.3:** The Accuracy of Different Types of Sensors.

Sensor	Accuracy	Characteristics and Applicability
<b>MAGNETOMETERS</b>	1.0° (5,000 km alt) 5° (200 km alt)	Attitude measured relative to Earth's local magnetic field. Magnetic field uncertainties and variability dominate accuracy. Usable only below ~6,000 km.
<b>EARTH SENSORS</b>	0.05° (GEO) 0.1° (low altitude)	Horizon Uncertainties dominate accuracy. Highly accurate units use scanning.
<b>SUN SENSORS</b>	0.01°	Typical field of view ±130°
<b>STAR SENSORS</b>	2 arc sec	Typical field of view ±16°
<b>GYROSCOPES</b>	0.001°/hour	Normal use involves periodically resetting the reference position.

## 2.2. Attitude Actuators

As mentioned before, an actuator is the mechanism that supplies control torque for the attitude control system. In active control systems, continuous decision making and hardware operation is needed. The most common sources of torque are gas jets, electromagnets and reaction wheels. Passive attitude control makes use of environmental torques to maintain spacecraft orientation. Gravity gradient boom and solar sails are common passive actuators. Decision to use either active, passive methods depends on mission pointing and stability requirements, interaction of control system with onboard experiments or equipment, power requirements, weight restrictions, mission orbital characteristics, and the control system's response time.

### 2.2.1 Momentum and Reaction Wheels

Reaction wheels, momentum wheels, or control momentum gyros are devices used for the storage of angular momentum. They are simply used on spacecraft for several aims: to add stability against disturbance torques, to absorb cyclic torques, and to transfer momentum to the satellite body for slewing maneuvers. They usually depend on the momentum of a spinning wheel,  $h = I\omega$ , where  $I$  is the moment of inertia about the rotation axis and  $\omega$  is the angular velocity. *A flywheel is any rotating wheel or disk used to transfer or store momentum*, [8]. Momentum wheel is a flywheel which operates at a biased momentum. It is capable of storing a variable momentum about its rotation axis, which is usually fixed in the vehicle. Reaction wheel is also a flywheel which operates at zero bias. Control moment gyro consists of a single- or double-gimbaled wheel spinning at a constant rate. The gimbal rings allow the control of the direction of the flywheel momentum vector in the spacecraft body. As stated above, under the name of momentum wheels, these devices are generally used to control the spin rate and attitude about the wheel axis.

Momentum wheel assembly consists of a flywheel and its components: bearings, torque motors, tachometers, control electronics, and other sensing devices, [8]. Torque motors are used to transfer momentum between the wheel and the spacecraft body. Tachometers measure the wheel speed. They usually consist of a wheel-mounted magnet and a fixed sensor, such as a simple pick off coil. The output of the tachometer, which is a pulse train, can be converted to a DC voltage to use as a controlling error signal for either a constant speed or variable speed mode. DC tachometer uses the back electromotive force generated by the armature winding to produce an analog voltage proportional to the rotational speed, [8].

Bearing noise, jitter, quantization, variation of the bearing friction with temperature, offset of the wheel axis from the body principal axis are the practical problems in the design of momentum wheel systems. Also, in switching from the spinning to the despun mode, attitude control problems may occur. This is because of the difficulty in achieving pitch lock if the body rate is too high. The problems stated above are explained in Reference [8].

### **2.2.1.1 Momentum Wheels**

Momentum wheels are similar to reaction wheels except their spin rate can not be varied or reversed. The concept behind this device is that by adding or removing energy from a flywheel, a torque is applied to a single axis of the spacecraft, causing it to react by rotating, [8]. A typical momentum wheel is given in Figure 2.27.



**Figure 2.27:** A Typical Momentum Wheel Configuration.

In some satellites horizon scanners are incorporated as an integral part of the momentum wheel assembly.

A momentum bias design is common for dual-spin Earth-orbiting spacecraft. This kind of spacecraft has two sections with different spin rates. These sections are usually a despun section and a flywheel. A momentum wheel is mounted along the pitch axis, which is controlled to orbit normal. This allows the instruments to scan over the Earth. For example, the SAS-3 spacecraft uses its reaction wheel for different modes: spin rate control mode using gyro rate sensing, Earth-oriented mode using horizon scanner pitch data, and a three axis stabilized mode using star camera data for pitch control [Mobley, et al., 1974].

### **2.2.1.2 Reaction Wheels**

Reaction wheels are simple disks (rotors) that are spun by an electric motor. When the motor applies a torque to speed up or slow down the rotor, it produces a reacting torque on the body of the satellite, [8]. Since the satellite is essentially a closed system, the total angular momentum of the satellite body plus the reaction wheels is constant. Thus any change in the angular momentum of a reaction wheel results in an equal and opposite change of the angular momentum of the satellite body. Figure 2.28 illustrates a typical reaction wheel. Figure 2.29 simply shows the configuration of Ithaco type reaction wheel.

Reaction wheels are effective active control elements. They are particularly good for variable spin rate control. Active control of spacecraft by using reaction wheels is a fast, flexible, precise way of attitude control and stabilization. On the other hand, it requires rapidly moving parts which implies problems of support and friction. A second control system may be needed to control the overall angular momentum in response to changes in the environmental torques. An essential difference between momentum wheels and reaction wheels is that reaction wheels operate with zero

momentum bias. They are used primarily for absorbing cyclic torques and temporarily storing momentum from the body during slew, or reorientation maneuvers. On the other hand, secular disturbance torques can cause saturation in the momentum storage capacity.

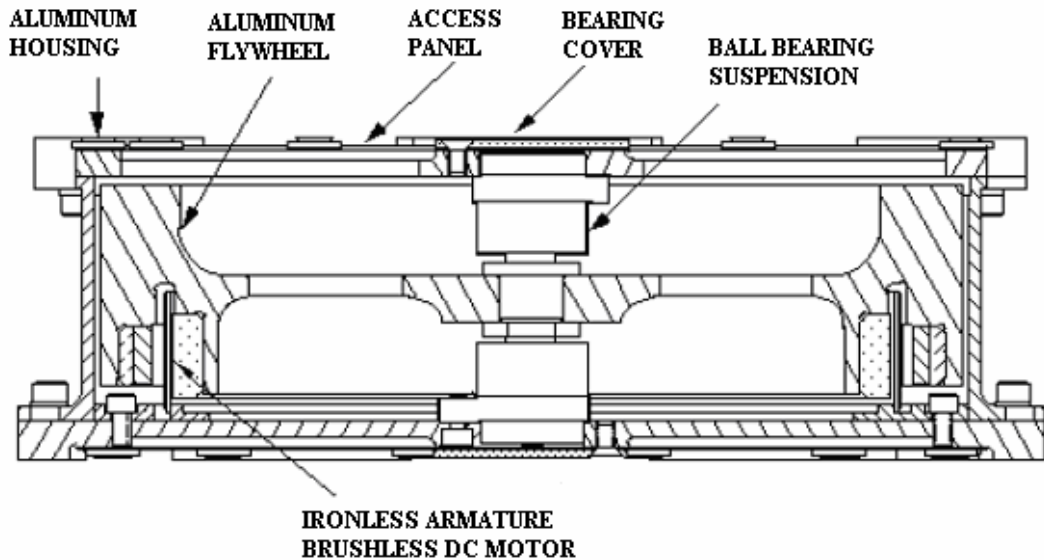
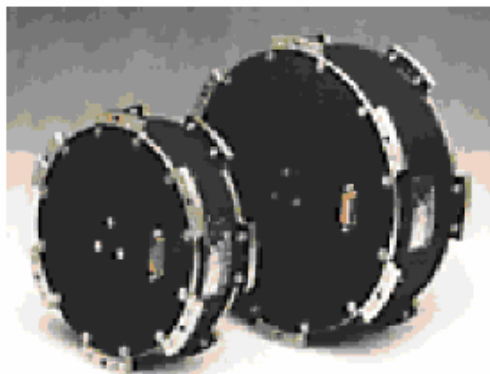


**Figure 2.28:** Typical Reaction Wheel Configuration.



**Ithaco Type A & B**

2 to 19.5 Nms  
 28 cm d x 13.5 cm, 8.4 kg, 10 W (steady state @ 1000 rpm) 350 W (peak)  
 All maximums

**Figure 2.29:** Ithaco Type Reaction Wheel Configuration and Physical Properties.

One reaction wheel can affect the satellite's momentum along only one axis. To control the satellite along all three axes at least three reaction wheels are required. A system of four reaction wheels can be used to provide redundancy and also makes it possible to change the reaction wheel speeds without causing any net torque (By making the torques from the four reaction wheels cancel each other). In Figure 2.30, reaction wheels in tetrahedral configuration is shown, [26].

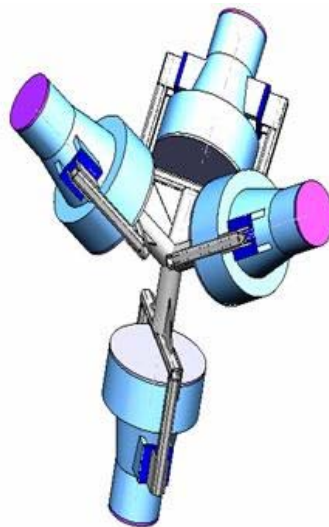


**Figure 2.30:** Typical Tetrahedral Configuration of Reaction Wheels, [26].

In three axis stabilized systems, gyroscopes are usually used to sense and feedback any motion to the wheel motors on each axis. Then, the torque motors apply a compensating torque to each reaction wheel, which absorbs the effect of the disturbance torques such as secular disturbance torques. When the wheels are near saturation , the angular momentum is adjusted using gas jets or magnetic coils.

A slew, or attitude reorientation maneuver, can be applied using the set of reaction wheels to rotate the body about the given axis. The angular momentum vector inertially remains fixed, on the other hand the attitude angles change as the angular momentum vectors change in body-fixed coordinate system as shown in Figure 2.31, [8].

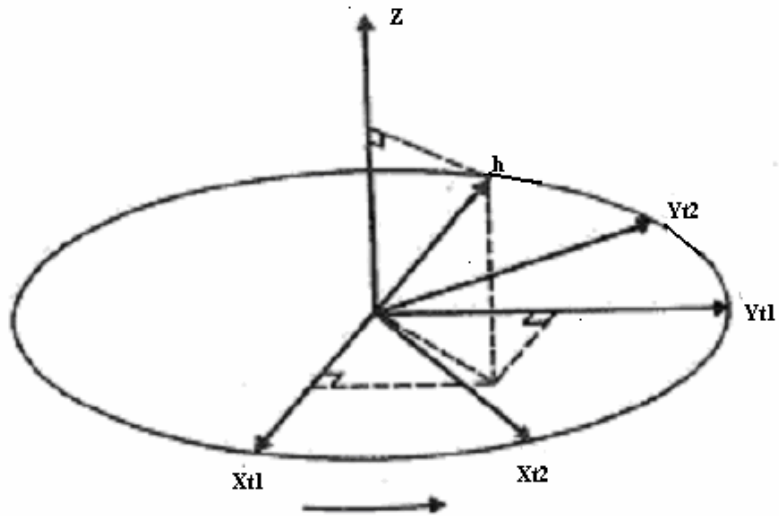


**Figure 2.31:** A Slew Rotation about z Axis in Inertial Space: x Axis has to absorb additional momentum when moving to its location at  $t_2$ .

The advantages of a three-axis stabilized reaction wheel system are: (1) achieving continuous high-accuracy pointing control, (2) compensation of disturbance torques, (3) Angle slewing maneuvers without fuel consumption.

Models of reaction wheel torque and friction characteristics are needed to model the reaction wheel control system. The torque level in reaction wheel is controlled by varying the duty cycle, or fraction of each half-cycle in which the applied square-wave voltage is non-zero. In Figure 2.32, duty cycle,  $X_{dc}$ , as a function of control voltage,  $V$  is shown, [8].

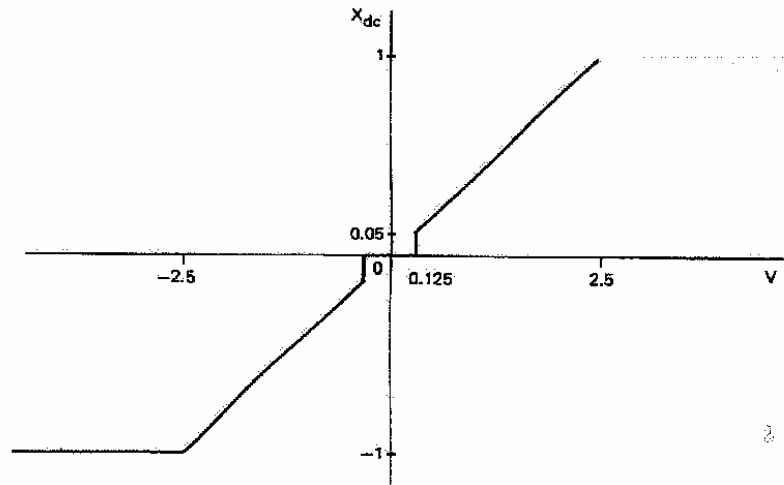


**Figure 2.32:** Duty Cycle,  $X_{dc}$ , as a Function of Control Voltage,  $V$ .

The net torque on the wheel is given by, [8],

$$N = X_{dc} N_{em} - N_{friction} \quad (2.2)$$

where  $N_{em}$ , is the applied electromagnetic torque when the duty cycle is unity,  $N_{friction}$  is the bearing friction torque, depending on the wheel speed,  $s$ . For less precise calculations, [8];

$$N_{em} = 2N_o \alpha r (\alpha^2 + r^2)^{-1} \quad (2.3)$$

The dependence of  $N_{em}$  on  $s$  is shown in Figure 2.33, [8].

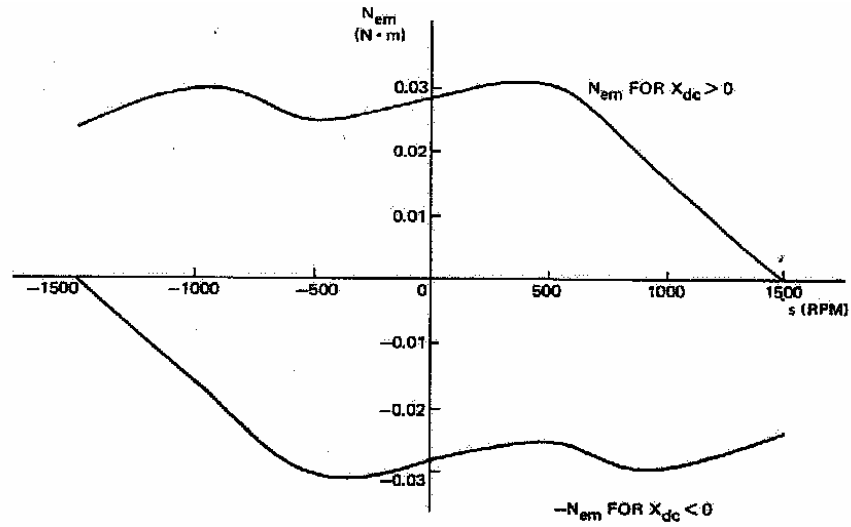


**Figure 2.33:** Applied Torque as a Function of Wheel Speed.

Where  $r = 1 - s/s_{\max}$  for  $X_{dc} > 0$  ;  $r = 1 + s/s_{\max}$  for  $X_{dc} < 0$ .  $N_o$  is the maximum magnitude of  $N_{em}$  [8].

The friction torque can be modelled as [8],

$$N_{friction} = N_c \operatorname{sgn}(s) + f_s \quad (2.4)$$

$N_c$  is the Coulomb friction coefficient and  $f$  is the viscous friction coefficient.

Configurations of four reaction wheels provide control even if one wheel fails. If more than more than three wheels operate simultaneously, a **steering law** is needed to distribute the momentum between wheels during a maneuver. An example steering law is given below in Equation 2.22. The total angular momentum of the four wheel is expressed as , [23], [8] :

$$h_{tot} = A[h_1, h_2, h_3, h_4]^T \quad (2.5)$$

where  $h_i$  is the magnitude of the momentum of  $i^{\text{th}}$  wheel and the transformation matrix,  $A$ , depend only on the mounting angles of the wheels. Pseudoinverse of  $A$ , where  $A^R \equiv A^T(AA^T)^{-1}$  is used in steering law. The wheel torque four-vector,  $N$ , is given by [23], [8],

$$N = A^R N_c + k(1, -1, -1, 1)^T \quad (2.6)$$

where  $N_c$  is the control torque vector in body coordinates, the vector  $(1, -1, -1, 1)^T$  shows the specific wheel geometry along the diagonals of octants with positive  $x$ , and  $k$  is an arbitrary scalar which signifies the one remaining degree of freedom. For detailed information please see References [23], [8].

### 2.2.2 Magnetic Torquers

Magnetic torquers are generally coils of uniform wire, [8]. When a voltage is applied across a coil winding, a current is created, which creates a magnetic dipole. The strength and the direction of the dipole depends on the amount and direction of the current flowing through windings, the number of turns of wire, and the total area enclosed by the coil. Magnetic moment for a coil of one turn is given by [8],

$$m = IAn \quad (2.7)$$

where current  $I$  is flowing through wire loop enclosing an area of  $A$  and  $n$  is a unit vector normal to the plane of the loop.

The magnetic dipole moment depends on the material enclosed by the current carrying loop and is given by , [8],

$$d = \mu m \quad (2.8)$$

where  $\mu$  is the permeability of the core material. So magnetic dipole moment turns out to be, [8] ;

$$d = \mu(NI)An \quad (2.9)$$

Parameters such as coil configuration,  $N$  and  $A$ ; current level  $I$  ; and the core material  $\mu$  must be selected properly in order to generate a proper amount of dipole. In design level, limitations on weight, power consumption should be considered. Core material selection is the most essential decision. Materials with high permeabilities will result in loss of power. Ferromagnetic materials can cause nonlinearity and hysteresis as these materials have magnetization curves which saturate at relatively low values of applied magnetic field intensity. Air cores are generally applied in satellites. The material of current-carrying element is chosen according to weight restrictions and ability to dissipate the heat generated by the current.

Magnetic torquers are generally used to generate magnetic dipole moments for attitude and angular momentum control. They are also used to compensate residual spacecraft biases and to counteract attitude drift due to environmental disturbance torques. They are widely preferred since they are reliable and accurate according to the mission of the satellite. They have low power consumption. On the other hand, they are effective in near Earth orbit only and applicability is limited by the direction of the external magnetic field. Figure 2.34 shows a magnetic torquer with the resultant magnetic field vector and force.

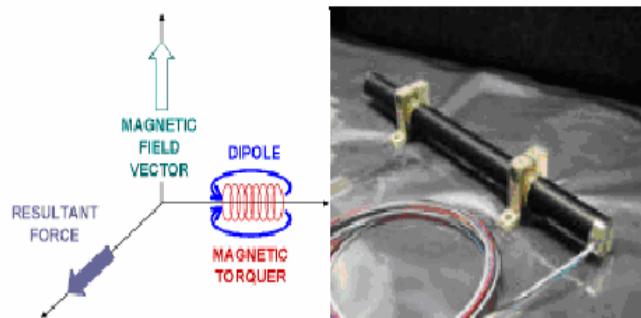


**Figure 2.34:** Magnetic Torquer with Resultant Force Vector.

### 2.2.3 Gravity Gradient Boom

Gravity gradient is used in stabilization mode as a passive attitude control method. Basic requirement in applying gravity boom is that the gravity gradient torque must be greater than all other environmental torques. They require no power from satellite and maintain stable orientation relative to central body such as Earth, or Moon. But their control accuracy is limited to 1 degree.

Figure 2.35 gives an illustration of the SSTL-Weitzmann 6 m deployable boom used in BILSAT-1.

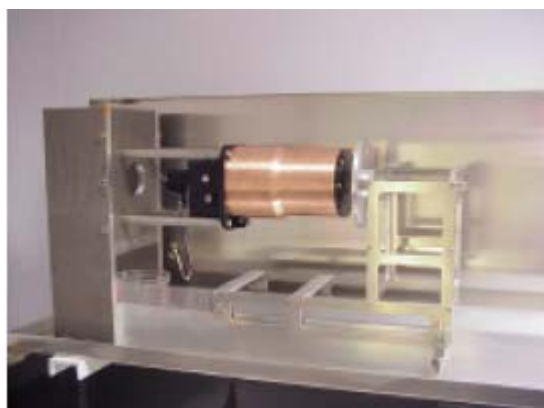


**Figure 2.35:** SSTL-Weitzmann 6 m. Deployable Boom.

## 2.2.4 Gas Jets

All jets or thrusters produce thrust by expelling propellant in the opposite direction. Gas jets can be hot gas, when energy is derived from a chemical reaction or cold gas type when energy is derived from the latent heat of a phase change.

The obtained torques or forces can be used to control attitude, spin rate, nutation, speed of momentum wheels, and to adjust orbits. Gas jets or magnetic coils can be used for the same purposes at low Earth orbits. The control algorithms are simpler than those for magnetic coils since jets produce larger torques. The magnetic torque produced by magnetic coils depends on the local magnetic field. The local magnetic field varies as the spacecraft moves in its orbit. On the other hand, jets don't change behavior according to the environment. The main limitation on the use of jets is the required propellant supply. Fuel budget is an important part of mission planning for any system using gas jets. Gas jets also have complex and expensive plumbing systems. In higher orbits, gas jets are used for interchanging momentum with the environment.

Figure 2.36 gives an example of cold gas jet.

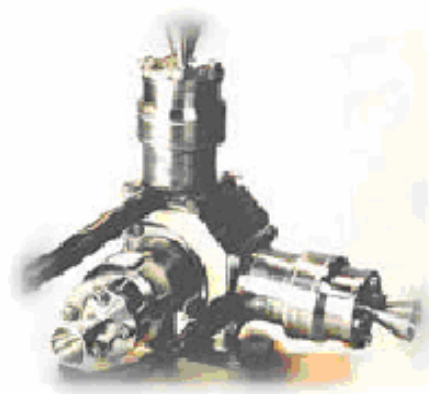


**Figure 2.36:** Cold Gas Jet.

Table 2.4, [25], generally summarizes the properties of some of the actuators.

**Table 2.4:** Typical Actuators and Their Technical Properties

<b>Actuator</b>	<b>Typical Performance Range</b>	<b>Weight (kg)</b>	<b>Power(W)</b>
<b>Thrusters</b>			
<b>Hot Gas</b>	0.5 to 9000 N	Variable	n/a
<b>Cold Gas</b>	<5 N	Variable	n/a
<b>Reaction and Momentum Wheels</b>	0.4 to 400 Nms for momentum wheels at 1200 to 5000 rpm Max. Torques from 0.01 to 1 Nm	2 to 20	10 to 110
<b>Control Moment Gyros</b>	0.25 to 500 Nm of torque	>40	90 to 150
<b>Magnetic Torquers</b>	10 to 4000 Am <sup>2</sup>	0.4 to 50	0.6 to 160

### 2.3 Summary

In summary, the sections expressed above briefly describes the attitude control and determination components. The facts given above can be applied in design steps for the selection of correct components through mission constraints. Data sheets of some of the attitude control and determination components applied in BILSAT-1 project are given in Appendix B.

## CHAPTER III

### ATTITUDE DYNAMICS AND SOME LINEAR CONTROL TECHNIQUES

This chapter gives information about the mathematical modelling of a satellite and its environment. It briefly explains reference frames for attitude modelling, attitude representations, environmental torques and Earth's magnetic field. Being informed about the basic definitions about satellite, dynamics and kinematics of the satellite are investigated. Lastly, some linear control techniques, applied in this thesis, are defined. The techniques studied for attitude control are linear controller and linear quadratic regulator.

#### 3.1 Mathematical Definitions

In order to design a reliable attitude model for the spacecraft, careful development of motion equations are needed. The mathematical model of the satellite and its environment can be developed in a number of different reference frames. In this part, mathematical knowledge to develop the satellite's mathematical model is explained in a short manner. Detailed information about these definitions can be found in Reference [7], [23], [21], [26].

##### 3.1.1 Keplerian Orbits

Predicting the motion of the Sun, Moon, and planets was a major part of the scientific revolution of the Sixteenth and Seventeenth centuries. In the Keplerian model, satellites orbit in an ellipse of constant shape and orientation. The Earth is at one focus of the ellipse, not the center (unless the orbit ellipse is actually a perfect

circle). Newton derived Kepler's three laws of planetary motion by using gravitational theory and his law of mechanics. These three laws are summarized below:

**First Law:** *The orbit of each planet is an ellipse, with the Sun at one focus.*

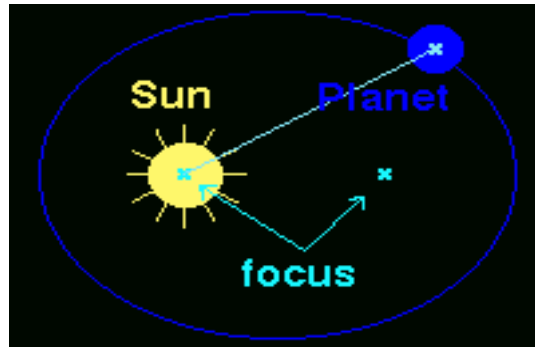


**Figure 3.1 :** Configuration of Kepler's First Law.

**Second Law:** *The line joining the planet to the Sun sweeps out equal areas at equal times.*

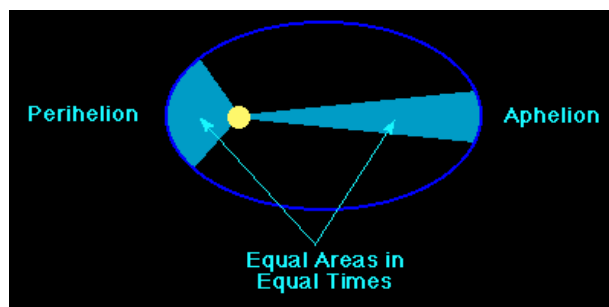


**Figure 3.2:** Configuration of Kepler's Second Law.

**Third Law:** *The square of the period of a planet is proportional to the cube of its mean distance from the Sun.*  $\left(\frac{P_1^2}{A_1^3} = \frac{P_2^2}{A_2^3}\right)$

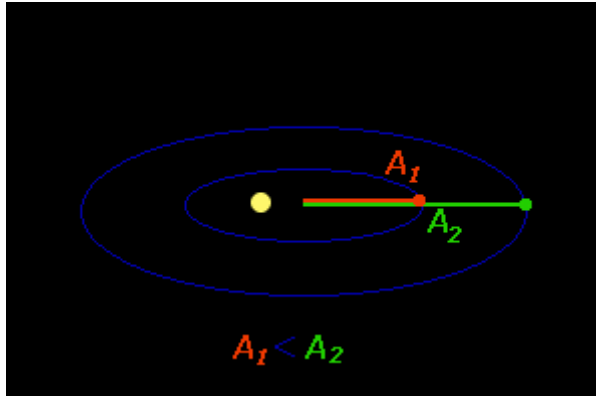


**Figure 3.3:** Configuration of Kepler's Third Law.

These laws also can be applied to the satellite motion in Earth orbit. For further information on Keplerian orbits and a satellite in elliptical Earth orbit see Reference [8].

### 3.1.2 Reference Frames

This section explains different reference frames for representing satellite's position and attitude.

#### 3.1.2.1 Earth-Centered Inertial (ECI) Frame

The Earth-centered inertial frame (ECI) is an inertial frame for terrestrial navigation. The frame is fixed in space, which means that it is a non-accelerated reference frame in which Newton's Laws are valid. The origin of the frame is oriented at the center of Earth. The x-axis points toward the point where the plane of the Earth's orbit toward Sun, crosses the Equator going from South to North, z-axis points toward the North pole and y-axis completes the right hand Cartesian coordinate system. Velocity of the orbit frame and the motion of the Sun can be directly compared to this frame and all different satellite motions can be presented in this frame. This frame is denoted by I.

### **3.1.2.2 Earth-Centered Earth Fixed (ECEF) Frame**

The origin of this frame is located at the center of the Earth. The x- and y-axes rotate about the z-axis relative to the ECI frame. Rotation has a rate of  $\omega_e = 7.2921 \times 10^{-5}$  rad/s. Magnetic field around the Earth, IGRF, can be used with an orbit estimator to create a reference model by the help of this frame. The frame is denoted by E.

### **3.1.2.3 Earth-Centered Orbit Frame**

The Keplerian elements are given in this frame. Then Keplerian elements can be used with an orbit estimator to model the magnetic field. The x-axis points toward the perigee, y-axis along the semiminor axis and z-axis is perpendicular to the plane. The frame is denoted as OC.

### **3.1.2.4 Orbit Frame**

Orbit frame rotates relative to the ECI frame, with a rate of  $\omega_o$  depending on the altitude of the satellite. The origin is at the center of mass of the satellite. The y-axis is toward the direction of motion tangentially to the orbit. The tangent is only perpendicular to the radius vector in circular orbit, not align with the velocity vector of the satellite in elliptical orbits. The z-axis points toward the center of Earth, and the x-axis completes the right hand system. The orbit frame is denoted as O. Figure 3.4 shows the axis notation.

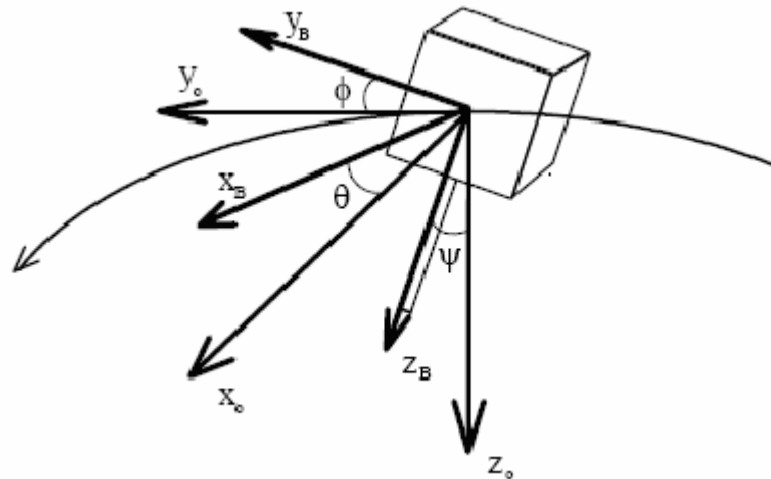


**Figure 3.4 :** The Body and Orbit Reference Frames.

### 3.1.2.5 Body Frame

This frame is a moving reference frame which is fixed on the satellite. The orientation of the satellite is determined relative to the Orbit frame, while angular velocities are expressed in Body frame. The x-axis forward and z-axis is downward , y-axis completes the right hand orthogonal system. The origin is at the center of the mass of the satellite. It is denoted as B. Figure 3.5 shows the axis notation. For further information on reference frames, see Reference [26].

## 3.2 Attitude Representation

This section describes the transformation principals between different reference frames, and it also expresses Euler equations, quaternions, inertia matrix.

### 3.2.1 Representing Attitude Information

The satellite attitude is referenced to Earth-Fixed reference frame in order to obtain angle data from angular velocity in body fixed frames, so a conversion method is needed to demonstrate the velocity vector correctly. Euler angle transformation is

one of the methods applied in transformation. Although this method is reliable, simple and accurate enough for applications, sometimes singularities occur in coordinate transformations. In order to avoid singularities, Quaternion representation can be used as representation method. Also it increases the computation speed, which is critical for navigation applications. On the other hand, it's sometimes hard to visualise the actual angles. In below sections, both representations are expressed briefly. In this thesis, quaternion method is used to represent attitude information.

### 3.2.1.1 Euler Angle Representation

Euler [17], reasoned that any rotation from one frame to another can be visualized as a sequence of three simple rotations about base vectors. The other Euler contribution is the theorem [17] given below that tells us that only one rotation is necessary to reorient one frame to another.

***Euler's Theorem*** . *The most general motion of a rigid body with a fixed point is a rotation about a fixed axis.*

Euler angle transformation can be presented by using roll, pitch, yaw angles. These angles help to determine the attitude of the satellite relative to the Orbit frame. The roll angle is a rotation angle  $\theta$  about the  $x_0$ -axis, the pitch angle a rotation angle  $\phi$  about the  $y_0$ -axis and lastly, the yaw angle is a rotation angle  $\psi$  about the  $z_0$ -axis. The main problem with Euler angles is the existence of singularities. To avoid the problem of singularities, a fourth parameter to represent the attitude is introduced. For BILSAT-1 model the roll, yaw, pitch angles are only used as input and output to the simulation, internally quaternions are used.

### 3.2.1.2 Unit Quaternions

Quaternions or Euler parameters are used in computations in order to overcome the singularity problem in the attitude representation. Euler parameter,  $\mathbf{q}$  is a complex number with one real part,  $\eta$ , and three imaginary parts,  $\boldsymbol{\varepsilon}$ , defined by [7],

$$\begin{aligned} \eta &= \cos \frac{\theta}{2} \quad ; \quad \boldsymbol{\varepsilon} = [\varepsilon_1 \quad \varepsilon_2 \quad \varepsilon_3]^T = \lambda \sin \frac{\theta}{2} \\ q &= [\eta \quad \varepsilon_1 \quad \varepsilon_2 \quad \varepsilon_3]^T \end{aligned} \quad (3.1)$$

where  $\theta$  is the rotation about the unit vector  $\lambda$ . The unit quaternions satisfy the constraint  $\mathbf{q}^T \mathbf{q} = 1$ , which means that

$$\eta^2 + \varepsilon_1^2 + \varepsilon_2^2 + \varepsilon_3^2 = 1 \quad (3.2)$$

The conversions between unit quaternions and Euler angles are given in Appendix A.

### 3.3 Rotation Matrix

The rotation matrix can behave as a transformation of a vector represented in one coordinate frame to another frame, as a rotation of a vector within the same frame and finally as a description of mutual orientation between two frames. The rotation matrix  $R$  from frame  $a$  to  $b$  is denoted  $R_a^b$ . The rotation of a vector from one frame is written with the following notation:

$$x^{to} = R_{from}^{to} x^{from} \quad (3.3)$$

Angle-axis parameterization, is a way of parameterization of the rotation matrix, given in Equation 3.3 as  $R_{from}^{to}$ ,  $R_{\lambda, \theta}$ , corresponding to a rotation  $\theta$  about the  $\lambda$ -axis [8], [26]:

$$R_{\lambda,\theta} = I + S(\lambda) \sin \theta + (1 - \cos \theta)S^2(\lambda) \quad (3.4)$$

where S is the skew-symmetric operator and defined in Appendix A. The rotation matrix also satisfies :

$$R_a^b = (R_b^a)^{-1} = (R_b^a)^T \quad (3.5)$$

Rotations using Euler angles, are defined as :

$$R_x(\varphi) = \begin{bmatrix} 1 & 0 & 0 \\ 0 & \cos \varphi & \sin \varphi \\ 0 & -\sin \varphi & \cos \varphi \end{bmatrix} \quad (3.6)$$

$$R_y(\theta) = \begin{bmatrix} \cos \theta & 0 & -\sin \theta \\ 0 & 1 & 0 \\ \sin \theta & 0 & \cos \theta \end{bmatrix} \quad (3.7)$$

$$R_z(\phi) = \begin{bmatrix} \cos \phi & \sin \phi & 0 \\ -\sin \phi & \cos \phi & 0 \\ 0 & 0 & 1 \end{bmatrix} \quad (3.8)$$

The rotation matrix has the orthogonality property,

$$R_a^b \cdot (R_b^a)^T = I \quad (3.9)$$

### 3.3.1 Transformation Between Different Frames

The different rotations between frames are described briefly here.

#### 3.3.1.1 Transformation from Earth Centered-Orbit to ECI And ECEF Frames

The rotation transformation between these frames is done by using the orbit estimator. The rotation, [19] is done,

$$\begin{aligned} R_{OC}^I &= R_z(-\Omega) R_x(-\iota) R_z(-\omega) \\ R_{OC}^E &= R_z(-\Omega + \theta) R_x(-\iota) R_z(\omega) \end{aligned} \quad (3.10)$$

where  $\Omega$  is the right ascension of ascending node,  $\iota$  is the inclination of the satellite,  $\omega$  is argument of perigee, and  $\theta$  is the ascension of the zero meridian.

#### 3.3.1.2 Transformation from ECEF to ECI Frame

This transformation is a rotation about the coincident  $z_I$  and  $z_E$ -axes, equal to an angle  $\alpha = \omega_e t$  where  $\omega_e$  is the Earth rotation rate, and  $t$  is the time passed until the ECEF and ECI frame were aligned. The rotation is [18],

$$R_E^I = R_{zI}^\alpha = \begin{bmatrix} \cos \alpha & \sin \alpha & 0 \\ -\sin \alpha & \cos \alpha & 0 \\ 0 & 0 & 1 \end{bmatrix} \quad (3.11)$$

### 3.3.1.3 Transformation from ECI to Orbit Frame

The orbit frame is rotated about  $y_I$  axis with an angle of  $\beta$  and is expressed as  $\beta = \beta_0 + \omega_0 t$ , where  $\omega_0$  is the satellite rotation velocity,  $\beta_0$  is latitude position (drop angle) and  $t$  is the time since last passing of  $0^\circ$  latitude. The rotation is defined as, [18],

$$R_{y_I, \beta} = \begin{bmatrix} \cos \beta & 0 & \sin \beta \\ 0 & 1 & 0 \\ -\sin \beta & 0 & \cos \beta \end{bmatrix} \quad (3.12)$$

According to the relation between Orbit frame and ECI frame, the following rotation about  $x_I$  axis can be obtained:

$$R_{x_I, \pi} = \begin{bmatrix} 1 & 0 & 0 \\ 0 & \cos \pi & -\sin \pi \\ 0 & \sin \pi & \cos \pi \end{bmatrix} = \begin{bmatrix} 1 & 0 & 0 \\ 0 & -1 & 0 \\ 0 & 0 & -1 \end{bmatrix} \quad (3.13)$$

combining with Equation 3.17, total rotation to transform a vector in ECI frame to Orbit frame:

$$R_I^O = R_{x_I, \pi} R_{y_I, \beta} = \begin{bmatrix} \cos \beta & 0 & \sin \beta \\ 0 & -1 & 0 \\ \sin \beta & 0 & -\cos \beta \end{bmatrix} \quad (3.14)$$

where  $\beta$  is the latitude of the satellite.

### 3.3.1.4 Transformation from Orbit to Body Frame

The attitude of the satellite can be determined by estimating the rotation matrix between Orbit and Body frame,  $R_o^b$ . A representation of the rotation from Orbit to Body frame can be calculated as, (Appendix A), [7], [23], [26]:

$$R_o^b = I + 2\eta S(\varepsilon) + 2S^2(\varepsilon) \quad (3.15)$$

$$R_o^b = (R_o^o)^T = \begin{bmatrix} 1 - 2(\varepsilon_2^2 + \varepsilon_3^2) & 2(\varepsilon_1\varepsilon_2 + \eta\varepsilon_3) & 2(\varepsilon_1\varepsilon_3 - \eta\varepsilon_2) \\ 2(\varepsilon_1\varepsilon_2 - \eta\varepsilon_3) & 1 - 2(\varepsilon_1^2 + \varepsilon_3^2) & 2(\varepsilon_2\varepsilon_3 + \eta\varepsilon_1) \\ 2(\varepsilon_1\varepsilon_3 + \eta\varepsilon_1) & 2(\varepsilon_2\varepsilon_3 - \eta\varepsilon_1) & 1 - 2(\varepsilon_1^2 + \varepsilon_2^2) \end{bmatrix} \quad (3.16)$$

For more details see Reference [26].

Another way to represent the rotation vector is given below :

$$R_o^b = \begin{bmatrix} c_1^B & c_2^B & c_3^B \end{bmatrix} \quad (3.17)$$

where  $c_i^B = \begin{bmatrix} c_{ix}^B & c_{iy}^B & c_{iz}^B \end{bmatrix}^T$  are column vectors, representing the projections of  $x_o$ ,  $y_o$  and  $z_o$  axes in the body frame.  $c_3^B = \begin{bmatrix} 0 & 0 & \pm 1 \end{bmatrix}^T$  means that the  $z_o$ -axis and  $z_b$ -axis are aligned. This vector is assumed to be deviation between  $z_o$ -axis and  $z_b$ -axis, and this is a sign of the performance of the control system.

## 3.4 Inertia Matrix

The inertia matrix  $I_o \in \mathfrak{R}^{3 \times 3}$  about origin is defined according to [7]:

$$I_o := \begin{bmatrix} I_x & -I_{xy} & -I_{xz} \\ -I_{yx} & I_y & -I_{yz} \\ -I_{zx} & -I_{zy} & I_z \end{bmatrix} \quad (3.18)$$

$$I_x = \int_V (y^2 + z^2) \rho_m dV \quad ; \quad I_{xy} = I_{yx} = \int_V xy \rho_m dV \quad (3.19)$$

$$I_y = \int_V (x^2 + z^2) \rho_m dV \quad ; \quad I_{xz} = I_{zx} = \int_V xz \rho_m dV \quad (3.20)$$

$$I_z = \int_V (x^2 + y^2) \rho_m dV \quad ; \quad I_{yz} = I_{zy} = \int_V yz \rho_m dV \quad (3.21)$$

If principal axes of inertia and the axes of the body frame coincides, then the inertia matrix reduces to :

$$I = \begin{bmatrix} I_x & 0 & 0 \\ 0 & I_y & 0 \\ 0 & 0 & I_z \end{bmatrix} \quad (3.22)$$

Throughout this thesis, inertia matrix is assumed to be diagonal matrix and defined by I. BILSAT-1 inertia matrix parameters are given as,  $I_{xx}=9,8194$ ;  $I_{yy}=9,7030$ ;  $I_{zz}=9,7309$  and applied as the diagonal elements of I in simulations.

### 3.5 Modelling the Earth's Magnetic Field

The performance of the attitude control system can be utilized by the measurement of geomagnetic field with the related sensors, magnetometers. This part briefly describes the two basic magnetic field models; IGRF Model and Dipole Model.

### 3.5.1 The Earth's Magnetic Field

The magnetic field is highly varies over the Earth's surface as can be seen in Figure 3.5. The Earth's magnetic field changes between 25000 nT (nano Tesla) in equatorial regions and 70000 nT at poles.

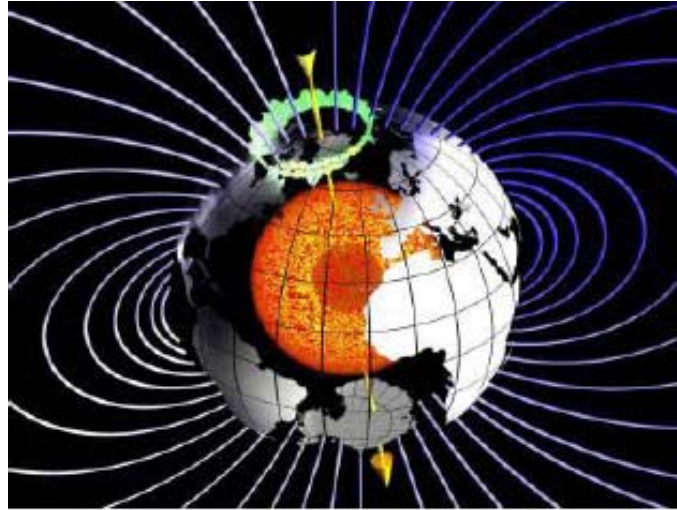


**Figure 3.5:** The Distribution of Earth's Magnetic Field.

#### 3.5.1.1 Mathematical Model

The Earth's magnetic field can be found by the help of the equations expressed below:

$$\nabla \times \mathbf{B} = i\left(\frac{\partial B_y}{\partial z} - \frac{\partial B_z}{\partial y}\right) + j\left(\frac{\partial B_x}{\partial z} - \frac{\partial B_z}{\partial x}\right) + k\left(\frac{\partial B_y}{\partial x} - \frac{\partial B_x}{\partial y}\right) \quad (3.23)$$

$$\mathbf{B} = \left(i \frac{\partial V}{\partial x} + j \frac{\partial V}{\partial y} + k \frac{\partial V}{\partial z}\right) = -\nabla V \quad (3.24)$$

where  $B$  is the Earth's magnetic field,  $\nabla$  is the gradient operator and  $V$  is the scalar potential function and given in Equation 3.25.

$$V(r, \theta, \phi) = a \sum_{n=1}^{\infty} \left(\frac{a}{R}\right)^{n+1} \sum_{m=0}^n P_n^m \cos(\theta) (g_n^m \cos(m\phi) + h_n^m \sin(m\phi)) \quad (3.25)$$

where  $V(r, \theta, \phi)$ , is the potential function of the field about the Earth expressed in spherical harmonics form,  $a$  is the mean radius of Earth,  $P_n^m \cos(\theta)$  are Schmidt quasynormalized associated Legendre functions of degree  $n$  and order  $m$ ,  $g_n^m$  and  $h_n^m$  are the constant gaussian,  $\phi$  and  $\theta$  are the longitude and colatitude (collatitude= $90^\circ$ -latitude).

### 3.5.1.2 IGRF Model

The International Geomagnetic Reference Field, IGRF, computes the theoretical undisturbed Earth's magnetic field at any point on the Earth's surface. IGRF determines the numerical coefficients of the spherical harmonics series given in Equation 3.25. It is updated every fifty year. In simulations, IGRF 2000 model is used. General mathematical equations related to this section can be found in Appendix A.

### 3.5.1.3 Dipole Model

Dipole Model is an alternative way to calculate magnetic field. Although it is not accurate as IGRF model, it can still be applied to the models.

Dipole model of magnetic field is calculated by using the spherical harmonic model to the first degree ( $n = 1$ ) and all orders ( $m = 0, 1$ ).

$$\begin{aligned}
B_r &= 2\left(\frac{a}{r}\right)^3 [g_{1,0} \cos \theta + \sin \theta (g_{1,1} \cos m\phi + h_{1,1} \sin \phi)] \\
B_\theta &= \left(\frac{a}{r}\right)^3 [g_{1,0} \sin \theta - \cos \theta (g_{1,1} \cos m\phi + h_{1,1} \sin \phi)] \\
B_\phi &= \left(\frac{a}{r}\right)^3 [g_{1,0} \sin \phi - h_{1,1} \cos \phi]
\end{aligned} \tag{3.26}$$

Earth's magnetic field can also be found by the following equation. More detailed equations can be found in Reference [21].

$$B = \frac{M}{R^3} \begin{bmatrix} \cos \mu_m \\ 0 \\ 2 \sin \mu_m \end{bmatrix} \tag{3.27}$$

where  $M$  is the Magnetic dipolar moment ( $7.9577 * 10^{15}$ ),  $\mu_m$  is the magnetic latitude and  $R$  is the radial coordinate ( $6971.2 * 10^3$ ).

### 3.6 Modelling Environmental and Actuator Torques

In order to design the attitude control and prediction system, environmental disturbance torques acting on the spacecraft shall be modelled sufficiently. The torques must be modelled as a function of time, the spacecraft's position and attitude so that they can be integrated to Euler's equations and any other mathematical models.

The dominant sources of environmental disturbance torques on the spacecraft attitude are the solar radiation pressure, aerodynamic drag and Earth's gravitational and magnetic fields. There are also internal torques primarily resulted from internal moving hardware, propellant leakage, thrust misalignment and so on.

The solar radiation pressure is effective on attitude of the satellite for altitudes higher than 1000 km. The gravity gradient disturbance are most significant below 1000 km.

Aerodynamic perturbations are most effective below 500 km and negligible over 1000 km altitudes. The effects are shown on Figure 3.6 ([9], [10] and [11]).

The actuators of the satellite produce torques that shall be included in the general equations of motion of the satellite attitude. In this work, torques produced by reaction wheels and magnetic torquers are taken into consideration in mathematical model derivations.

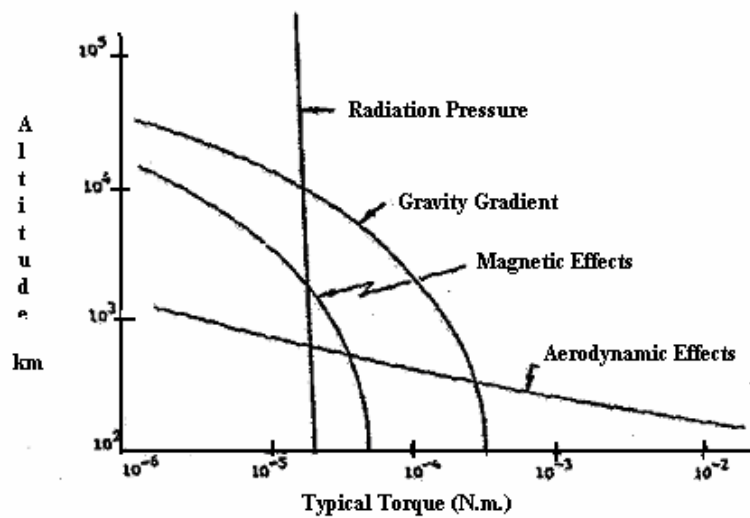


Figure 3.6 : Disturbance Torques as a Function of Altitude.

### 3.6.1 Mathematical Models For Environmental Disturbance Torques

The mathematical modeling of environmental torques are presented in this section. Ideally, the internal torques are avoided in the simulation model of the BILSAT-1. The effects of gravity gradient and aerodynamic flag is taken into consideration at the simulation stage since BILSAT-1 has an altitude of 686 km.

### 3.6.1.1 Gravity Gradient Torque

Any non-symmetrical object in the orbit is affected by a gravitational torque because of the variation in the Earth's gravitational force over the object, [8]. There are many mathematical models for gravity gradient torque, [8]. The most common one is derived by assuming homogeneous mass distribution of the Earth. It is given as, [23], [26] :

$$\tau_{grav} = \frac{3\mu}{R_o^3} u_e \times (Iu_e) \quad (3.28)$$

where  $\mu=3.986 \times 10^{14} m^3/s^2$  is the Earth's gravitational coefficient,  $R_o$  is the distance from Earth's center (m),  $I$  is the inertia matrix and finally,  $u_e$  is the unit vector toward nadir , [12], [13].

When  $\omega_0^2$  which is defined in Equation 3.29, is applied to Equation 3.28 with the unit vector toward nadir expressed in body frame,  $\tau_{grav}$  becomes,

$$\tau_{grav} = 3\omega_0^2 c_3^b \times (Ic_3^b) \quad , \quad \omega_0^2 = \frac{\mu}{R_o^3} \quad (3.29)$$

$c_3^b$  is the third column of the rotation matrix,  $R_o^b$ . It transforms the  $z_b$  axis to the  $z_o$  axis and defined in Equation 3.30.

$$c_3 = \begin{bmatrix} 2(\varepsilon_1 \varepsilon_3 - \eta \varepsilon_2) \\ 2(\varepsilon_2 \varepsilon_3 + \eta \varepsilon_1) \\ 1 - 2(\varepsilon_1^2 + \varepsilon_2^2) \end{bmatrix} \quad (3.30)$$

Then, Equation 3.29 becomes as [26], [8],

$$\tau_{grav}^b = 3\omega_o^2 \begin{bmatrix} 2(I_z - I_y)(\varepsilon_2\varepsilon_3 + \eta\varepsilon_1)(1 - 2(\varepsilon_1^2 + \varepsilon_2^2)) \\ 2(I_x - I_z)(\varepsilon_1\varepsilon_3 - \eta\varepsilon_2)(1 - 2(\varepsilon_1^2 + \varepsilon_2^2)) \\ 2(I_y - I_x)(\varepsilon_1\varepsilon_3 - \eta\varepsilon_2)(\varepsilon_2\varepsilon_3 + \eta\varepsilon_1) \end{bmatrix} \quad (3.31)$$

For the detailed deviation of the equations, see [8], [12], [13], [26].

### 3.6.1.2 Solar Radiation Pressure

The photons from the sun produces a force which results in a torque about the center of mass of the satellite. The solar radiation pressure has more effect on light objects with relatively high surface.

Mathematical model of the solar radiation pressure in most general form is given, [8],

$$d\vec{f}_{total} = -P \int \left[ (1 - C_a)S + 2(C_s \cos(\theta) + \frac{1}{3}C_d)\vec{N} \right] \cos(\theta)dA \quad (3.32)$$

Differential force vector can be modelled assuming that the incident radiation is either absorbed, reflected, or some combination of these. The coefficients  $C_a, C_s, C_d$  define the percentage of the absorbed, specularly reflected and diffusively reflected radiation, respectively.  $P$  is the mean momentum flux,  $\vec{S}$  is the unit vector from satellite to the Sun,  $\vec{N}$  is the unit vector along the normal of the exposed surface, and  $\theta$  is the angle between  $\vec{S}$  and  $\vec{N}$ . Solar radiation pressure is most effective at high altitudes. The surface area of the satellite which faces the Sun is taken into consideration to calculate the torque caused by solar radiation.

In Reference [7] , solar radiation is modelled as:

$$F_{SR} = -\rho_{SR} * c_R * A_{\ominus} * r_{\oplus\ominus} \quad (3.33)$$

where

$$\rho_{SR} = \frac{SF}{c} = \frac{1353 \frac{W}{m^2}}{3 * 10^8 \frac{m}{sec}} = 4.51 * 10^{-6} \frac{N}{m^2} \quad (3.34)$$

and where  $A_{\ominus}$  is the exposed area to the Sun. The reflectivity,  $c_R$ , shows how the satellite reflects incoming radiation, and its value is between 0.0 and 2.0.  $\rho_{SR}$  is solar radiation pressure.  $SF$  is the solar radiation constant,  $SF = 1353 \text{ W} / \text{m}^2$ , and  $c$  is the speed of the light,  $c = 3 \times 10^8 \text{ m} / \text{s}$ .

For the detailed derivation of the equations, see [8], [12], [13], [26].

### 3.6.1.3 Aerodynamic Drag

This disturbance is most effective on satellites orbiting below 400-500 km. The drag force created by the air molecule interaction with satellite body produce a torque on the satellite, thus reducing its velocity and resulting in a lower orbit for the satellite.

The torque is derived as:

$$\tau_{aero} = \frac{1}{2} \rho V^2 C_d A_{inc} (u_v \times (c_{pa} - c_g)), \quad F_{aero} = \frac{1}{2} \rho V^2 C_d A_{inc} \quad (3.35)$$

where  $\rho$  is the atmospheric density ( $\frac{kg}{m^3}$ ),  $A_{inc}$  is the area perpendicular to  $u_v (m^2)$ ,  $u_v$  is the unit vector in velocity direction,  $C_d$  is drag coefficient,  $V$  is velocity,  $c_{pa}$  center of pressure and finally,  $c_g$  is center of gravity. BILSAT-1 satellite is affected by the aerodynamic torque. The aerodynamic torque is added to the system in MATLAB-SIMULINK model when actuators are reaction wheels. On the other hand, aerodynamic torque is neglected in mathematical model of the satellite when magnetic torquers are actuators. The maximum torque delivered by

magnetic torquers is selected to be as  $0.1 \text{ Am}^2$  in simulations. This gives a good margin to counteract the total disturbing torques (only gravity gradient torque) effecting the satellite model environment. If desired and needed, one can add the aerodynamic torque to the mathematical model in case of magnetic torquers for more realistic applications. But it is worth to mention that maximum torque to overcome the effect of the disturbing torques shall be checked and increased by finding the magnitude of the total control torque required which is ideally expressed as:

$$|m^b| = \frac{|Total\ disturbing\ torques|}{|B^b|} \quad (3.35a)$$

In BILSAT-1 , the values given to parameters in Equation 3.35 are:

$\rho = 2.89 * 10^{-13}$  ,  $A_{inc} = 0.42 \text{ m}^2$  ,  $c_{pa} = c_{ga}$  ,  $V = \text{sqrt}[(2 * \frac{mu}{r^3}) - (\frac{mu}{a})]$  where  $mu = 3.986005 * 10^{15} \text{ km}^3/\text{s}^2$  ,  $r = (6378 + 686) \text{ km}$  ; distance of the satellite from the center of Earth,  $a = r$  for circular orbit and  $a$  represents semimajor axis.

For the detailed deviation of the equations, see [8], [12], [13], [26].

### 3.6.1.4 Magnetic Disturbance Torque

This torque is resulted from the interaction of the geomagnetic field and spacecraft's residual magnetic field. If  $\mathbf{M}$  is the sum of all magnetic moments in the satellite , the torque acting on the satellite [10], [16] :

$$\mathbf{T}^{(m)} = \mathbf{M} \times \mathbf{B} \quad (3.36)$$

where  $\mathbf{B}$  is the geomagnetic field vector.  $\mathbf{M}$  is caused by satellite generated current loops, permanent magnets or induced magnets.

In the following equation, torque produced by the magnetic torquers is defined.

$$\boldsymbol{\tau}_m^b = \mathbf{m}^b \times \mathbf{B}^b \quad (3.37)$$

where,  $\tau_m^b$  is the torque which is generated by the magnetic torquer,  $m^b$  is the magnetic dipole moment generated by the torquer,  $B^b = [B_x^b \ B_y^b \ B_z^b]^T$  is the local geomagnetic field vector, relative to the satellite. Local geomagnetic field vector can be found using some models such as IGRF or Dipole Model.

Magnetic dipole moment is given below :

$$m^b = m_x^b + m_y^b + m_z^b = \begin{bmatrix} N_x i_x A_x \\ N_y i_y A_y \\ N_z i_z A_z \end{bmatrix} = \begin{bmatrix} m_x \\ m_y \\ m_z \end{bmatrix} \quad (3.38)$$

where,  $N_k$  is number of windings in the torquer,  $A_k$  is the span area of the coil, and,  $i_k$  is the torquer current.

Magnetic torque can also be expressed as shown below, by the using skew-symmetric matrix formulation.

$$\tau_m^b = \mathbf{S}(m^b) \mathbf{B}^b = \begin{bmatrix} B_z^b m_y - B_y^b m_z \\ B_x^b m_z - B_z^b m_x \\ B_y^b m_x - B_x^b m_y \end{bmatrix} \quad (3.39)$$

For the detailed deviation of the equations, see [8], [12], [13], [26].

### 3.6.2 Reaction Wheel Torque

The reaction wheel configuration in x, y, z axes is generally modelled by the following equation, [23], [26]:

$$\tau_r^b = \left( \frac{dL_r}{dt} \right)^b + \omega_{bi}^b \times L_r - \tau_{friction}^b \quad (3.40)$$

$\tau_r^b$  is the torque caused by reaction wheel,  $L_r = [L_{rx} \quad L_{ry} \quad L_{rz}]^T = I_r \omega_r$  is the total moment vector of reaction wheel,  $\tau_{friction}^b$  is the frictional torque caused by wheels and usually assumed to be zero. Then Equation 3.40 turns out to be:

$$\tau_r^b = \left( \frac{dL_r}{dt} \right)^b + \omega_{bi}^b \times L_r = \begin{bmatrix} \tau_{rx} \\ \tau_{ry} \\ \tau_{rz} \end{bmatrix} = \begin{bmatrix} \dot{L}_{rx} + L_{rz} \omega_y - L_{ry} \omega_z \\ \dot{L}_{ry} + L_{rx} \omega_z - L_{rz} \omega_x \\ \dot{L}_{rz} + L_{ry} \omega_x - L_{rx} \omega_y \end{bmatrix} \quad (3.41)$$

$$\omega_{bi}^b = [\omega_x \quad \omega_y \quad \omega_z]^T \quad (3.42)$$

As stated before in Chapter II, reaction wheels can produce moment on the axis they are mounted on. Mounting reaction wheels at each of the three axis makes it possible to rotate the satellite according to the desired orientation. Challenge here lies on the development a robust, rapid and effective regulator. Reaction wheels are placed in tetrahedral configuration for extra robust regulation and for the reasons given in Chapter II and III. Figure 3.7 shows an example for the tetrahedral configured of the reaction wheels. In this work, as actuating torquers, the mathematical model given in Equation 3.43 is applied to the satellite model.

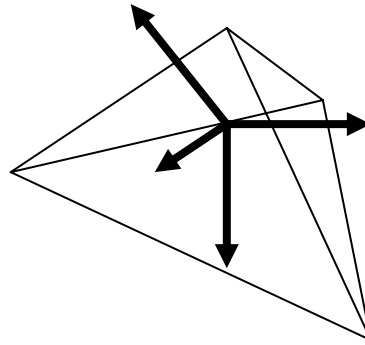


**Figure 3.7:** Example for the Tetrahedral Configured Reaction Wheels.

In some satellites, like BILSAT-1, there are three angles to be visualized; roll, pitch, yaw and there are four reaction wheels. Therefore, the parameter n is selected to be as three and the parameter r is selected as four. The contribution of the four wheels along three axes (x, y, z) can be expressed as, [23]:

$$T = \begin{bmatrix} t_1 & t_2 & t_3 & t_4 \end{bmatrix} = \begin{bmatrix} r_{1,x} & r_{2,x} & r_{3,x} & r_{4,x} \\ r_{1,y} & r_{2,y} & r_{3,y} & r_{4,y} \\ r_{1,z} & r_{2,z} & r_{3,z} & r_{4,z} \end{bmatrix} \quad (3.43)$$

where  $t_i = \begin{bmatrix} r_{i,x} & r_{i,y} & r_{i,z} \end{bmatrix}$  is the vector representing the location of each reaction wheel with the related axis.

The vectors in tetrahedral formation satisfy the following equations, [23] :

$$\begin{aligned} r_{1,x} + r_{2,x} + r_{3,x} + r_{4,x} &= 0 \\ r_{1,y} + r_{2,y} + r_{3,y} + r_{4,y} &= 0 \\ r_{1,z} + r_{2,z} + r_{3,z} + r_{4,z} &= 0 \end{aligned} \quad (3.44)$$

Equation (3.44) states that each reaction wheel in tetrahedral formation produces zero moment on each axis totally. Since then, each column vector shall be unit vector and satisfy the following equation.

$$\sqrt{(r_{i,x})^2 + (r_{i,y})^2 + (r_{i,z})^2} = 1 \quad i = 1,2,3,4 \quad (3.45)$$

The angle between the actuators in tetrahedral formation is given as  $109.47^\circ$ , [23] then  $\varphi = 2 \cos^{-1}(\frac{1}{\sqrt{3}})$ . Then the dot product between two vector,  $t_i$  and  $t_j$

becomes:

$$t_i t_j = |t_i| |t_j| \cos \varphi \quad (3.46)$$

where  $|t_i| = |t_j| = 1$  and  $\varphi$  is the angle between them. Combining Equations 3.44, 3.45 and 3.46 is enough to determine the tetrahedral formulation matrix. By placing  $t_1$  along z axis like  $t_1 = [0 \ 0 \ -1]$ , the remaining values in Equation 3.44 can be settled as  $r_{2,z} = r_{3,z} = r_{4,z} = \frac{1}{3}$ , then T becomes,

$$T = \begin{bmatrix} 0 & r_{2,x} & r_{3,x} & r_{4,x} \\ 0 & r_{2,y} & r_{3,y} & r_{4,y} \\ -1 & \frac{1}{3} & \frac{1}{3} & \frac{1}{3} \end{bmatrix} \quad (3.47)$$

All other vectors  $t_2, t_3, t_4$  form an angle of  $\varphi = 2 \cos^{-1}(\frac{1}{\sqrt{3}})$  with  $t_1$  by x and y components independently.

$$r_{1,x}r_{j,x} + r_{1,y}r_{j,y} + r_{1,z}r_{j,z} = \cos \varphi \quad j = 2,3,4 \quad (3.48)$$

$$r_{1,z}r_{j,z} = -\frac{1}{3} \quad (3.49)$$

$r_{2,x}$  is considered to be zero for finding  $t_2$ . When  $i=2$ ,  $r_{2,y}$  component will be as given below (from Equation 3.45):

$$\begin{aligned} \sqrt{(0)^2 + (r_{2,y})^2 + (\frac{1}{3})^2} &= 1 \\ r_{2,y} &= \pm \sqrt{1 - (\frac{1}{3})^2} \\ r_{2,y} &= \pm \frac{2}{3}\sqrt{2} \end{aligned} \quad (3.50)$$

One possible solution is,  $r_{2,y} = -\frac{2}{3}\sqrt{2}$ . According to Equation 3.44, the other parameters become as,  $r_{3,y} = r_{4,y} = \frac{1}{3}\sqrt{2}$ . Then, T becomes:

$$T = \begin{bmatrix} 0 & 0 & r_{3,x} & r_{4,x} \\ 0 & -\frac{2}{3}\sqrt{2} & \frac{1}{3}\sqrt{2} & \frac{1}{3}\sqrt{2} \\ -1 & \frac{1}{3} & \frac{1}{3} & \frac{1}{3} \end{bmatrix} \quad (3.51)$$

Vectors  $t_3$  and  $t_4$  form an angle of  $\varphi = 2\cos^{-1}\left(\frac{1}{\sqrt{3}}\right)$  with vector  $t_2$  independently by x component.

$$r_{2,x}r_{j,x} + r_{2,y}r_{j,y} + r_{2,z}r_{j,z} = \cos \varphi \quad j = 3,4 \quad (3.52)$$

$$r_{2,y}r_{j,y} + r_{2,z}r_{j,z} = -\frac{4}{9} + \frac{1}{9} = -\frac{1}{3} \quad (3.53)$$

Finally,  $r_{3,x}$  and  $r_{4,x}$  satisfies,

$$\begin{aligned} \sqrt{\left(\frac{1}{3}\sqrt{2}\right)^2 + (r_{i,x})^2 + \left(\frac{1}{3}\right)^2} &= 1 \\ r_{i,x} &= \pm\sqrt{-\left(\frac{1}{3}\sqrt{2}\right)^2 + 1 - \left(\frac{1}{3}\right)^2} \end{aligned} \quad (3.54)$$

Hence,  $r_{3,x} = +\frac{1}{3}\sqrt{6}$  and  $r_{4,x} = -\frac{1}{3}\sqrt{6}$ . Finally, T becomes:

$$T = \begin{bmatrix} 0 & 0 & \frac{1}{3}\sqrt{6} & -\frac{1}{3}\sqrt{6} \\ 0 & -\frac{2}{3}\sqrt{2} & \frac{1}{3}\sqrt{2} & \frac{1}{3}\sqrt{2} \\ -1 & \frac{1}{3} & \frac{1}{3} & \frac{1}{3} \end{bmatrix} \quad (3.55)$$

Tetrahedral configuration is used for the robust control and continuity of the control operation during failure in the any reaction wheel. For example, if any of the reaction wheels fails, remaining three still could supply the desired torque. Allocation matrix for the tetrahedral configuration can be found as given above. The torques produced by four wheels are converted to torques in three reference axes.

In fact, T stands for the tetrahedral configuration allocation matrix in the design scheme. Tetrahedral configuration of reaction wheels is usually preferred for the following reasons. First of all, four reaction wheeled structure provides an accurate control of the three axis in case of failure of one of the reaction wheels on any axis. The other advantage of this configuration comes from the geometry of the location of the angular momentum vectors. That's, it is possible to obtain twice as much as torque in one axis with this configuration. The vectoral addition of four reaction wheels according to one axis leads to this result. See Appendix A for more details.

Steering law is needed to distribute the momentum between the wheels during a maneuver. It realizes the torque commanded. There are several steering laws. The steering law applied in this thesis is given as below, [23]:

$$\tau = T(\alpha)Ku \quad ; \quad Ku = f \quad (3.56)$$

where  $u \in \mathfrak{R}^r$  and  $\alpha \in \mathfrak{R}^p$  and can be determined as given below:

$$\alpha = [\alpha_1 \quad , \quad \dots \quad \alpha_p]^T \quad , \quad u = [u_1 \quad , \quad \dots \quad u_r]^T \quad (3.57)$$

$K \in \mathfrak{R}^{r \times r}$  is a diagonal matrix as:

$$K = \text{diag}\{K_1, \dots, K_r\} \quad (3.58)$$

$T(\alpha)$  defines the actuator distribution along axes and defined as:

$$T(\alpha) = [t_1 \quad \dots \quad t_r] \quad (3.59)$$

Given the three dimensioned torque, one should find the four u term which correspond to four actuator inputs.

Let n be the number of axes angles (n=3) and r be the number of actuators (r=4). If  $r > n$ , system becomes overactuated and this problem can be solved by finding an optimal solution. That is problem becomes an LS optimization problem. In order to solve, minimization function should be applied as given in Equation 3.59, [23]:

$$J = \min\{f^T W f\} \quad (3.59)$$

With lagrange multiplier;

$$f = W^{-1} T^T (T W^{-1} T^T)^{-1} \tau \quad (3.60)$$

$$T_w^T = W^{-1} T^T (T W^{-1} T^T)^{-1} \quad (3.61)$$

where  $W$  is a diagonal positive definite matrix and can be taken to be equal to I. According to Moore-Penrose pseudo inverse law:

$$T^T = T^T (T T^T)^{-1} \quad (3.62)$$

Then, torque becomes as input u,

$$u = K^{-1}T_w^T \tau \quad (3.63)$$

Notice that, in simulation at MATLAB, u is defined as :

$$u = \text{alloc}(K, T, W, \tau) \quad (3.64)$$

The input torque, u, represents the model for tetrahedral configured reaction wheels' torque and is applied to the satellite dynamic equations in control model. Details of the equations and expressions given above can be found in Reference [23], [26]. Derivations for tetrahedral configuration (the angle between reaction wheels etc.) are given in Appendix A.

### 3.7 General Mathematical Modelling of a Satellite

In this part, general mathematical modelling of a satellite is expressed. Mathematical modelling concerns kinematic equations, dynamic equations and linearization of these equations. Dynamic equations describe how velocity changes for a given force. Kinematics differential equations express how position changes for a given velocity. For the detailed derivation of the equations, see [7], [8], [12], [13], [23], [26].

#### 3.7.1 Dynamic Model of a Satellite

Some assumptions are made for the dynamic modelling of the satellite. For example, satellite is assumed to act as a rigid body. Spacecraft is assumed to behave as a point mass model for orbital dynamics. According to Newton-Euler formulation angular momentum changes according to applied torque. With these assumptions, the dynamic model is given below [7], [26]:

$$I\dot{\omega}_{bi}^b + \omega_{bi}^b \times (I\omega_{bi}^b) = \tau^b \quad (3.65)$$

where,  $\tau^b = \tau_{grav}^b + \tau_m^b$  when magnetic torquers are selected as actuators for stabilization mode, or  $\tau^b = \tau_{grav}^b + \tau_{aero} + \tau_{reac}$  when reaction wheels act as actuators in maneuver control,  $I$  is the moment of inertia,  $\omega_{bi}^b$  is the angular velocity of the body frame with respect to the inertial frame in the body frame,  $\tau^b$  are the torques acting on the satellite in body frame,  $\tau_{grav}^b$  is the gravitational torque on the satellite body,  $\tau_m^b$  is the torque applied by the magnetic torquer,  $\tau_{reac}$  is the reaction wheel torque and  $\tau_{aero}$ , is the aerodynamic torque. Total torque changes according to the selection of actuator. In this section, related equations and linearizations are given for both cases, either magnetic torquer or reaction wheel selected as actuator.

Using the skew-symmetric operator, Equation (3.65) turns out to be :

$$I\dot{\omega}_{bi}^b + S(\omega_{bi}^b)I\omega_{bi}^b = \tau^b \quad (3.66)$$

To add angular velocity vectors as given in Equation 3.67, transformation of all velocity vectors to the same reference frame shall be done. Rotation matrix is applied to the below equation in order to carry all vectors to the same reference frame. Body frame is usually used as reference frame in attitude dynamics. The rotation matrix that changes angular velocity in orbit frame to body frame is given in Equation 3.16 [7], [26].

$\omega_{bi}^b$ , the angular velocity of the satellite, can also be expressed as, [26],

$$\omega_{bi}^b = \omega_{bo}^b + \omega_{oi}^b = R_o^b \omega_{oi}^o + \omega_{bo}^b \quad (3.67)$$

where,  $\omega_{oi}^o = [0 \quad -\omega_o \quad 0]$  is the angular velocity of the orbit frame relative to the ECI frame, expressed in Orbit frame. Then  $\omega_{bi}^b$  becomes,

$$\omega_{bi}^b = \begin{bmatrix} \omega_x \\ \omega_y \\ \omega_z \end{bmatrix} = \omega_{bo}^b - \omega_o c_2 \quad (3.68)$$

where  $c_2$  is the second column of the rotation matrix given in Equation 3.16.

Detailed expressions and derivations for the equations given in this section can be found in Reference [26].

### 3.7.2 Kinematics for Satellite Model

Kinematics of the satellite describes the orientation of the satellite. Kinematics is simply integration of the angular velocity. The differential equations are given below and detailed information about them can be found in References [12], [22] and [26] in detail.

$$\dot{\eta} = -\frac{1}{2} \varepsilon^T \omega_{bo}^b \quad (3.69)$$

$$\dot{\varepsilon} = \frac{1}{2} \eta \omega_{bo}^b - \frac{1}{2} \omega_{bo}^b \times \varepsilon \quad (3.70)$$

When Equations 3.69 and 3.70 are combined, they can be represented as in Equation 3.71:

$$\dot{q} = \begin{bmatrix} \dot{\eta} \\ \dot{\varepsilon} \end{bmatrix} = \frac{1}{2} \begin{bmatrix} -\varepsilon^T \\ \eta I_{3 \times 3} + S(\varepsilon) \end{bmatrix} \omega_{bo}^b \quad (3.71)$$

Angular velocity in the body frame relative to the orbit frame is expressed as:

$$\omega_{bo}^b = \omega_{bi}^b - R_o^b \omega_{oi}^o = \omega_{bi}^b + \omega_o c_2 \quad (3.72)$$

The details of the equations given above can be found in Reference [26].

### 3.8 Linearization of Mathematical Model

When linear controller techniques are selected for the attitude control system, the system mathematical model should be linearized. The linearization points are selected as given in Equation 3.73,

$$q = \begin{bmatrix} 1 \\ 0 \end{bmatrix} \quad (3.73)$$

The idea in selection is to coincide the body frame with the orbit frame for three-axis stability. The nadir vector of the satellite points to the center of the Earth.

In the following sections, linearized equations for the mathematical model are obtained. Details of the derivations can be found in Reference [26], [7], [23] and Appendix A.

#### 3.8.1 Linearization of Kinematic Equations

In Equation 3.74, kinematic model of the satellite is given as [7], [23], [21], [26]:

$$\dot{q} = \begin{bmatrix} \dot{\eta} \\ \dot{\varepsilon} \end{bmatrix} = \frac{1}{2} \begin{bmatrix} -\varepsilon^T \\ \eta I_{3 \times 3} + S(\varepsilon) \end{bmatrix} \omega_{bo}^b \quad (3.74)$$

System is linearized about the points where  $\eta = 1$  and  $\varepsilon = 0$ . Applying these linearization points to Equation 3.74, the following equation is obtained [7], [23], [21], [26]:

$$\dot{q} = \begin{bmatrix} \dot{\eta} \\ \dot{\varepsilon} \end{bmatrix} = \frac{1}{2} \begin{bmatrix} 0 \\ \omega_{bo}^b \end{bmatrix} \quad (3.75)$$

It is easy to see from Equation 3.75 that  $\omega_{bo}^b = 2\dot{\varepsilon}$ .

### 3.8.2 Rotation Matrix Linearization

If the rotation matrix between body and orbit frame given in Equation 3.16 is linearized around points given as  $\eta = 1$  and  $\varepsilon = 0$ , it becomes,

$$R_o^b = 2 \begin{bmatrix} \frac{1}{2} & \varepsilon_3 & -\varepsilon_2 \\ -\varepsilon_3 & \frac{1}{2} & \varepsilon_1 \\ \varepsilon_2 & -\varepsilon_1 & \frac{1}{2} \end{bmatrix} \quad (3.76)$$

### 3.8.3 Angular Velocity Linearization

By applying Equation 3.76 and  $\omega_{bo}^b = 2\dot{\varepsilon}$  into 3.67, linearized model of  $\omega_{bi}^b$  is derived as:

$$\omega_{bi}^b = \begin{bmatrix} \omega_x \\ \omega_y \\ \omega_z \end{bmatrix} = \begin{bmatrix} 2\dot{\varepsilon}_1 - 2\omega_o\varepsilon_3 \\ 2\dot{\varepsilon}_2 - \omega_o \\ 2\dot{\varepsilon}_3 + 2\omega_o\varepsilon_1 \end{bmatrix} \quad (3.77)$$

The time derivative of  $\omega_{bi}^b$  is hence obtained as:

$$\dot{\omega}_{bi}^b = \begin{bmatrix} \dot{\omega}_x \\ \dot{\omega}_y \\ \dot{\omega}_z \end{bmatrix} = \begin{bmatrix} 2\ddot{\varepsilon}_1 - 2\omega_o\dot{\varepsilon}_3 \\ 2\ddot{\varepsilon}_2 \\ 2\ddot{\varepsilon}_3 + 2\omega_o\dot{\varepsilon}_1 \end{bmatrix} \quad (3.78)$$

Equations 3.77 and 3.78 will then be used to derive the linearized dynamic equation.

### 3.8.4 Linearization of the Gravitational Torque

$\tau_{grav}^b$  in Equation 3.31 is simplified as in Equation 3.79, when  $\eta = 1$  and  $\varepsilon = 0$ :

$$\tau_{grav}^b = 3\omega_o^2 \begin{bmatrix} 2(I_z - I_y)\varepsilon_1 \\ 2(I_x - I_z)\varepsilon_2 \\ 0 \end{bmatrix} \quad (3.79)$$

### 3.8.5 Magnetic Torquer Linearization

The torque from magnetic torquer is given as [26], [7]:

$$\tau_m^b = S(m^b)B^b = S(m^b)R_b^o B^o = S(m^b)[I_{3 \times 3} - 2\eta S(\varepsilon) + 2S^2(\varepsilon)]B^o \quad (3.80)$$

Linearizing it around  $\eta = 1$  and  $\varepsilon = 0$  gives:

$$\tau_m^b = S(m^b)B^o = \begin{bmatrix} B_z^o m_y - B_y^o m_z \\ B_x^o m_z - B_z^o m_x \\ B_y^o m_x - B_x^o m_y \end{bmatrix} \quad (3.81)$$

### 3.8.6 Linearization of the Reaction Wheel Torque

Reaction wheels dynamic equations, which are shown below, is linearized around the point where  $\omega_{bi}^b = 0$ ,

$$\tau_r^b = \left(\frac{dL_r}{dt}\right)^b + \omega_{bi}^b \times L_r = \begin{bmatrix} \tau_{rx} \\ \tau_{ry} \\ \tau_{ry} \end{bmatrix} = \begin{bmatrix} \dot{L}_{rx} + L_{rz} \omega_y - L_{ry} \omega_z \\ \dot{L}_{ry} + L_{rx} \omega_z - L_{rz} \omega_y \\ \dot{L}_{rz} + L_{ry} \omega_x - L_{rx} \omega_y \end{bmatrix} \quad (3.82)$$

The result comes out to be:

$$\tau_r^b = \left(\frac{dL_r}{dt}\right)^b = \begin{bmatrix} \dot{L}_{rx} \\ \dot{L}_{ry} \\ \dot{L}_{rz} \end{bmatrix} \quad (3.83)$$

### 3.8.7 Linearization of the Satellite Mathematical Model with Magnetic Torquer as Actuator

Mathematical model of the satellite can also be obtained as,

$$I\dot{\omega}_{bi}^b = -\omega_{bi}^b \times (I\omega_{bi}^i) + S(m^b B^o) + \tau_{grav}^b \quad (3.84)$$

The time derivative of the Equation 3.84, can be modelled with quaternion parameters by the help of the derivations given in Appendix A. Then, the system can be represented by state-space representation in linear form given by Equation 3.85.

$$\dot{x}(t) = Ax(t) + B(t)u(t) \quad (3.85)$$

Now, if we define the states to be  $x = [\varepsilon_1 \quad \dot{\varepsilon}_1 \quad \varepsilon_2 \quad \dot{\varepsilon}_2 \quad \varepsilon_3 \quad \dot{\varepsilon}_3]$  and inputs to be  $u = [m_x \quad m_y \quad m_z]^T$ , then, A matrix can be written as in Equation 3.86 and B matrix can be written as in Equation 3.87.

$$A = \begin{bmatrix} 0 & 1 & 0 & 0 & 0 & 0 \\ -4k_x \omega_o^2 & 0 & 0 & 0 & 0 & (1-k_x)\omega_o \\ 0 & 0 & 0 & 1 & 0 & 0 \\ 0 & 0 & -3k_y \omega_o^2 & 0 & 0 & 0 \\ 0 & 0 & 0 & 0 & 0 & 1 \\ 0 & -(1-k_z)\omega_o & 0 & 0 & -k_z \omega_o^2 & 0 \end{bmatrix} \quad (3.86)$$

and

$$B(t) = \begin{bmatrix} 0 & 0 & 0 \\ 0 & \frac{1}{2I_x} B_z^o & -\frac{1}{2I_x} B_y^o \\ 0 & 0 & 0 \\ -\frac{1}{2I_y} B_z^o & 0 & \frac{1}{2I_y} B_x^o \\ 0 & 0 & 0 \\ \frac{1}{2I_x} B_y^o & -\frac{1}{2I_x} B_x^o & 0 \end{bmatrix} \quad (3.87)$$

### 3.8.8 Linearization of the Satellite Mathematical Model with Reaction Wheel as Actuator

Assuming that the applied torque to be coming from reaction wheels, dynamic equation becomes:

$$I\dot{\omega}_{bi}^b = -\omega_{bi}^b \times (I\omega_{bi}^b) + \tau_{grav}^b + \left(\frac{dL}{dt}\right)^b \quad (3.88)$$

Repeating the steps as done in previous section, the mathematical model of the linearized system becomes:

$$\dot{x}(t) = Ax(t) + B(t)u(t) \quad (3.89)$$

where  $u = [\dot{L}_{rx} \quad \dot{L}_{ry} \quad \dot{L}_{rz}]^T$  in this model.,

The derivation of the state-space representation is given in Appendix A in detail. By the help of those derivations, A matrix is found to be:

$$A = \begin{bmatrix} 0 & 1 & 0 & 0 & 0 & 0 \\ -4k_x\omega_o^2 & 0 & 0 & 0 & 0 & (1-k_x)\omega_o \\ 0 & 0 & 0 & 1 & 0 & 0 \\ 0 & 0 & -3k_y\omega_o^2 & 0 & 0 & 0 \\ 0 & 0 & 0 & 0 & 0 & 1 \\ 0 & -(1-k_z)\omega_o & 0 & 0 & -k_z\omega_o^2 & 0 \end{bmatrix} \quad (3.90)$$

and B matrix becomes:

$$B(t) = \begin{bmatrix} 0 & 0 & 0 \\ \frac{1}{2I_x} & 0 & 0 \\ 0 & 0 & 0 \\ 0 & \frac{1}{2I_y} & 0 \\ 0 & 0 & 0 \\ 0 & 0 & \frac{1}{2I_z} \end{bmatrix} \quad (3.91)$$

### 3.9 Some Linear Control Techniques Applied for Attitude Control

#### 3.9.1 Attitude Control

Wertz [8] defines attitude control, attitude maneuver and attitude stabilization processes as stated below:

*Attitude control is the process of achieving and maintaining an orientation in space. An attitude maneuver is the process of reorienting the spacecraft from one attitude to another. Attitude stabilization is the process of maintaining an existing attitude relative to some external relative frame.*

Attitude control system is both the hardware and the software by which spacecraft's attitude is controlled. Attitude control system components are: attitude sensors which locate known reference targets such as Earth, Sun to determine the attitude; control process that determines when control is required and lastly, control hardware which is the mechanism that supplies the control torque.

Because of the existence of disturbance torques throughout the spacecraft environment, some procedure is necessary for attitude control and stabilization. Spacecraft stabilization techniques can be listed as:

1. Spacecraft stabilization by the spacecraft's angular momentum (spin stabilized) .
2. Spacecraft stabilization by its response to environmental torques, e.g. gravity gradient stabilization.
3. Spacecraft stabilization by active control with reaction wheels, gas jets or electromagnets.

In general, active methods of control are more accurate, faster and flexible than passive control systems but they consume more power.

In spin stabilization control technique, the entire spacecraft is rotated so that its angular momentum remains fixed in inertial space. A gravity-gradient stabilization system interacts with the gravitational torque to maintain the spacecraft attitude. The basic requirement for gravity-gradient stabilization is that the gravity-gradient torque must be larger than all other environmental torques. Because of that reason, it is usually preferred in near Earth or Moon satellites as a control technique (e.g. Radio Astronomy Explorer-2 satellite).

Mass expulsion control systems being an active control method, are generally used for attitude maneuvering including gas jets and thrusters. They are simple to operate but expensive and sometimes cause orbit changes during maneuvering action. They are commonly used in spin-stabilized spacecrafts. For three-axis stabilization, minimum six thrusters are needed to maneuver in all directions. Momentum wheel control systems can have one or more wheels on axes and require a secondary control system, to maintain the wheel and the spacecraft momentum in presence of disturbance torques and friction losses. Magnetic coil control system in active control, can be used for maneuvers for virtually all orbits less than synchronous altitudes below 35,000 km.

### **3.9.2 Some Linear Control Techniques**

Attitude control techniques can be divided into two categories, attitude stabilization and, attitude maneuver. Attitude stabilization consists of maintaining an existing orientation. Attitude maneuver control consists of reorienting the spacecraft from one attitude to another. In this section, several linear control techniques are investigated referring to both categories. Linear controller is applied to attitude maneuvering control with reaction wheels as actuators. Linear quadratic regulator is applied as controller for attitude stabilization with magnetic torquer as actuator.

#### **3.9.2.1 Controllability**

The linearized system has a model given by:

$$\begin{aligned}\dot{x} &= Ax + Bu \\ y &= Cx\end{aligned}\tag{3.92}$$

Controllability property is the property to be able to find  $u$  such that the states are forced to go from initial state,  $x_0$ , to final desired state,  $x_f$ , in finite time. By applying the

definition given below (Balchen, Andresen and Foss, 2001), verification of this property can be checked.

**Definition 3.1.** The system states in Equation 3.93 are completely controllable if and only if the rank of  $Q_c = n$ , where  $n$  is the dimension of  $x$ , and  $Q_c$  is given by:

$$Q_c = [B, AB, A^2B, \dots, A^{n-1}B] \quad (3.93)$$

The controllability of the designed system is checked by using Matlab controllability function named as `ctrlb( )`. Rank of the controllability matrix  $Q_c$ , is equal to the dimension of states in this thesis. That means all states are controllable.

### 3.9.2.2 Linear Controller

In fact, linear controller is simply a P controller. In order to find a state feedback value, pole placement technique is applied to the plant. The closed-loop pole locations have a direct effect on time response characteristics such as settling time, rise time and transient oscillations. Pole placement is a state-space design technique used to assign closed-loop poles in Multiple-Input Multiple-Output (MIMO) systems. This technique requires a state-space model of the system as given in Equation 3.95. The torque vector,  $u(t)$  is the input that controls the system.

$$\begin{aligned} \dot{x}(t) &= Ax(t) + Bu(t) \\ y(t) &= Cx(t) \end{aligned} \quad (3.94)$$

In Equation 3.94, the values of A and B matrices are obtained after linearization process which is explained in Section 3.8.8. The state feedback gain, K, is applied to the system such that the control input becomes  $u=K(r-x)$  where,  $r$  is the desired state vector, usually known as reference, and  $x$  is the actual state vector.

As a result, Equation 3.95 turns out to be:

$$\dot{x}(t) = Ax(t) + Bu(t) = Ax(t) + BK(r(t) - x(t)) = (A - BK)x(t) + BKr(t) \quad (3.95)$$

where  $x = [\varepsilon_1 \quad \dot{\varepsilon}_1 \quad \varepsilon_2 \quad \dot{\varepsilon}_2 \quad \varepsilon_3 \quad \dot{\varepsilon}_3]$  represents the state vector and the control input is defined as  $u = K(r - x)$ .

$K$ , state feedback matrix, is found by pole placement technique, with Matlab code *place* as shown below:

$$K = \text{place}(A, B, p) \quad (3.96)$$

*Place* computes a gain matrix  $K$  such that the state feedback  $u = -K(r - x)$  places the closed-loop poles at the locations of desired self-conjugate closed-loop pole locations,  $p$ . That is, the eigenvalues of  $A - BK$  match the entries of  $p$ . In order to use this algorithm, all states should be controllable. In other words,  $(A, B)$  pair must be controllable.

Vector of complex conjugate pole pairs,  $p$ , is selected after several trials as given below.

$$p = \begin{bmatrix} -0.1 + 0.1j \\ -0.1 - 0.1j \\ -0.1 + 0.1j \\ -0.1 - 0.1j \\ -0.1 + 0.1j \\ -0.1 - 0.1j \end{bmatrix} \quad (3.97)$$

The length of  $p$  must match the row size of  $A$ . In high-order systems, choosing pole locations in an unrealistic way results in high gain values. This makes the entire closed-loop eigenstructure very sensitive to perturbations.

### 3.9.2.3 Linear Quadratic Regulator

In this thesis, Linear Quadratic Regulator (LQR) is a control technique used in attitude stabilization. The main idea of the control system is to find a cost function and minimize this cost function. First of all, system dynamics is linearized around the selected points. The cost function is minimized, and lastly, system states are fed back by a gainmatrix. In References [19], [21], [23], LQR technique is explained in detail.

Since minimizing a cost function is the main aim of the control idea, we need a cost function as defined below, [7]:

$$J(u) = \frac{1}{2} \int_{t_0}^T [\tilde{x}^T Q \tilde{x} + u^T P u] dt \quad (3.98)$$

where

$$\tilde{x}(t) = x(t) - x_d(t) \quad (3.99)$$

and  $x_d(t)$  is the reference trajectory (desired),  $\tilde{x}(t)$  is then the error between actual and desired states,  $Q$  is the positive semidefinite weight matrix for the state deviation and  $P$  is the positive definite weight matrix for the actuator. In order to solve this though cost function, Ricatti equation is applied. Below Ricatti equation is given:

$$\dot{R}(t) = -R(t)A - A^T R(t) + R(t)B(t)P^{-1}B(t)^T R(t) - Q(t) \quad (3.100)$$

Finally, the solution of the LQ-problem results in :

$$u(t) = -P^{-1}B(t)^T R(t)x(t) \quad (3.101)$$

The mean value of  $B^o$  in  $B(t)$  is applied to the equation as geomagnetic field is assumed to be periodic. This results in a time invariant model,

$$\dot{x} = Ax + Bu \quad (3.102)$$

which in turn implies the following algebraic Ricatti Equation:

$$0 = -RA + A^T R - RBP^{-1}B^T R + Q \quad (3.103)$$

The control input then turns out to be :

$$u(t) = -P^{-1}B^T Qx(t) \quad (3.104)$$

Now, let us mention some properties of Q and P. Weight matrices are defined as:

$$Q = \text{diag}[q_1 \quad , \quad q_2 \quad , \quad \dots \quad q_{n_s}]$$

$$P = \text{diag}[p_1 \quad , \quad p_2 \quad , \quad \dots \quad p_{n_a}] \quad (3.105)$$

where  $n_s$  is the number of the states and  $n_a$  is the number of actuators.

According to Kristiansen, [19], weight matrices can be taken as;

$$p_i = \frac{1}{(\Delta u_i)^2} \quad \text{and} \quad q_i = \frac{1}{(\Delta x_i)^2} \quad (3.106)$$

where  $\Delta u_i$  is the  $i$  th maximum dipole moment of the actuator and  $\Delta x_i$  is the state deviation.

In LQR control, Matlab code, *lqr* is applied to the design as given below:

$$[K, S, E] = lqr(A, B, Q, P) \quad (3.107)$$

$lqr(A, B, Q, P)$  calculates the optimal gain matrix  $K$  such that the state-feedback law,  $u = -Kx$ , minimizes the quadratic cost function in Equation 3.107 for the state-space model.  $T$  is taken as the simulation time and  $t_0$  is taken as zero in Equation 3.98.

$lqr$  also returns the solution  $S$  of the Riccati equation given in Equation 3.107 and the closed-loop eigenvalues  $E = eig(A - B * K)$ .

### 3.10 Summary

Throughout this chapter, mathematical definitions and equations concerning satellite dynamics are expressed briefly. After this analysis, linear control techniques applied in control scheme are explained. Chapter IV gives the simulation results of these control techniques.

## CHAPTER IV

### SIMULATION RESULTS

This chapter includes different linear controllers studied throughout this thesis and the behavior of the system when these controllers are applied to the satellite model.

In this work, two different modes of the satellite are examined with two different actuators. These modes are attitude stabilization and attitude maneuver. In attitude stabilization, magnetic torquers are used as actuators and linear quadratic regulator is selected as the control method. On the other hand, actuators of the attitude maneuver mode are reaction wheels with linear regulator as applied control method. Following sections, briefly describes the satellite model used in simulations and gives simulation results of the applied controllers.

Controllers are simulated in MATLAB/SIMULINK environment. Simulations time scale is given in orbit unit. One orbit unit is equal to 96.6 minutes. This time period is nearly equal to the actual period of the BILSAT-1. BILSAT-1 actual satellite properties are given in Table 4.1.

**Table 4.1:** BILSAT-1 Satellite Properties

<b>BILSAT-1 SATELLITE PROPERTIES</b>	<b>VALUE</b>
<b>Weight</b>	120 Kg.
<b>Inertia Matrix</b>	$I_x = 9.8194, I_y = 9.7030, I_z = 9.7309 \text{ kgm}^2$
<b>Orbit</b>	686 km 10:30 AM-10:30 PM Sun Sync. Low Earth Orbit.
<b>Orbit Period</b>	97.7 Min.

## 4.1 Satellite Model with Magnetic Torquers as Actuators

The basic block diagram of the Simulink model of the satellite is given below:

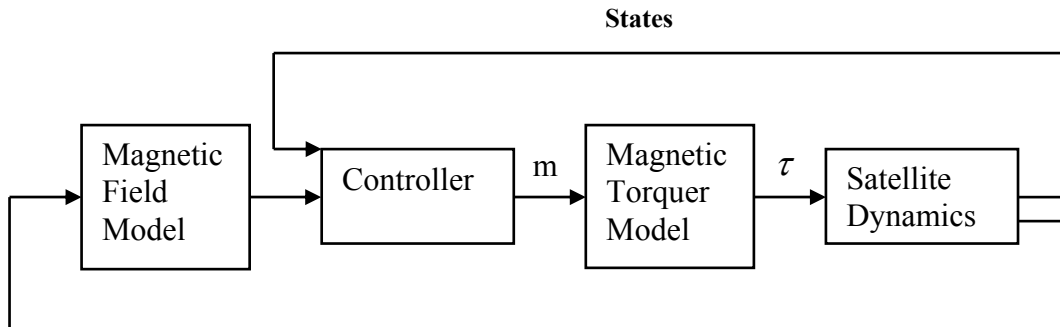


**Figure 4.1:** Generalized Satellite Model with Magnetic Torquers.

In this model, magnetic field model calculates the magnetic field,  $B$  of Earth. Controller is selected as linear quadratic regulator and it is explained in Chapter III in detail. The output of the controller is the magnetic moment of the torquer. The torque obtained from magnetic torquer model is used in satellite dynamics. Chapter III also contains the mathematical derivations for the model given above. The aim of the controller is to stabilize the system about the given equilibrium points in order to simulate the attitude stabilization mode in real applications. The small angle changes around the equilibrium point is compensated with the help of this design.

## 4.2 Satellite Model with Reaction Wheels as Actuators

The basic block diagram of the Simulink model of the satellite is given in Figure 4.2:

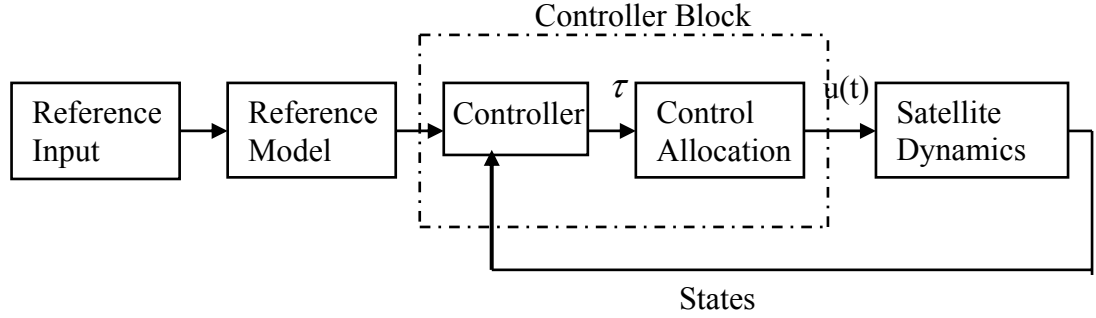


**Figure 4.2 :** Generalized Satellite Model with Reaction Wheels.

Reference input block gives the desired Euler angles that are set for the attitude maneuver mode. Reference model takes quaternion form of the reference Euler angles as input. The main aim of the reference model is to generate a smooth reference trajectory for the controller to follow. It is simply a filter that corrects fluctuations of the input in such a way that output trajectory becomes a smooth curve. Reference model used in the Simulink model of the satellite is taken from Reference [23]. A similar model is also used in Reference [21].

The transfer function of the model is given as:

$$\frac{q_{di}}{q_{ri}} = \frac{\omega_n^3}{(s + \omega_n)(s^2 + 2\zeta\omega_n + \omega_n^2)} \quad i \in \{1, \dots, 4\} \quad (4.1)$$

where  $q_{di}$  is the desired ,smooth output reference vector,  $q_{ri}$  is the reference input of the system from the reference input block,  $\zeta$  is the relative damping factor and finally,  $\omega_n$  is the resonance frequency of the system.  $\zeta$  is set to 1 in order to obtain critical damping response,  $\omega_n$  is selected as 0.002 rad/sec. after several values between 0 and 1 are tried (e.g.  $\omega_n=0.5$ ,  $\omega_n=0.035$ ,  $\omega_n=0.35$ ).

Control allocation block distributes the torques belonging to reaction wheels, which is (3x4) matrix, on to the input torque matrix, which is (1x3) matrix, and sends it to the satellite dynamics as input. The distribution matrix which is denoted by  $T$ , was widely explained in Chapter III.

$$T = \begin{bmatrix} t_1 & t_2 & t_3 & t_4 \end{bmatrix} = \begin{bmatrix} r_{1,x} & r_{2,x} & r_{3,x} & r_{4,x} \\ r_{1,y} & r_{2,y} & r_{3,y} & r_{4,y} \\ r_{1,z} & r_{2,z} & r_{3,z} & r_{4,z} \end{bmatrix} \quad (4.2)$$

where  $t_i = \begin{bmatrix} r_{i,x} & r_{i,y} & r_{i,z} \end{bmatrix}$  is the vector representing the location of each actuator with the related axis.

The (1x3) controller output torque vector is distributed on to the reaction wheels by using  $T$  matrix and (1x4) input vector,  $u(t)$ , is obtained. This is obtained by the Alloc command in the Matlab GNC Toolbox, which is written by Fossen, 2002 [16].

### 4.3 Simulation Results with Reaction Wheels as Actuators

#### 4.3.1 Linear Controller

Control input in linear regulator controller is defined as:

$$u = K(r-x) \quad (4.3)$$

where,  $r$  is the desired state vector, usually known as reference, and  $x$  is the actual state vector.

Initial conditions and controller parameters used in the simulations are given in Table 4.2.

**Table 4.2:** Initial Values of the Parameters

PARAMETERS	INITIAL VALUE
Angular Velocity	$\omega_{0b}^b = [0 \ 0 \ 0]^T$
Euler Angles $[\phi \ \theta \ \psi]$	$[0 \ 0 \ 0]$
Desired Euler Angles $[\phi \ \theta \ \psi]$	$[20 \ 40 \ 60]$
Aerodynamic Torque	3.4245e-07
$\omega_n$	0.02
$\zeta$	1
Pole p1, p3, p5	-0.1 + 0.1i
Pole p2, p4, p6	-0.1 - 0.1i

The values of BILSAT-1 inertia matrix is given as;  $I_{xx} = 9.8194$ ,  $I_{xy} = 0.0721$ ,  $I_{xz} = 0.2893$ ,  $I_{yx} = 0.0721$ ,  $I_{yy} = 9.7030$ ,  $I_{yz} = 0.1011$ ,  $I_{zx} = 0.2892$ ,  $I_{zy} = 0.1011$ ,  $I_{zz} = 9.7309$ . Diagonal values  $I_{xx}$ ,  $I_{yy}$ ,  $I_{zz}$  are used as the diagonal elements of I.

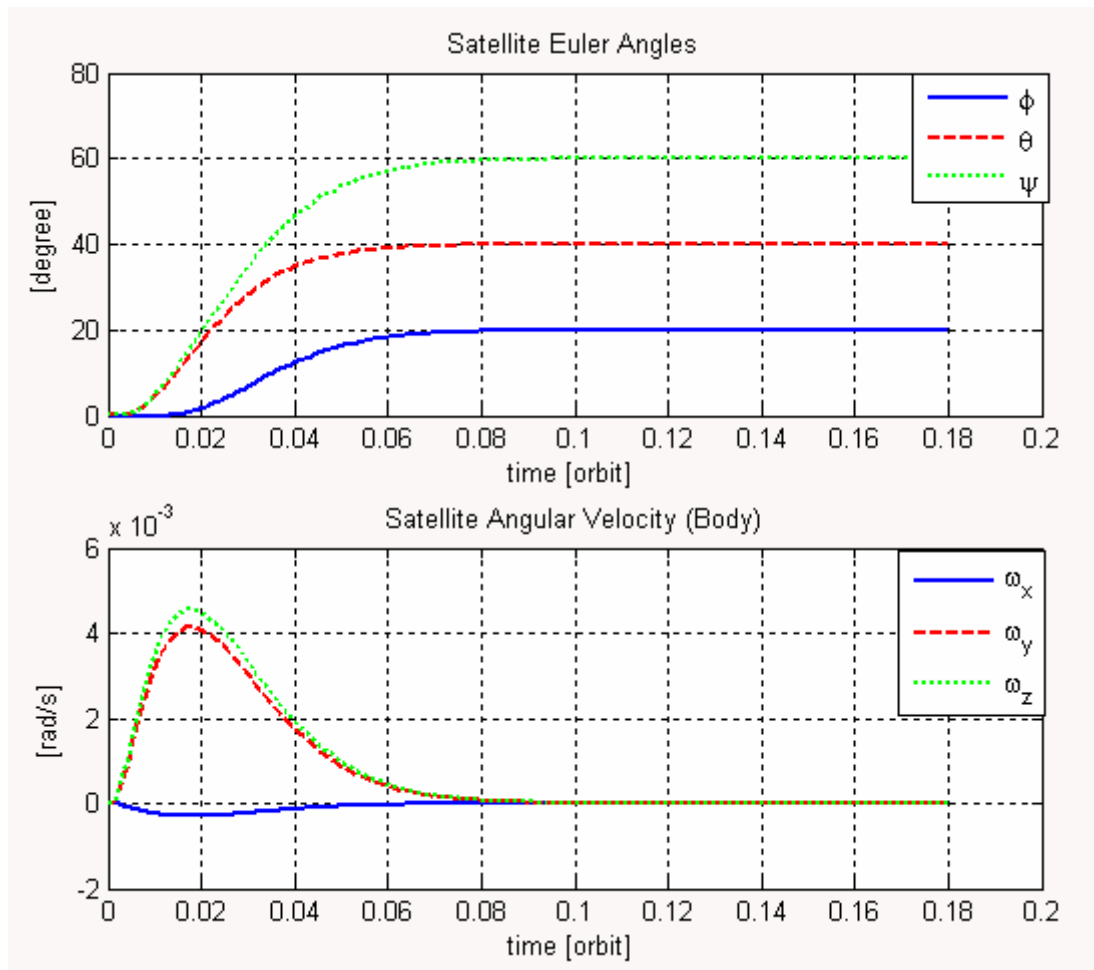
K gain matrix is calculated by place command:

$$K = \text{place}(A, B, p) \quad (4.4)$$

where A and B are found from state-space equations.

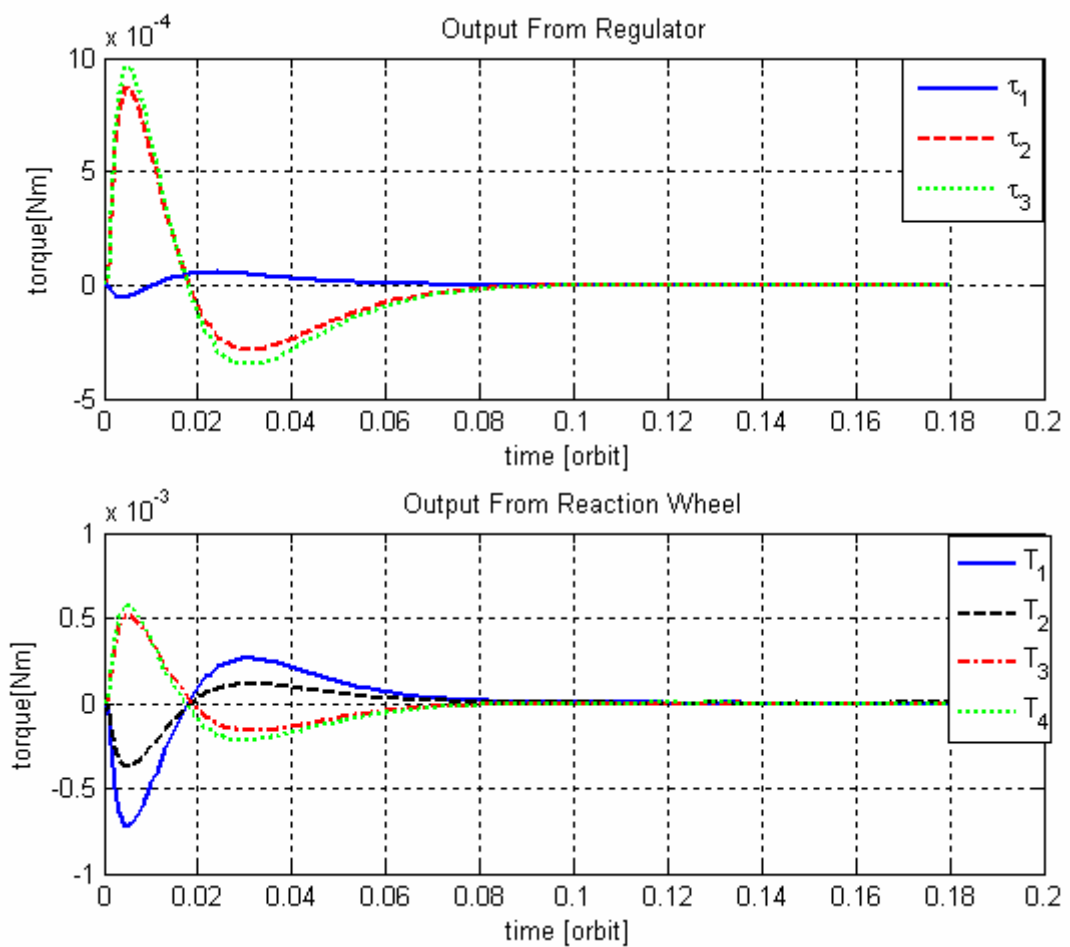
Simulations are observed for several cases. Case 1 stands for the simulation with aerodynamic disturbance torque effect and without noise effect. The effect of noise is given in Case 2. In Case 3, one of the reaction wheels are disabled in order to show the effect of tetrahedral configuration of the reaction wheels. Case 4 represents the output response of the system when two wheels are disabled. Finally, Case 5 shows a maneuver in pitch direction.

Figure 4.3 and 4.4 shows the simulation results of the linear regulator control method with aerodynamic torque effect and without noise effect.



**Figure 4.3:** Satellite Euler Angles and Angular Velocity in Body Frame.

The top view graph in Figure 4.3 shows that Euler angles reach the selected desired values at about 0.08 orbits. The system has a long rise time and settling time. If desired, this long rise time and settling time can be changed by adjusting the values of  $\omega_n$  (i.e.  $\omega_n=0.5$  ). But applying these values results in increase at the torque values of reaction wheels which is not desirable in real-life applications. The greater torque value needed is, the greater power rating of actuators needed will be. Steady state error for the system is minimized by using the reference model as input. The bottom view graph in Figure 4.3 shows the angular velocity trajectory of the system.



**Figure 4.4:** Outputs of the Reaction Wheels and Regulator.

The top view graph of the Figure 4.4 represents the output from the regulator, which is calculated by  $-K(x-x_d)$ . The trajectory nearly reaches to the value of zero after 0.08 orbits as expected. This proves that the error of the states reaches to zero. The bottom graph in Figure 4.4 stands for the output from the reaction wheels. The wheels never exceed the maximum torque value given as 1 mNm in Matlab program. The trajectory for the wheels changes from negative to positive torque values or vice versa after 0.02 orbits. This is because of the interaction between the output of the regulator, the output of the reaction wheels and K gain matrix.

Figure 4.5 and 4.6 are the results of the Case 2 described below. Uniformly

distributed noise which is a replica of the internal noise resulting from reaction wheels, is added to the actuator torque by  $\tau = \tau + r_{b_o} * (\text{noise})$  formulation. The expression in Matlab codes for uniformly distributed noise modelling,  $\text{sign}((2 * \text{rand}(1) - 1))$ , ensures that the noise is either in the region of  $-1$  or  $1$  of the actuator torque because  $\text{rand}(1)$  gives numbers in the region of  $[0.0 \ 1.0]$ . In this work, the expression given above is multiplied with the 40 percent of the produced torque to model a realistic internal noise. It is important to mention that different noise models can be applied to the satellite model for different actuators. Different noise models can be selected by analyzing the internal noise produced by the actuators (datasheets, etc.). For example, white gaussian noise model can be used in order to model the internal noise resulted from gyroscopes.

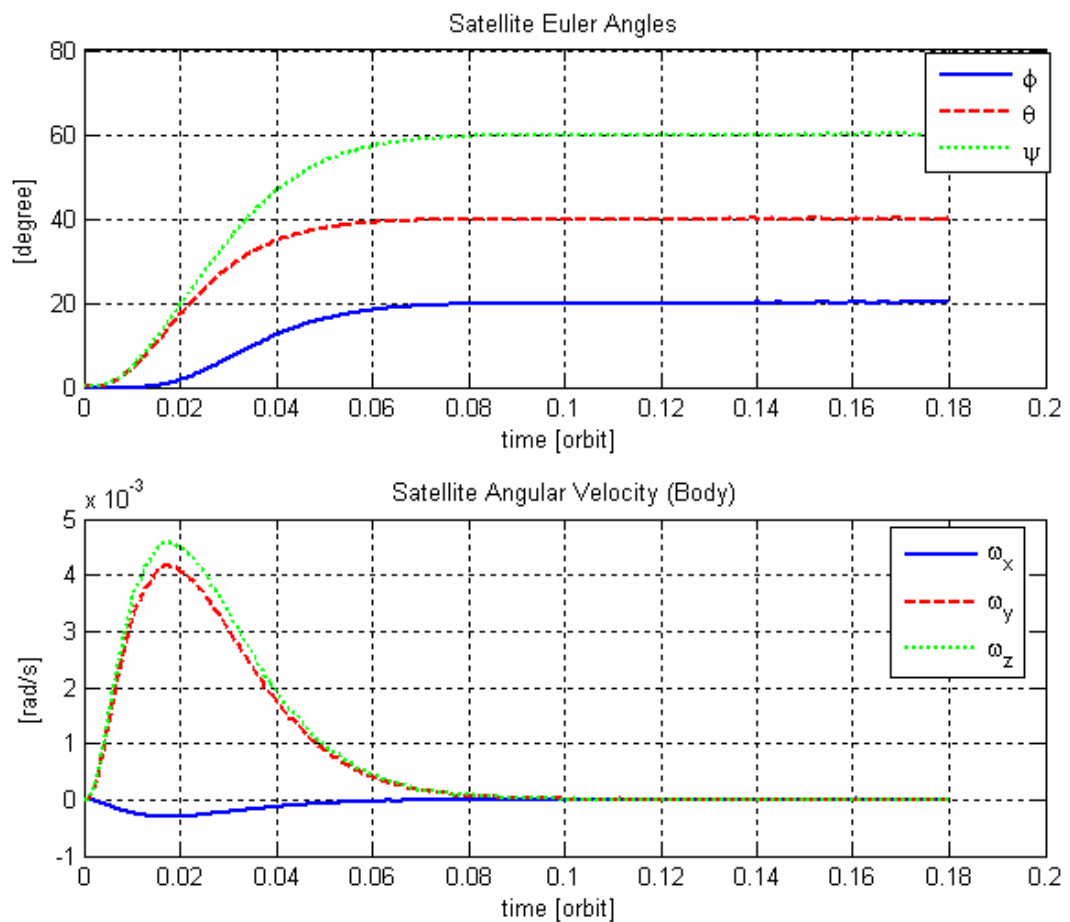


**Figure 4.5:** Satellite Desired Euler Angles and Angular Velocity with Noise Effect.

The trajectories for the Euler angles and angular velocity are not effected from the noise added to the system. Euler angles reach their final value after 0.08 orbits. On the other hand, torque output trajectories given in Figure 4.6 have distortions. The oscillations on them do not affect the overall system response. The system compensates the noise effect perfectly.

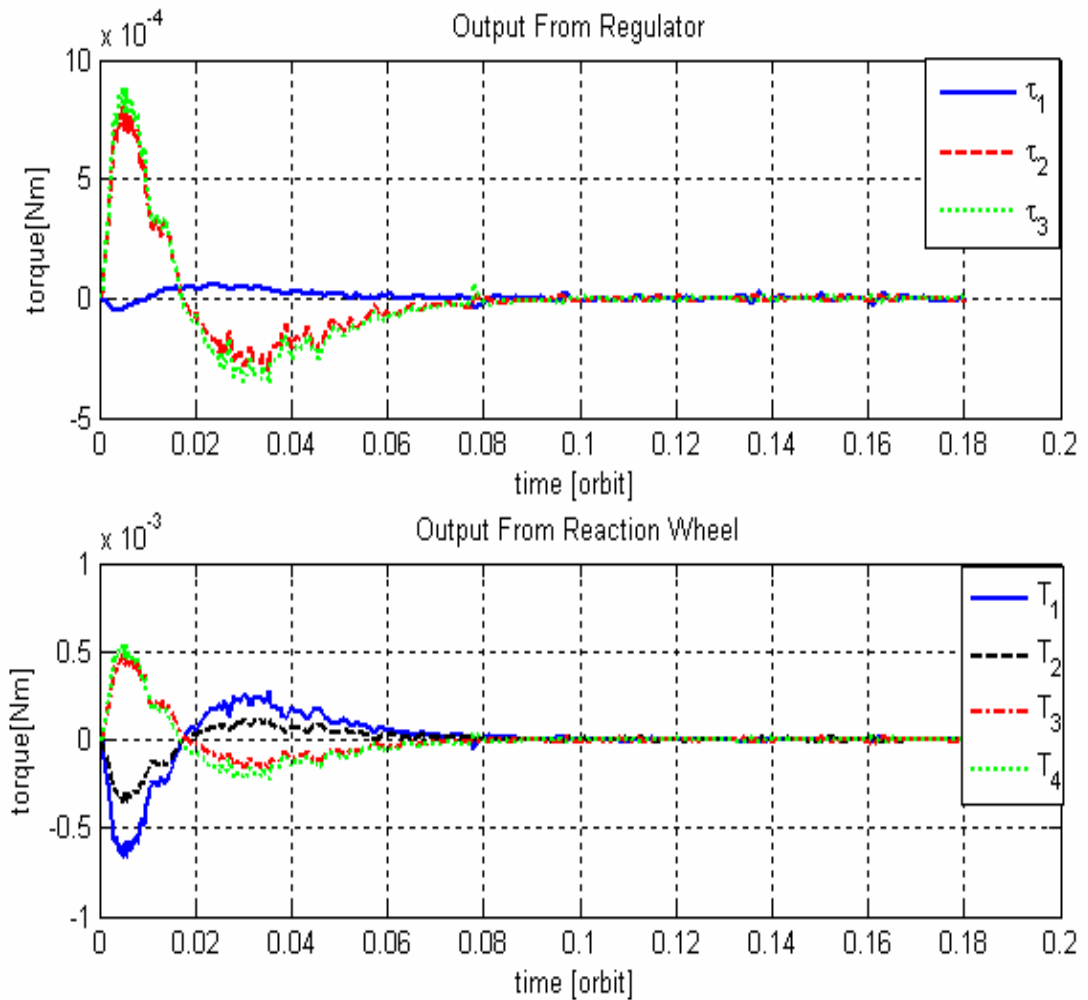


**Figure 4.6:** Outputs from the Regulator and Reaction Wheels with Noise Effect.

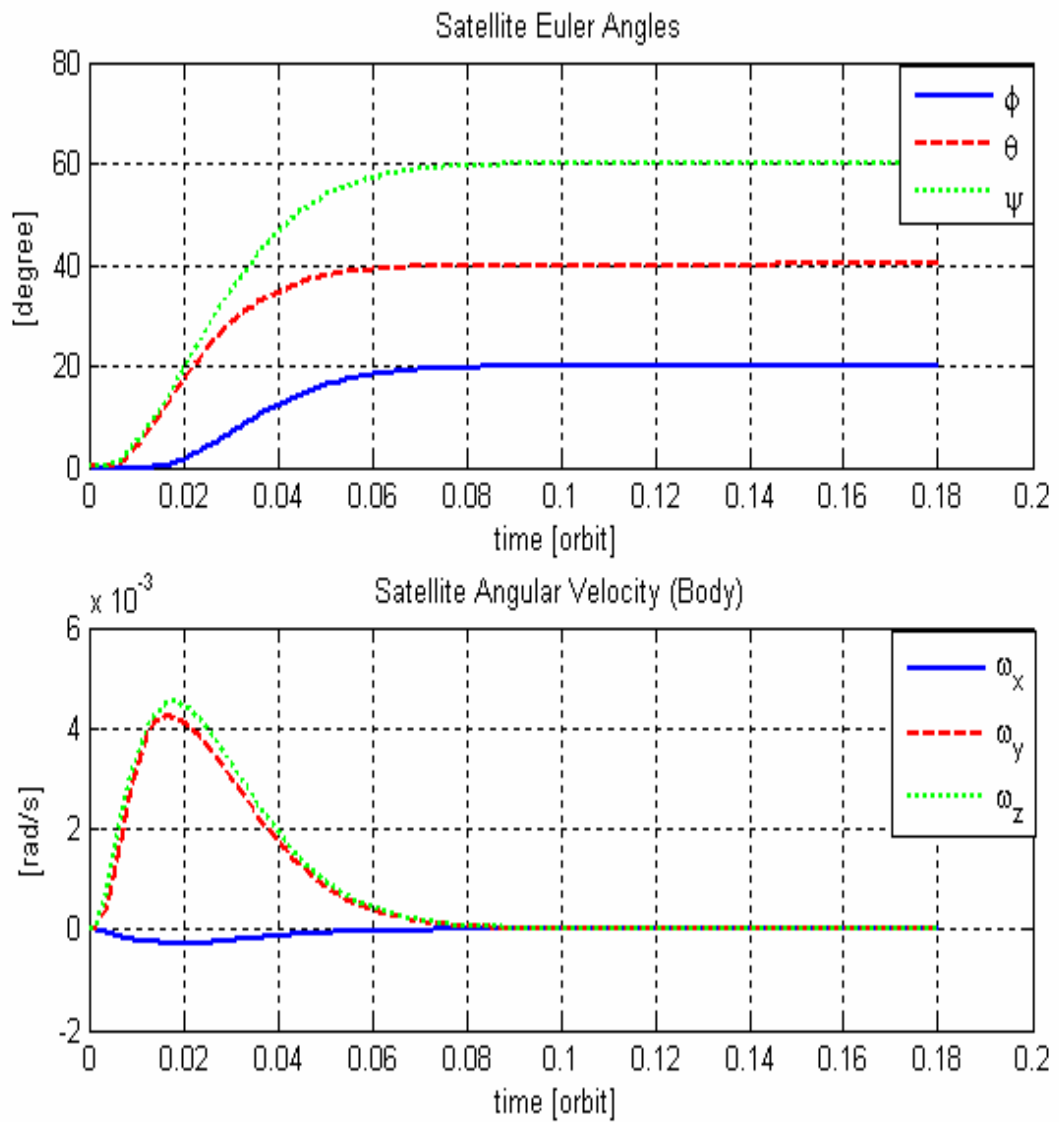


**Figure 4.7:** Satellite Desired Euler Angles and Angular Velocity When Wheel 2 is Disabled.

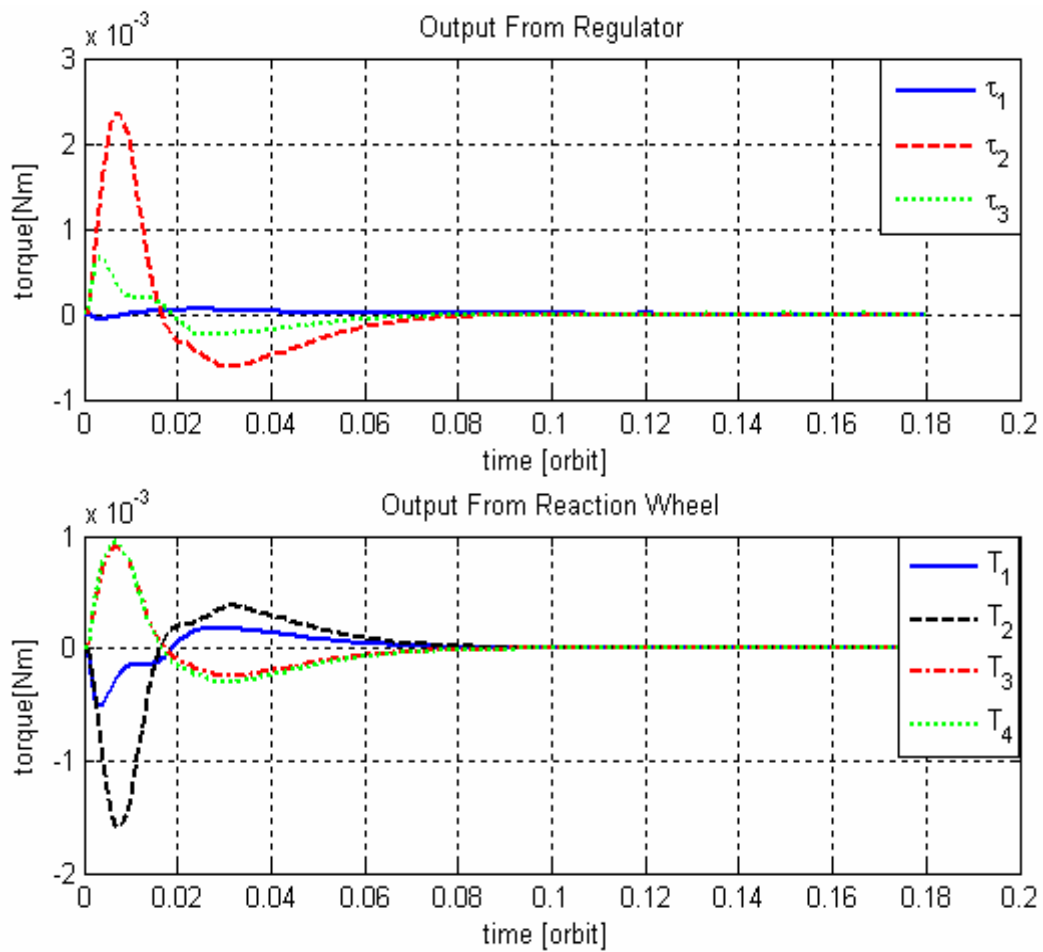


**Figure 4.8:** Outputs from the Regulator and Reaction Wheels When Wheel 2 is Disabled.

It can be easily seen that disabling one of the wheels does not affect the response of the system for the Case 3. Euler angles reach the desired value at about 0.08 orbits. This is mainly because of the tetrahedral configuration of the reaction wheels. Disabling one wheel has no effect on the response, since the others can compensate this lack on the three axes. This is experimented by disabling wheels one by one and examining the results of the simulations. It is observed that disabling one different wheel at each time has no effect on the simulation result. So only one of the observations is stated here. It is easily seen from the graph that the disabled wheel does not produce torque.

On the other hand, disabling two wheels causes the system response to fail as shown in Figure 4.9. Euler angles, as expected, do not reach their desired values.

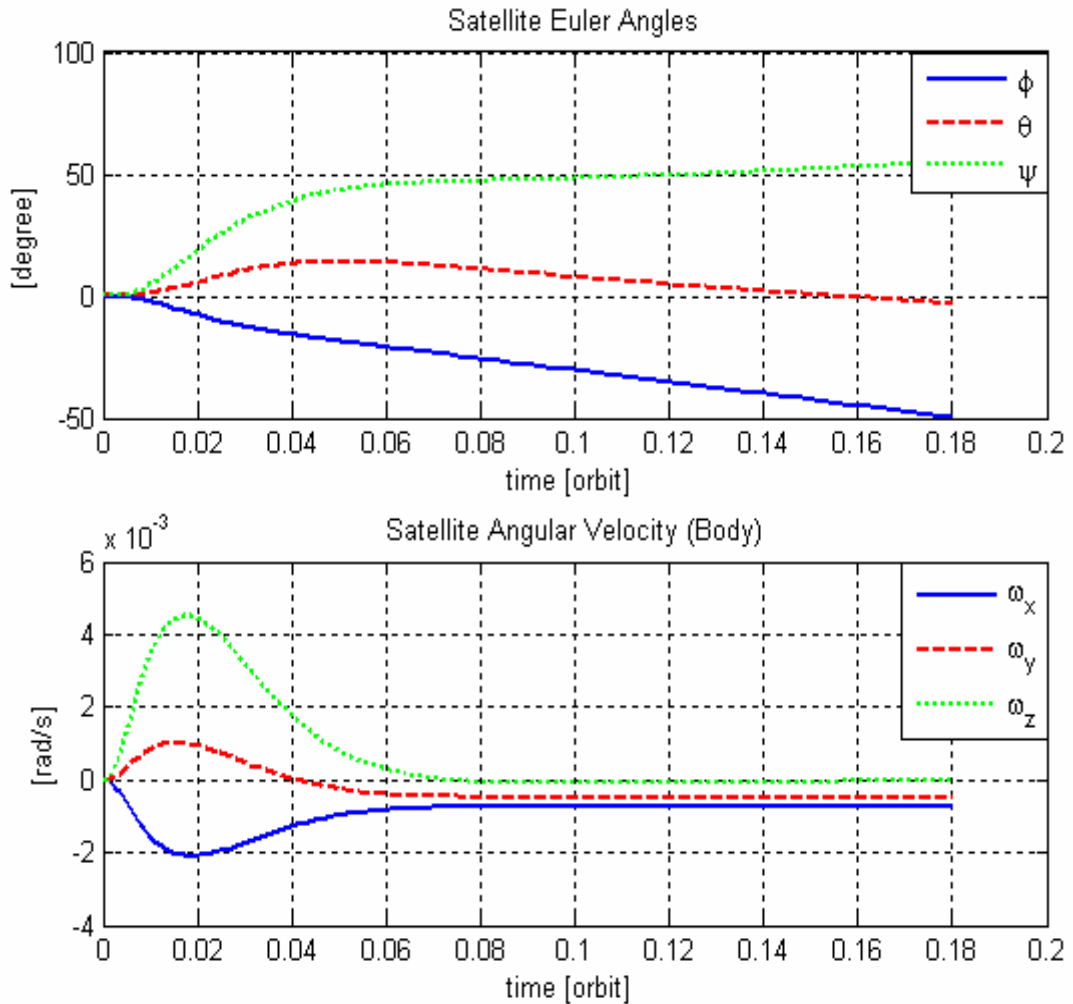


**Figure 4.9:** Satellite Euler Angles and Angular Velocity When Wheel 2 and 3 are Disabled.

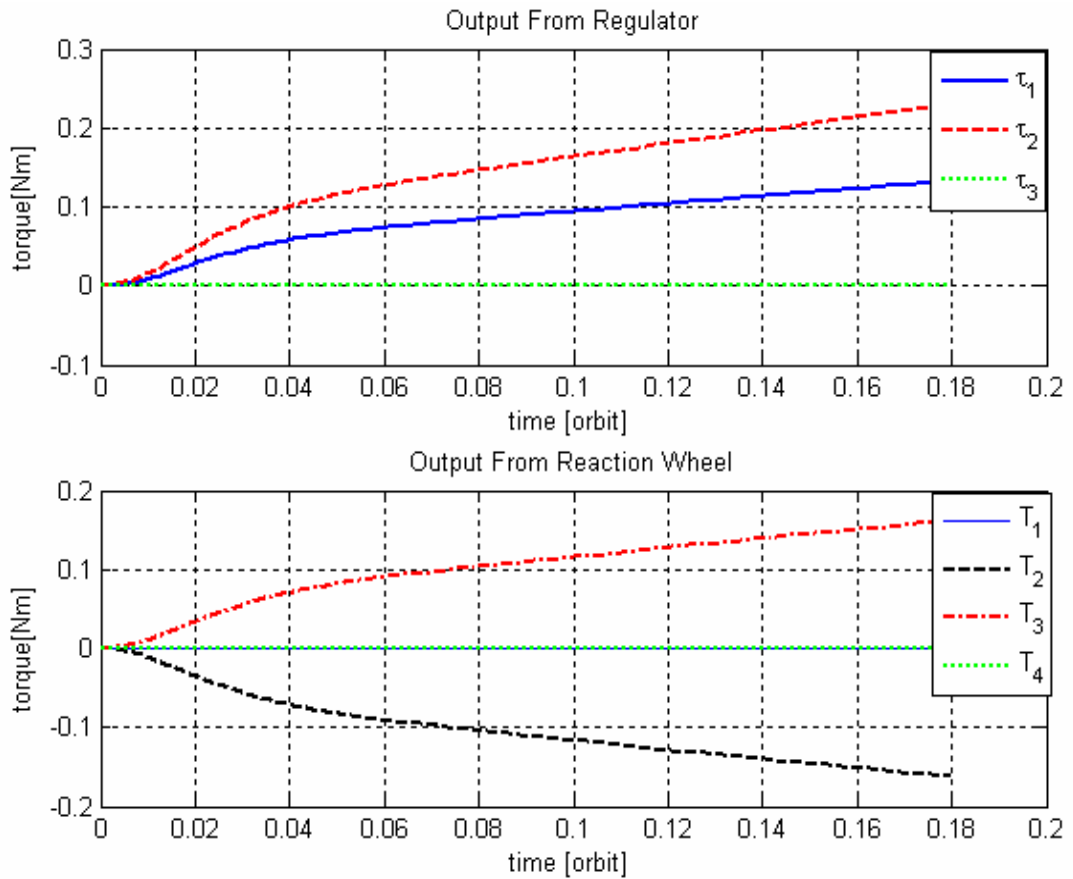


**Figure 4.10:** Outputs from the Regulator and Reaction Wheels When Wheel 2 and 3 are Disabled.

The last case simulates the maneuver of the satellite in only one direction. For this case, pitch angle is selected as  $30^{\circ}$ , roll and yaw angles are set to zero. Figure 4.11 represents the Euler angles and angular velocity. The roll angle reaches its final value at about 0.08 orbits after the start of the simulation. It is smoothly set to the value of  $30^{\circ}$ .

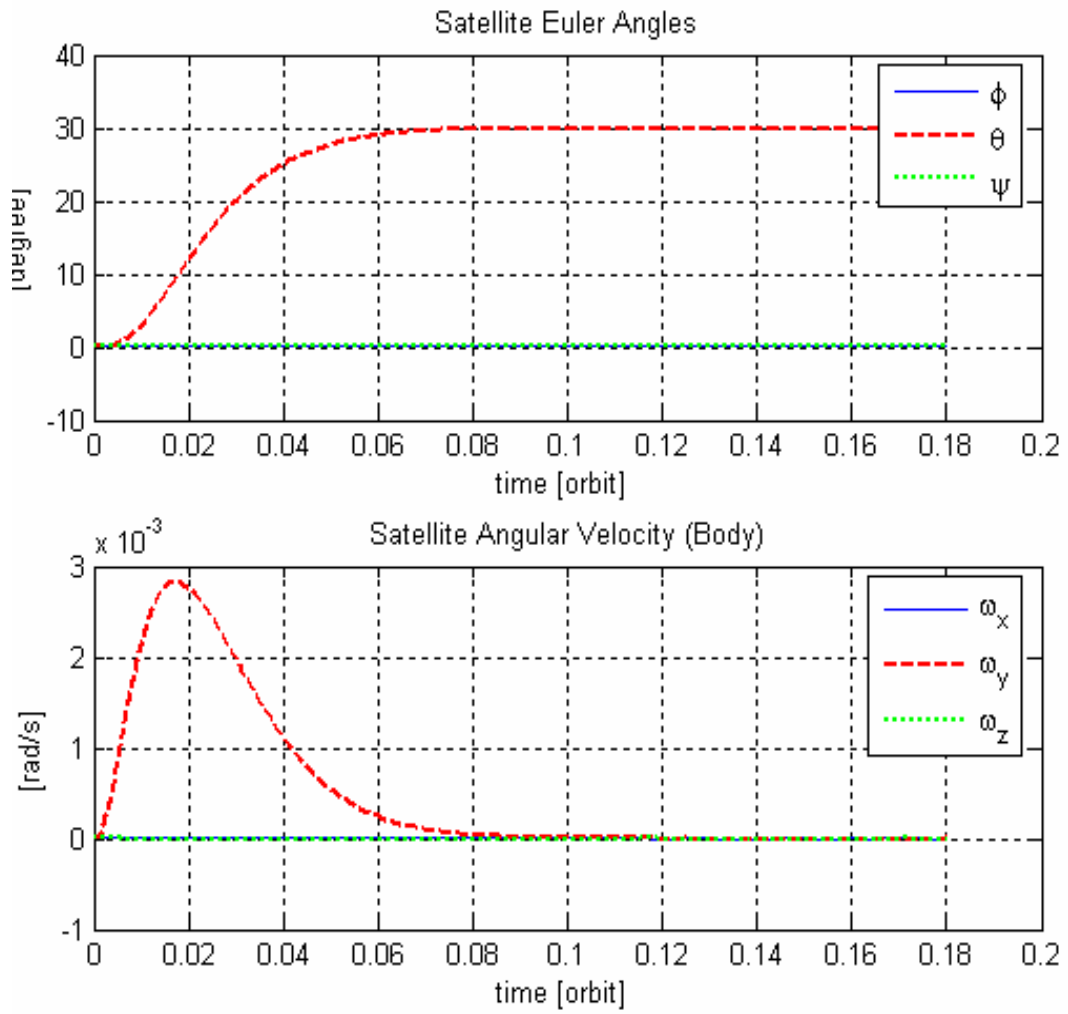


**Figure 4.11:** Satellite Euler Angles and Angular Velocity with Pitch Angle= $30^\circ$ .

Figure 4.12 represents the outputs of the regulator and reaction wheels. The figure is given on the next page.

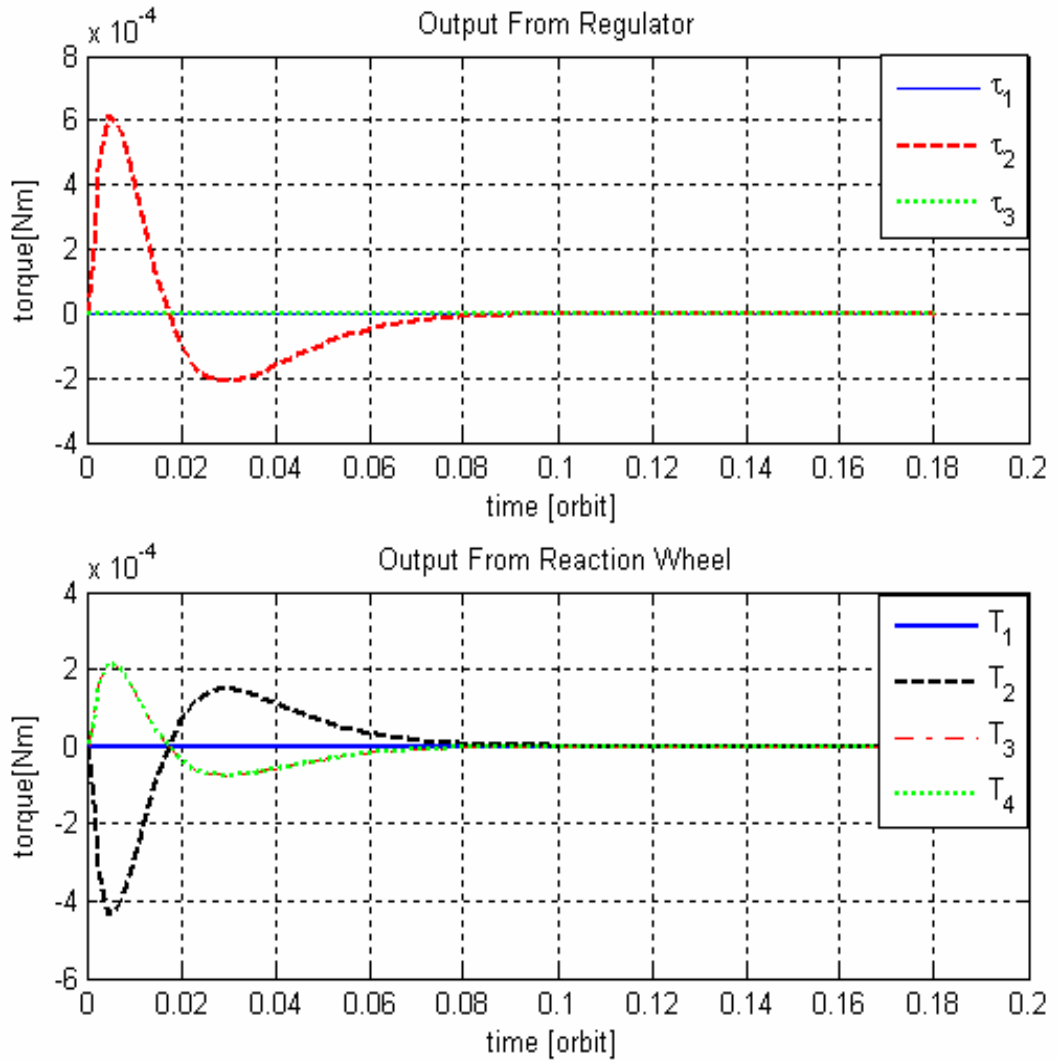


**Figure 4.12:** Outputs of the Regulator and Reaction Wheels with Pitch Angle= $30^0$ .

Lastly, the real response results taken from Tübitak-Bilten for BILSAT-1 are shown below. Table 4.3 lists the commands given for a  $30^0$  rotation around the pitch axis of the satellite.

**Table 4.3:** Command Table for BILSAT-1.

20 March 2006 02:22:00 UTC	Pitch=+30 degree command
20 March 2006 02:37:00 UTC	Pitch=0 degree command
20 March 2006 02:52:00 UTC	Pitch=+30 degree command
20 March 2006 03:07:00 UTC	Pitch=0 degree command
20 March 2006 04:02:00 UTC	Pitch=-30 degree command
20 March 2006 04:17:00 UTC	Pitch=0 degree command
20 March 2006 04:32:00 UTC	Pitch=-30 degree command
20 March 2006 04:47:00 UTC	Pitch=0 degree command
20 March 2006 05:37:00 UTC	Pitch=-30 degree command
20 March 2006 05:52:00 UTC	Pitch=0 degree command
20 March 2006 06:07:00 UTC	Pitch=+30 degree command
20 March 2006 06:22:00 UTC	Pitch=0 degree command

The pitch angle response of BILSAT-1 is shown in Figure 4.13. Horizontal axis denotes time and vertical axis denotes pitch angle.

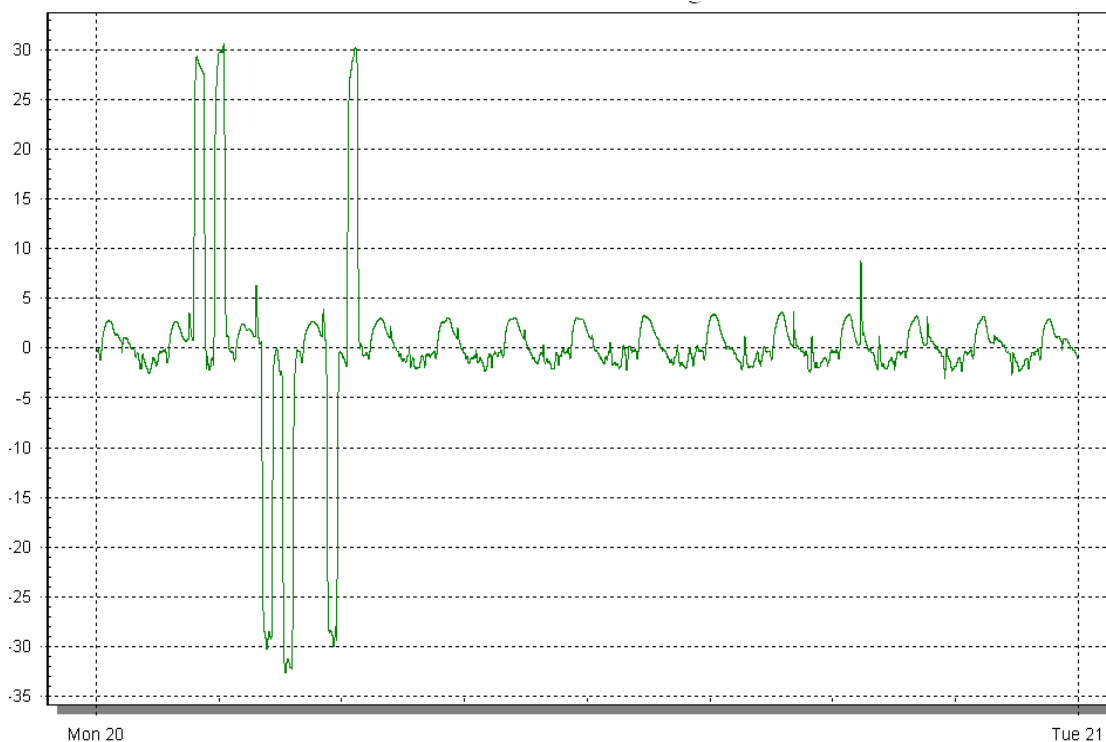


**Figure 4.13:** Pitch Angle vs. Time Graph According to Commands Taken from Table 4.3.

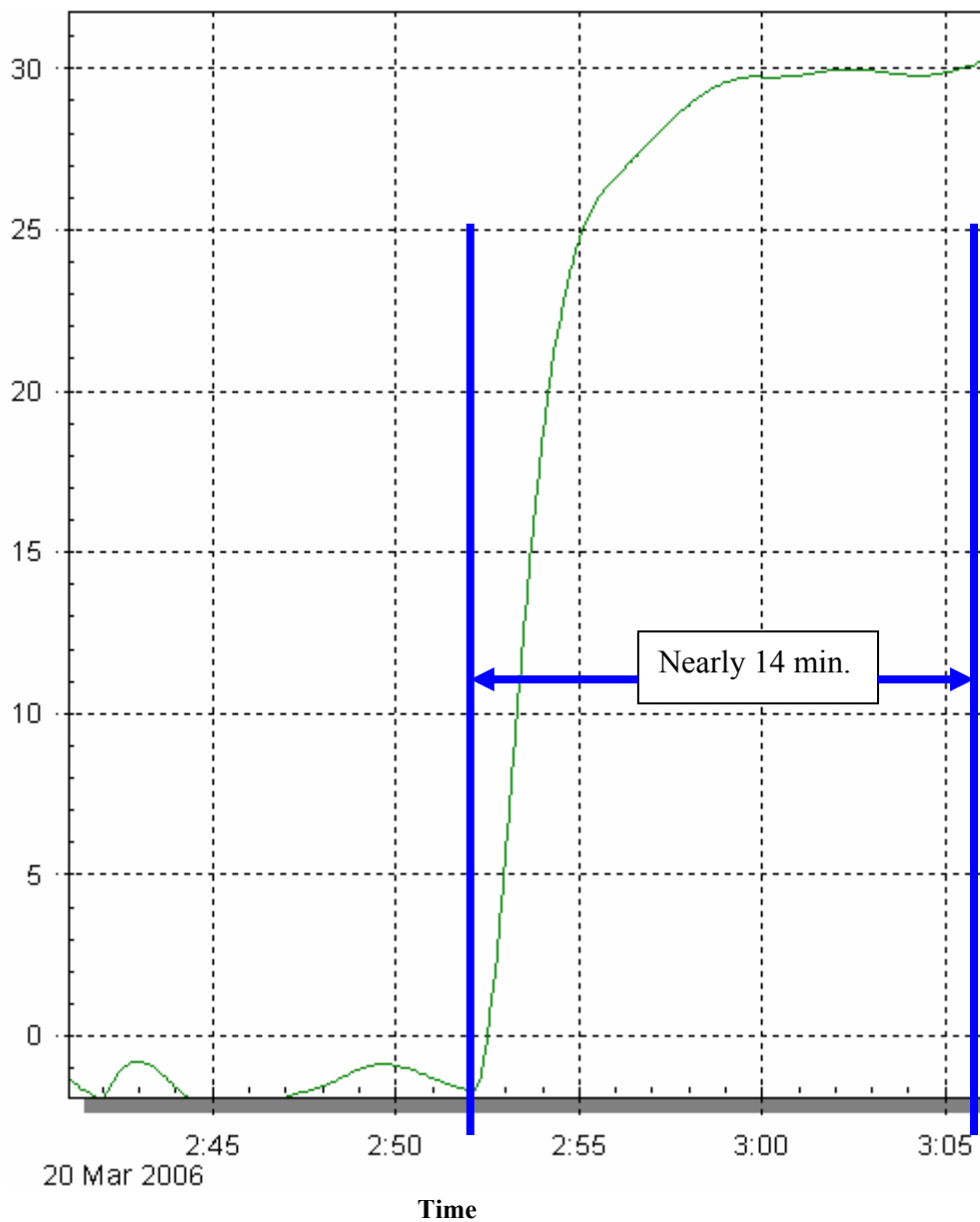


**Figure 4.14:** Zoomed Pitch Angle vs. Time Graph.

When the response shown in Figure 4.13 is zoomed to 02:52:00 UTC - 03:06:00 UTC time segment, the response in Figure 4.14 is obtained. It is interesting to see that this real time response from BILSAT-1 is similar to the one obtained in Figure 4.11. The time needed to reach  $30^{\circ}$  is nearly 14 minutes which corresponds to 0.1 orbit time when compared with our simulations. According to our simulation results, pitch angle reaches its desired value nearly in about 0.1 orbit time.

## 4.4 Simulation Results with Magnetic Torquers as Actuators

### 4.4.1 Linear Quadratic Regulator

Control input in linear quadratic regulator controller is given as:

$$u(t) = -P^{-1}B^T R x(t) \quad (4.5)$$

Weight matrices Q and P are defined in Equation 3.106 and 3.107. Here, the total number of states ( $n_s$ ) is equal to six and total number of actuators ( $n_a$ ) is equal to three.

In LQR control, Matlab code, *lqr* is applied to the design as given below:

$$[K]= \text{lqr}(A,B,Q,P) \quad (4.6)$$

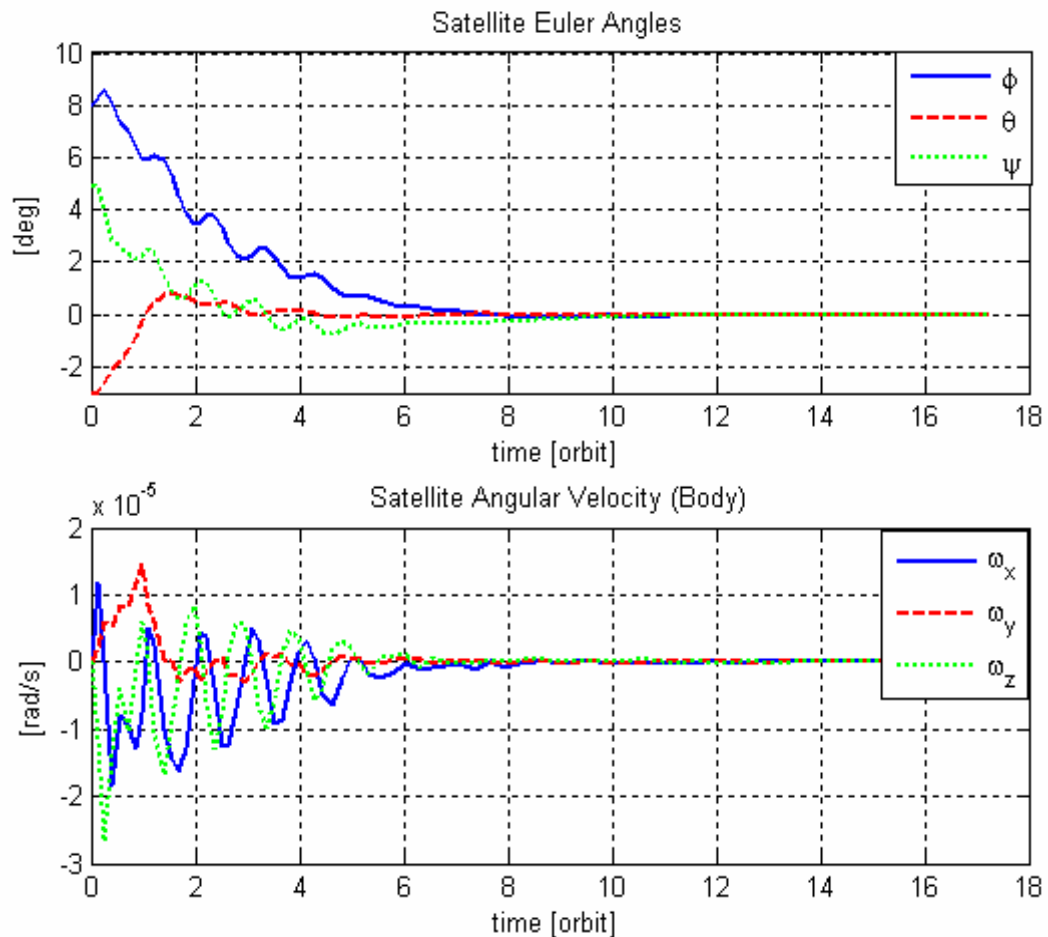
*lqr(A,B,Q,P)* calculates the optimal gain matrix K such that the state-feedback law,  $u = -Kx$ , minimizes the quadratic cost function in Equation 3.105 for the state-space model.

Initial conditions and controller parameters used in the simulations are given in Table 4.4.

**Table 4.4:** Initial Values of the Parameters.

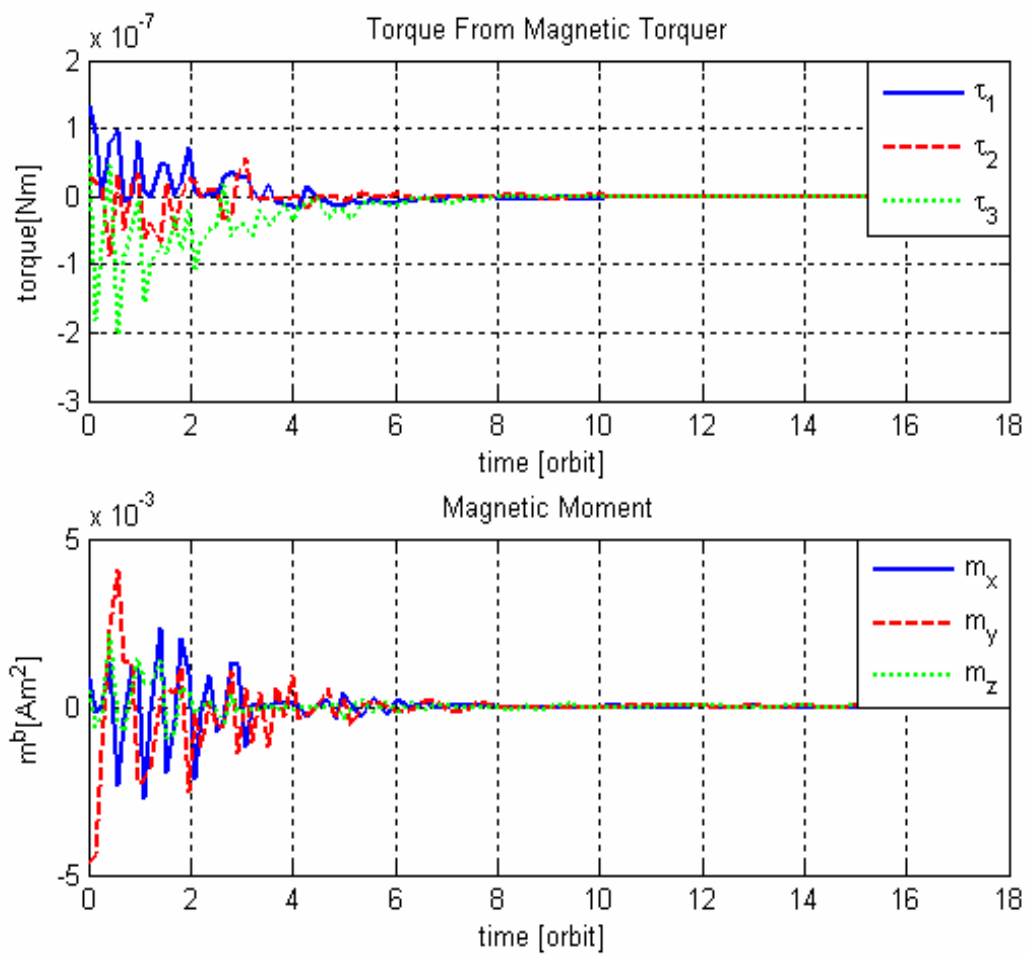
PARAMETERS	INITIAL VALUE
Angular Velocity	$\omega_{ob}^b = [0 \ 0 \ 0]^T$
Euler Angles $[\phi \ \theta \ \psi]$	$[8 \ -5 \ 3]$
Desired Euler Angles $[\phi \ \theta \ \psi]$	$[0 \ 0 \ 0]$
Maximum Dipole Moment ( $\Delta u_i$ )	0.01
State Deviation( $\Delta x_i$ )	$10 * \frac{\pi}{180}$
Q	$\text{diag}([1 \ 0 \ 1 \ 0 \ 1 \ 0]) * \text{inv}(10 * \pi / 180)^2$
P	$\text{diag}([1 \ 1 \ 1]) * \text{inv}(0.01)^2$

Figure 4.15 and 4.16 shows the simulation results when the initial conditions given above are applied to the system.



**Figure 4.15:** Satellite Euler Angles and Angular Velocity of the System.

The top view graph in Figure 4.15 represents the Euler Angles response according to the given initial condition in Table 4.3. It is observed that Euler Angles reach to the equilibrium point after 10 orbits. In fact, they are never actually equal to the zero. But small deviations can be tolerated. The performance of the system changes according to the different values of weight matrices P and Q. The values of the weight matrices are decided after several trials.



**Figure 4.16:** Torque from Magnetic Torquer and Magnetic Moment.

Magnetic moment and torque nearly reach zero after 8 orbit time. Although they have an oscillatory response, stability is maintained at the end of the simulation. According to Wisniewski [22] and Overby [7], linear quadratic regulator is an alternative way to maintain stability around the equilibrium points. This method is tolerable to small angle changes around the equilibrium points. It is useful when it is applied to the systems where it is desired to keep the system stable in a small region around the equilibrium point.

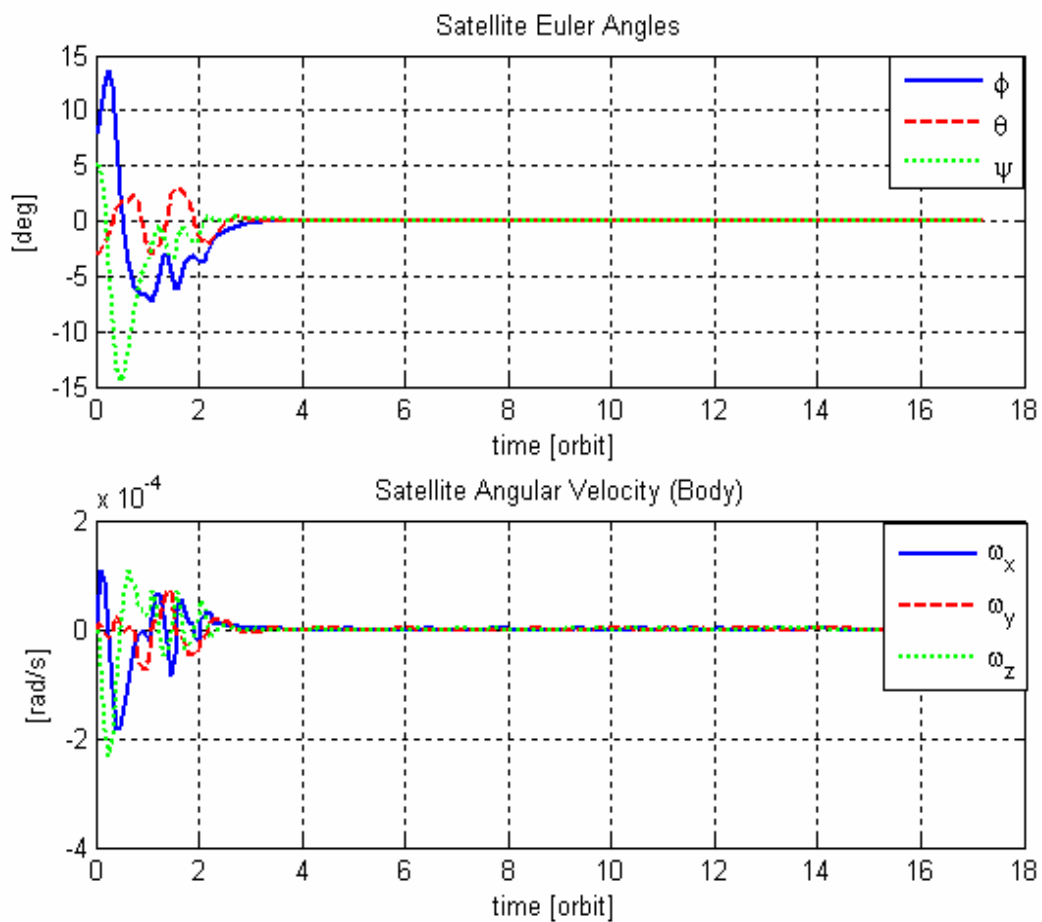


**Figure 4.17:** Satellite Euler Angles and Angular Velocity of the System for Case 2.

Case 2 represents the simulations with  $\mathbf{Q}=\text{diag}([1 \ 0 \ 1 \ 0 \ 1 \ 0]) \cdot \text{inv}(8 \cdot \pi / 180)^2$  and  $\mathbf{P}=\text{diag}([1 \ 1 \ 1]) \cdot \text{inv}(0.1)^2$ . It is easily observed in Figure 4.17 that the time to reach equilibrium points is reduced to 4 orbit time. On the other hand, torque produced by magnetic torquers is increased as it is given in Figure 4.18.

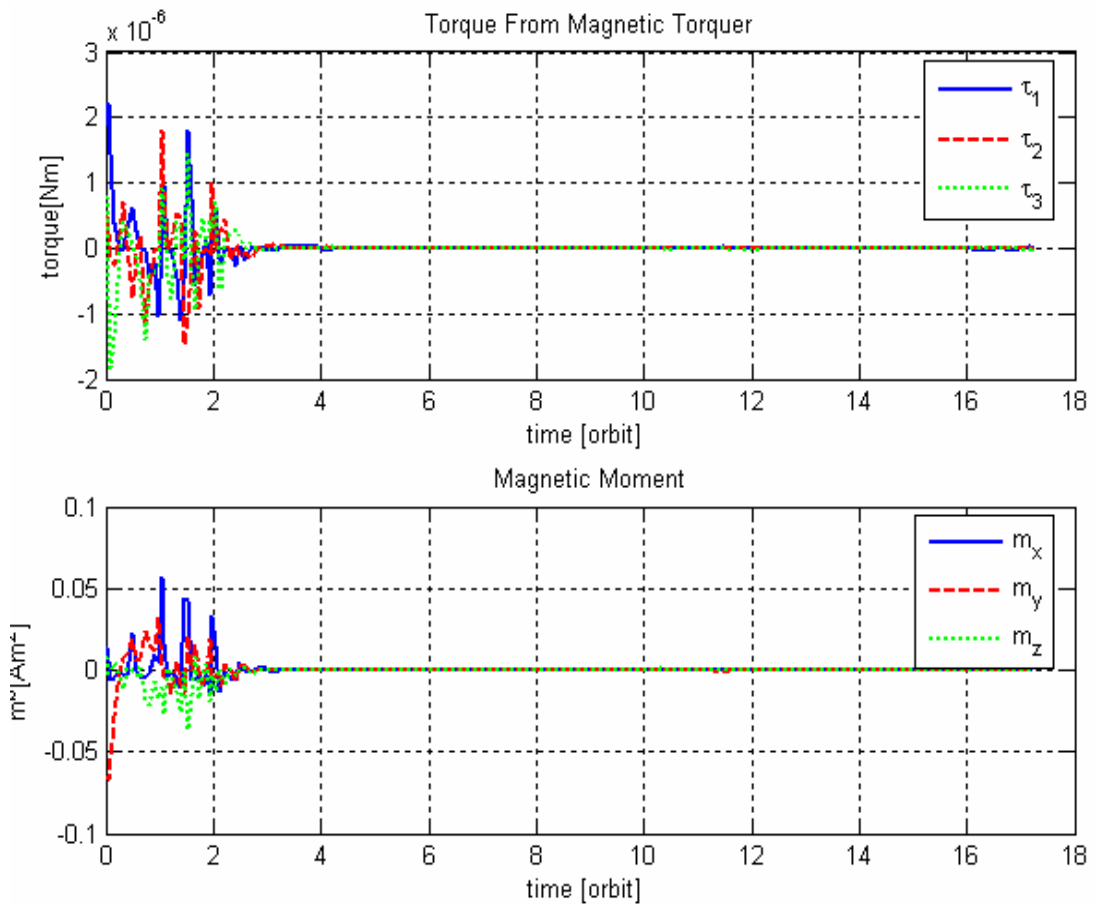


**Figure 4.18:** Torque from Magnetic Torquer and Magnetic Moment for Case 2.

In simulations for linear quadratic regulator, aerodynamic torque is not taken into consideration. It can be concluded that selection of P and Q depends on the design scheme. If it is important to reach equilibrium points as soon as possible, Case 2 can be recommended. On the other hand, if power consumption is important design criteria, then Case 1 can be taken into consideration.

## 4.5 Sensitivity Analysis

Sensitivity analysis of the system response to different controller parameters is done by observing the changes on the settling time, the rise time, the steady state error and the torque value obtained from actuators when the control parameters are changed

within a range. Table 4.5 and Table 4.6 on the next pages, show the different values of the control parameters and system responses corresponding to these values. In Table 4.5, the effect of changing the weights in P and Q matrices to the system response is analyzed. First the P matrix is kept constant while changing the weights of the Q matrix in the range  $\frac{1}{(13\pi/180)}$  to  $\frac{1}{(7\pi/180)}$ . Then the Q matrix is kept constant while changing the weights of P matrix in the range  $\frac{1}{0.01}$  to 1. When the system response is considered, it is observed that system response elements (settling time, the rise time, the steady state error and the torque value obtained from actuators) are sensitive to changes on the control parameters.

In Table 4.6, pole values are changed in the range  $0.1 \pm 0.1i$  to  $0.9 \pm 0.9i$ . The pole values greater than 1 cause oscillations and unstabilities on the system response. When the system response is considered, it is observed that system response elements (settling time, the rise time, the steady state error and the torque value obtained from actuators) do not change due to changes on the control parameters. It is worth to mention that the observed changes are so small that they are neglected.

**Table 4.5 :** Sensitivity of the System Response to Control Parameter Changes for Linear Quadratic Regulator.

CONTROL PARAMETERS	SETTLING TIME(ORBIT)	RISE TIME(ORBIT)	STEADY STATE ERROR	MAX. TORQUE FROM ACTUATOR(mNm)
$Q=\text{diag}([1\ 0\ 1\ 0\ 1\ 0])*\text{inv}(13*\pi/180)^2$ $P=\text{diag}([1\ 1\ 1])*\text{inv}(0.01)^2$	4	2.3	0.002	$1.2*10^{-6}$
$Q=\text{diag}([1\ 0\ 1\ 0\ 1\ 0])*\text{inv}(12*\pi/180)^2$ $P=\text{diag}([1\ 1\ 1])*\text{inv}(0.01)^2$	4	2.5	0.002	$1.5*10^{-6}$
$Q=\text{diag}([1\ 0\ 1\ 0\ 1\ 0])*\text{inv}(11*\pi/180)^2$ $P=\text{diag}([1\ 1\ 1])*\text{inv}(0.01)^2$	5	2.2	0.01	$2*10^{-6}$ -oscillations
$Q=\text{diag}([1\ 0\ 1\ 0\ 1\ 0])*\text{inv}(10*\pi/180)^2$ $P=\text{diag}([1\ 1\ 1])*\text{inv}(0.01)^2$	10	7	0	$1.2*10^{-7}$
$Q=\text{diag}([1\ 0\ 1\ 0\ 1\ 0])*\text{inv}(9*\pi/180)^2$ $P=\text{diag}([1\ 1\ 1])*\text{inv}(0.01)^2$	3	2	0.005	$2*10^{-6}$ -oscillations
$Q=\text{diag}([1\ 0\ 1\ 0\ 1\ 0])*\text{inv}(8*\pi/180)^2$ $P=\text{diag}([1\ 1\ 1])*\text{inv}(0.01)^2$	4	3	0.01	$2*10^{-6}$
$Q=\text{diag}([1\ 0\ 1\ 0\ 1\ 0])*\text{inv}(7*\pi/180)^2$ $P=\text{diag}([1\ 1\ 1])*\text{inv}(0.01)^2$	3-oscillations	2	0.03	$2*10^{-6}$ -oscillations
$Q=\text{diag}([1\ 0\ 1\ 0\ 1\ 0])*\text{inv}(10*\pi/180)^2$ $P=\text{diag}([1\ 1\ 1])*\text{inv}(0.01)^2$	10	7	0	$1.2*10^{-7}$
$Q=\text{diag}([1\ 0\ 1\ 0\ 1\ 0])*\text{inv}(10*\pi/180)^2$ $P=\text{diag}([1\ 1\ 1])*\text{inv}(0.05)^2$	4.2	2.5	0.006	$0.8*10^{-6}$
$Q=\text{diag}([1\ 0\ 1\ 0\ 1\ 0])*\text{inv}(10*\pi/180)^2$ $P=\text{diag}([1\ 1\ 1])*\text{inv}(0.1)^2$	10	8	0.001	$1,2*10^{-7}$
$Q=\text{diag}([1\ 0\ 1\ 0\ 1\ 0])*\text{inv}(8*\pi/180)^2$ $P=\text{diag}([1\ 1\ 1])*\text{inv}(0.5)^2$	oscillations	oscillations	oscillations	oscillations
$Q=\text{diag}([1\ 0\ 1\ 0\ 1\ 0])*\text{inv}(8*\pi/180)^2$ $P=\text{diag}([1\ 1\ 1])*\text{inv}(1)^2$	oscillations	oscillations	oscillations	oscillations

**Table 4.6 :** Sensitivity of the System Response to Control Parameter Changes for Linear Controller.

<b>CONTROL PARAMETERS</b>	<b>SETTLING TIME(ORBIT)</b>	<b>RISE TIME(ORBIT)</b>	<b>STEADY STATE ERROR</b>	<b>MAX. TORQUE FROM ACTUATOR(mNm)</b>
<b>P1=0.1+0.1i ; P2=0.1-0.1i</b>	0.08	0.04	0	$6 \cdot 10^{-4}$
<b>P1=0.2+0.2i ; P2=0.2-0.2i</b>	0.1	0.04	0	$2 \cdot 10^{-4}$
<b>P1=0.3+0.3i ; P2=0.3-0.3i</b>	0.1	0.04	0	$2 \cdot 10^{-4}$
<b>P1=0.5+0.5i ; P2=0.5-0.5i</b>	0.1	0.04	0	$2 \cdot 10^{-4}$
<b>P1=0.9+0.9i ; P2=0.9-0.9i</b>	0.1	0.04	0	$2 \cdot 10^{-4}$ -oscillations

## CHAPTER V

### CONCLUSION AND FUTURE WORK

In this work, attitude determination and control components are introduced in detail. Mathematical model of the satellite dynamics is derived and linearized. The model is modified according to the BILSAT-1 satellite parameters. Linear attitude control techniques for a Low-Earth Orbit satellite are considered. Throughout this thesis, two different modes of the satellite are examined with two different actuators. These modes are attitude stabilization and attitude maneuver. In attitude stabilization, magnetic torquers are used as actuators and linear quadratic regulator is selected as the control method. On the other hand, actuators of the attitude maneuver mode are reaction wheels and linear state feedback is applied for attitude control.

Simulations are done using BILSAT-1 dynamic model, and for different cases all of which uses linear controllers. According to the cases explained and simulated in Chapter IV, the following concluding remarks can be stated: Euler angles of the system satisfy the desired values( [20 40 60]) in 0.08 orbit time nearly in all cases except Case 4 which represents the disabling of two reaction wheels at the same time. The rise time of the response is about 0.06 orbit time. Addition of uniformly distributed noise to the system as an external torque, has an effect on the trajectory of the torque obtained from reaction wheels. Although maximum and minimum torque values do not change, distortions take place on trajectories. Since these oscillations are very small in value, they do not effect the overall system simulations. If these distortions have larger values (because of the effect of the internal disturbance torques or vice versa) rather than the small values considered in our simulations, reaction wheels can go into saturation. So, if needed, an extra control system should be added to the system for limiting and adjusting reaction wheels' torque values, or

dynamic model of the reaction wheels shall be designed in order to overcome the effects of the oscillations. In Case 3, one of the reaction wheels is disabled in order to prove the effectiveness of the tetrahedral configuration. Simulation results in Chapter IV show that Euler angles reach their final value within 0.08 orbit time again for Case 3. On the other hand, maximum and minimum torque values for the reaction wheels and time to settle are increased. This increase is a result of distributing the moments to three reaction wheels rather than four reaction wheels on three axis. In other words, distribution matrix torque values are distributed over three remaining reaction wheels causing an increase on the torque values. In the case of disabling two wheels, the simulation results failed and Euler angles no more reach to the given desired values. The last case simulated is an attitude maneuver on pitch direction with an angle of  $30^0$ . It is observed that reaction wheels two and four are effective throughout the maneuvering process. Compared with the simulation results taken from BILSAT-1 log data, the rise time (0.06 orbit time for BILSAT-1 simulations and nearly 0.06 orbit time for our simulations) and settling time (nearly 0.1 orbit time for BILSAT-1 simulations and 0.08 orbit time for our simulations) are found to be comparable to our simulations. This comparison is useful to prove that the linear controller designed here is applicable although ideal cases (circular orbit instead of elliptic, diagonal inertia matrix instead of nondiagonal) for satellite environment are taken into consideration. The last case (Case 5) is also compared with the results obtained from nonlinear control methods studied in Reference [26]. Table 4.7 given below, summarizes the system responses for different control methods. It can be concluded from the table that sliding mode regulator is better way of control compared to linear controller in terms of response time.

**Table 4.7 :** Comparison of the System Response for Different Control Methods.

Controller	Rise Time	Settling Time	Max-Min Reaction Wheel Torques
Linear Controller	0.03	0.08	2e-4/-4e-4
*Quaternion Feedback Controller	0.04	0.09	4.5e-4/-4.5e-4
*Sliding Mode Regulator	0.04	0.07	2e-4/-4e-4
BILSAT-1	0.04	0.14	**
*Control methods applied in Reference [26] **The torque values of BILSAT-1 log data are not comparable since actuator model is different.			

Finally, it is worth to mention that K gain matrix value selection and reference model design by adjusting the values of  $\omega_n$  are important design criterias in linear controller design. The pole values given in this thesis are obtained after several experiments and the ideas taken from the Reference [7]. According to Reference [7], actuators are saturated and overshoots are exaggerated when pole placement is done with poles too much away from origin. Fast oscillations can be introduced to the system, if poles have relatively large imaginary roots. This increases the fuel consumption in real-life applications. These recommendations are taken into account during pole selection and pole values are given as  $-0.1+0.1j$  and  $-0.1-0.1j$  in this work. The obtained long rise time and settling time values can be reduced by adjusting the values of  $\omega_n$  (i.e.  $\omega_n=0.5$ ). But this will result in an increase at the torque values of reaction wheels which in turn means more power consumption.

The linear controller method is also compared with nonlinear controllers studied in Reference [26]. In general, simulations results follow the same trajectory for Euler angles except that the roll angle in nonlinear control, maintains its initial value 0.02 orbits time greater than the one in linear controller simulation results. On the other hand, the rise time for Euler angle trajectories in nonlinear control methods are a bit smaller ( $\cong 0.05$  orbit time). Also, nonlinear controller methods are more effective in

terms of torque values needed from reaction wheels. Reaction wheels have produced less torque values thus, reducing the power consumed. As a result, nonlinear control methods are more effective compared to the linear controller.

The controller for attitude stabilization mode is selected as linear quadratic regulator. This controller is also examined in Reference [7]. In this controller, choosing the proper weight values for P and Q is important to avoid oscillations and to shorten the response time. It can easily be seen from Figures 4.15 and 4.16 that system converges to the equilibrium point after 8 orbit time. This is a very long response time compared to the simulations obtained from linear controller. The reason for that is the use of magnetic torquers as actuators. Figures 4.17 and 4.18 are obtained by adjusting different values for P and Q weight matrices. In Figure 4.17, Euler angles reach to the equilibrium point after 4 orbit time. On the other hand, the torque values become larger when compared with the case in Figure 4.16. This simulation shows the importance of choosing proper P and Q values. One can select different values for weights according to the design criterias (power consumption, fast/slow recovery of disturbances.)

For future work, It is worth to implement a reaction wheel model similar to the one used in BILSAT-1 (rather than the method used in this work), and then compare results of the simulations with those obtained from BILSAT-1 log data. Also, in this work, mathematical modelling of the satellite and environmental torques are derived according to the ideal cases. For example, inertia matrix is taken in diagonal form and satellite orbit is assumed to be circular. The system can be modelled without these assumptions in order to model the satellite and its environment in a more realistic way. Lastly, as it was mentioned earlier, linear quadratic regulator is a way to maintain stability in a small region around the equilibrium point (as is the case in most linearizations, the model gives realistic results for small disturbances around equilibrium point). So, It is suggested to find an alternative nonlinear control method that maintains stability in case of large angle deviations and existence of the environmental disturbances (e.g. aerodynamic torque) in attitude stabilization mode.

## REFERENCES

- [1] Andy Bradford, Luis M. Gomes, Prof. Sir Martin Sweeting, Gökhan Yüksel, Cem Özkaptan, Ünsal Orlu, “A Low-Cost, Agile, Earth Observation Microsatellite For Turkey”, IAC-02-IAA.11.3.02, 53<sup>rd</sup> International Astronautical Congress, October 2002 .
- [2] Uğur Murat Leloğlu, Gökhan Yüksel, Prof. Sir Martin N. Sweeting, “BILSAT-1: A Case Study For the Survey Satellite Technology Ltd. Know-How Transfer and Training Programme”, 53<sup>rd</sup> International Astronautical Congress, 10-19 Oct 2002.
- [3] Luis M. Gomes, Gökhan Yüksel, Alex da Silva Cerial, Andy Bradford, Prof. Sir Martin Sweeting, “BILSAT-1: Advancing Small-Sat Capabilities”, SS C03-VI-4, 17<sup>th</sup> AIAA/USU Conference on Small Satellites.
- [4] Neslin İsmailoğlu, Oğuz Benderli, Ilgaz Korkmaz, Mehmet Duna, Taner Kolçak, Y. Çağatay Tekmen, “A Real Time Image Processing Subsystem: Gezgin”, Proceedings of 16<sup>th</sup> AIAA/USU Conference on Small Satellites, ,USA, August 2002.
- [5] J.R. Wertz and W.J. Larson, Space Mission Analysis and Design, Library of Congress Cataloging-in-Publication Data, , 3<sup>rd</sup> Edition, 1999.
- [6] D. A. Vallado, Fundamentals of Astrodynamics and Applications, Microcosm/ Kluwer Academic Publishers, 2<sup>nd</sup> Edition, 2001.
- [7] E. Jerpseth Overby, “Attitude Control for the Norwegian Student Satellite N-Cube”, M.Sc. Thesis in NTNU, 2004
- [8] James R. Wertz, Spacecraft Attitude Determination and Control, Kluwer Academic Publishers, Netherlands, 1997.

- [9] Hakkı Özgür Derman, “3-Axis Control of Geostationary Satellite”, M.Sc. Thesis, M.E.T.U. , 1999.
- [10] Vladimir A. Chobotov, Spacecraft Attitude Dynamics and Control, Krieger Publishing Co., Florida, 1991.
- [11] P.J. Rimroh, Introductory Attitude Dynamics and Control, John Wiley and Sons, USA, 1976.
- [12] F. M. Indergaard, “Design and Implementation of a Gravity Boom for the Norwegian Nanosatellite NCUBE”, M.Sc. Thesis, NTNU, 2003.
- [13] Kyrkjebo, Erik, “Satellite Attitude Determination, 3-Axis Attitude Determination Using Magnetometers and a Star Tracker”, Siv. Ing. Thesis, Department of Engineering Cybernetics, NTNU, 2000.
- [14] M. H. Kaplan, Modern Spacecraft Dynamics and Control, John Wiley & Sons, USA, 1976.
- [15] Özge Uslu, “Orbit Dynamics, Attitude Dynamics and Control Investigation into Possible Applications to TÜRKSAT”, M.Sc. Thesis in Aeronautical Engineering, M.E.T.U., Ankara, January, 1997.
- [16] Chris Hall, “HokieSat Attitude and Orbit Dynamics and Control.”, Aeronautics and Astronautics, University of Illinois, March 31, 2003.
- [17] Stian Sondersrod Ose, “Attitude Determination for the Norwegian Student Satellite NCUBE”, M.Sc. Thesis, Department Of Engineering Cybernetics, NTNU, Norway, 2004.
- [18] Egeland & Gravdahl , Jan Tommy, Modeling and simulation for control, Lecture Notes, Department of Engineering Cybernetics, NTNU, 2001.

- [19] Kristian Svartveit, "Attitude Determination of the NCUBE Satellite", M.Sc. Thesis in Department Of Engineering Cybernetics, June, 2003.
- [20] Mortar Pedersen Topland, "Nonlinear Attitude Control of the Microsatellite ESEO", M.Sc. Thesis in Department Of Engineering Cybernetics, NTNU, July, 2004.
- [21] Bjorn Even Busterud, "Orienteringsregulering ow Microsatelliter", M.Sc. Thesis in Department Of Engineering Cybernetics, NTNU, 2003.
- [22] R. Wisniewski & M. Blanke, "Satellite Attitude Control Using Only Electromagnetic Actuation", Ph.D. Thesis, Department Of Control Engineering, Aalborg University, Denmark, 1996.
- [23] Geir Ytrehus, "Styring av Mikrosatellitt med Reaksijonshjul i Tetraeder", M.Sc. Thesis in Department Of Engineering Cybernetics, NTNU, 2003.
- [24] Webpage:  
[www.agi.com/downloads/corporate/partners/edu/advancedSunsensorproject](http://www.agi.com/downloads/corporate/partners/edu/advancedSunsensorproject)
- [25] Fullmer Rees, "Attitude Determination and Control", paper, Mechanical and Aerospace Engineering, Utah University, 1993.
- [26] Karataş Soner, "BILSAT-1: Attitude Dynamics and Some Nonlinear Control Techniques", M.Sc. Thesis in Department of Electrical and Electronics Engineering, METU, 2006.
- [27] Web page : <http://www.sstl.co.uk>

# APPENDIX A

## MATHEMATICAL DERIVATIONS

### A.1 Linearization of Mathematical Model

The linearization points are selected as,

$$q = \begin{bmatrix} 1 \\ 0 \end{bmatrix} \quad (\text{A.1})$$

The kinematic model of the satellite is given in Equation A.2.

$$\dot{q} = \begin{bmatrix} \dot{\eta} \\ \dot{\varepsilon} \end{bmatrix} = \frac{1}{2} \begin{bmatrix} -\varepsilon^T \\ \eta I_{3 \times 3} + S(\varepsilon) \end{bmatrix} \omega_{bo}^b \quad (\text{A.2})$$

Applying linearization points to Equation A.2, the following equation is obtained.

$$\dot{q} = \begin{bmatrix} \dot{\eta} \\ \dot{\varepsilon} \end{bmatrix} = \frac{1}{2} \begin{bmatrix} 0 \\ \omega_{bo}^b \end{bmatrix}, \quad \omega_{bo}^b = 2\dot{\varepsilon} \quad (\text{A.3})$$

The rotation matrix in the form of,

$$R_b^o = I + 2\eta S(\varepsilon) + S^2(\varepsilon) \quad (\text{A.4})$$

becomes Equation A.5 when linearized ,

$$R_b^o = I + 2\eta S(\varepsilon) \quad (\text{A.5})$$

Hence, taking in to account the fact that  $R_o^b = (R_b^o)^T$ . The linearized rotation matrix,  $R_o^b$  becomes:

$$R_o^b = I - 2\eta S(\varepsilon) \quad (\text{A.6})$$

Equation A.6 turns out to be:

$$R_o^b = 2 \begin{bmatrix} \frac{1}{2} & \varepsilon_3 & -\varepsilon_2 \\ -\varepsilon_3 & \frac{1}{2} & \varepsilon_1 \\ \varepsilon_2 & -\varepsilon_1 & \frac{1}{2} \end{bmatrix} \quad (\text{A.7})$$

The linearized model of  $\omega_{bi}^b$ , angular velocity, ( $\omega_{bo}^b = 2\dot{\varepsilon}$ ) is derived as:

$$\omega_{bi}^b = \begin{bmatrix} \omega_x \\ \omega_y \\ \omega_z \end{bmatrix} = \begin{bmatrix} 2\dot{\varepsilon}_1 - 2\omega_o \varepsilon_3 \\ 2\dot{\varepsilon}_2 - \omega_o \\ 2\dot{\varepsilon}_3 + 2\omega_o \varepsilon_1 \end{bmatrix} \quad (\text{A.8})$$

The time derivative of  $\omega_{bi}^b$  is given as :

$$\dot{\omega}_{bi}^b = \begin{bmatrix} \dot{\omega}_x \\ \dot{\omega}_y \\ \dot{\omega}_z \end{bmatrix} = \begin{bmatrix} 2\ddot{\varepsilon}_1 - 2\omega_o \dot{\varepsilon}_3 \\ 2\ddot{\varepsilon}_2 \\ 2\ddot{\varepsilon}_3 + 2\omega_o \dot{\varepsilon}_1 \end{bmatrix} \quad (\text{A.9})$$

When linearized, gravitational torque simplifies to:

$$\tau_{grav}^b = 3\omega_o^2 \begin{bmatrix} 2(I_z - I_y)\varepsilon_1 \\ 2(I_x - I_z)\varepsilon_2 \\ 0 \end{bmatrix} \quad (\text{A.10})$$

Magnetic torquers model is linearized around  $\eta = 1$  and  $\varepsilon = 0$  and gives:

$$\tau_m^b = S(m^b)B^o = \begin{bmatrix} B_z^o m_y - B_y^o m_z \\ B_x^o m_z - B_z^o m_x \\ B_y^o m_x - B_x^o m_y \end{bmatrix} \quad (\text{A.11})$$

Reaction wheel dynamic equations is linearized around the point where  $\omega_{bi}^b = 0$  and Equation A.12 is obtained.

$$\tau_r^b = \left(\frac{dL_r}{dt}\right)^b = \begin{bmatrix} \dot{L}_{rx} \\ \dot{L}_{ry} \\ \dot{L}_{rz} \end{bmatrix} \quad (\text{A.12})$$

## A.2 Satellite Linearized Model for Linear Controller

Mathematical model of the satellite when reaction wheels are the actuators of the satellite can also be given in the form as :

$$I\dot{\omega}_{bi}^b = -\omega_{bi}^b \times (I\omega_{bi}^b) + \tau_{grav}^b + \left(\frac{dL}{dt}\right)^b \quad (\text{A.13})$$

The cross product operator [18],  $\times$ , is defined by:

$$\lambda \times a : S(\lambda)a \quad (\text{A.14})$$

The skew-symmetric matrix  $S(\lambda)$  is defined as,

$$S(\lambda) = -S(\lambda)^T := \begin{bmatrix} 0 & -\lambda_3 & \lambda_2 \\ \lambda_3 & 0 & -\lambda_1 \\ -\lambda_2 & \lambda_1 & 0 \end{bmatrix} \quad (\text{A.15})$$

When Equation A.8, A.9, A.10, A.11, and A.15 are applied to Equation A.13, the following equations are obtained.

$$\begin{aligned}
I_x(2\ddot{\varepsilon}_1 - 2\dot{\varepsilon}_3\omega_0) &= -[I_y(2\dot{\varepsilon}_3 + 2\varepsilon_1\omega_0)(2\dot{\varepsilon}_2 - \omega_0) + I_z(2\dot{\varepsilon}_3 + 2\varepsilon_1\omega_0)(2\dot{\varepsilon}_2 - \omega_0)] + 6\omega_0^2(I_z - I_y)\varepsilon_1 + \frac{dL_x}{dt} \\
2I_y\ddot{\varepsilon}_2 &= -[I_x((2\dot{\varepsilon}_3 + 2\varepsilon_1\omega_0)(2\dot{\varepsilon}_1 - 2\varepsilon_3\omega_0) - I_z(2\dot{\varepsilon}_3 + 2\varepsilon_1\omega_0)(2\dot{\varepsilon}_1 - 2\varepsilon_3\omega_0))] + 6\omega_0^2(I_x - I_z)\varepsilon_2 + \frac{dL_y}{dt} \\
I_z(2\ddot{\varepsilon}_3 + 2\dot{\varepsilon}_1\omega_0) &= -[I_x(2\dot{\varepsilon}_2 - \omega_0)(2\dot{\varepsilon}_1 - 2\varepsilon_3\omega_0) + I_y(2\dot{\varepsilon}_2 - \omega_0)(2\dot{\varepsilon}_1 - 2\varepsilon_3\omega_0)] + \frac{dL_z}{dt}
\end{aligned} \tag{A.16}$$

and Equation A.16 becomes:

$$\begin{aligned}
\ddot{\varepsilon}_1 &= (1 - k_x)\omega_0\dot{\varepsilon}_3 - 4k_x\omega_0^2\varepsilon_1 + \frac{1}{2I_x}(\dot{L}_{rx}) \\
\ddot{\varepsilon}_2 &= -3k_y\omega_0^2\varepsilon_2 + \frac{1}{2I_y}(\dot{L}_{ry}) \\
\ddot{\varepsilon}_3 &= -(1 - k_z)\omega_0\dot{\varepsilon}_1 - k_z\omega_0^2\varepsilon_3 + \frac{1}{2I_z}(\dot{L}_{rz})
\end{aligned} \tag{A.17}$$

with

$$\begin{aligned}
k_x &= \frac{I_y - I_z}{I_x} \\
k_y &= \frac{I_x - I_z}{I_y} \\
k_z &= \frac{I_y - I_x}{I_z}
\end{aligned} \tag{A.18}$$

Representing the time derivative of the Equation A.13 with quaternion parameters helps to derive the state-space representation in linear form, given below:

$$\dot{x}(t) = Ax(t) + B(t)u(t) \tag{A.19}$$

where  $x = [\varepsilon_1 \quad \dot{\varepsilon}_1 \quad \varepsilon_2 \quad \dot{\varepsilon}_2 \quad \varepsilon_3 \quad \dot{\varepsilon}_3]$  and  $u = [\dot{L}_{rx} \quad \dot{L}_{ry} \quad \dot{L}_{rz}]^T$ .

The A matrix is derived as given in Equation A.20.

$$A = \begin{bmatrix} 0 & 1 & 0 & 0 & 0 & 0 \\ -4k_x\omega_o^2 & 0 & 0 & 0 & 0 & (1-k_x)\omega_o \\ 0 & 0 & 0 & 1 & 0 & 0 \\ 0 & 0 & -3k_y\omega_o^2 & 0 & 0 & 0 \\ 0 & 0 & 0 & 0 & 0 & 1 \\ 0 & -(1-k_z)\omega_o & 0 & 0 & -k_z\omega_o^2 & 0 \end{bmatrix} \quad (\text{A.20})$$

The B matrix turns out to be:

$$B(t) = \begin{bmatrix} 0 & 0 & 0 \\ \frac{1}{2I_x} & 0 & 0 \\ 0 & 0 & 0 \\ 0 & \frac{1}{2I_y} & 0 \\ 0 & 0 & 0 \\ 0 & 0 & \frac{1}{2I_z} \end{bmatrix} \quad (\text{A.21})$$

### A.3 Satellite Linearized Model for Linear Quadratic Regulator

Mathematical model of the satellite with magnetic torquers as actuators,

$$I\dot{\omega}_{bi}^b = -\omega_{bi}^b \times (I\omega_{bi}^i) + S(m^b B^o) + \tau_{grav}^b \quad (\text{A.22})$$

Equation A.22 becomes Equation A.23, when Equations A.8, A.9, A.10, A.11, and A.15 are applied to Equation A.22.

$$\begin{aligned}
I_x(2\ddot{\varepsilon}_1 - 2\dot{\varepsilon}_3\omega_0) &= -\left[-I_y(2\dot{\varepsilon}_3 + 2\varepsilon_1\omega_0)(2\dot{\varepsilon}_2 - \omega_0) + I_z(2\dot{\varepsilon}_3 + 2\varepsilon_1\omega_0)(2\dot{\varepsilon}_2 - \omega_0)\right] + 6\omega_0^2(I_z - I_y)\varepsilon_1 + B_z^o m_y - B_y^o m_z \\
2I_y\ddot{\varepsilon}_2 &= -\left[I_x((2\dot{\varepsilon}_3 + 2\varepsilon_1\omega_0)(2\dot{\varepsilon}_1 - 2\varepsilon_3\omega_0) - I_z(2\dot{\varepsilon}_3 + 2\varepsilon_1\omega_0)(2\dot{\varepsilon}_1 - 2\varepsilon_3\omega_0))\right] + 6\omega_0^2(I_x - I_z)\varepsilon_2 + B_x^o m_z - B_z^o m_x \\
I_z(2\ddot{\varepsilon}_3 + 2\dot{\varepsilon}_1\omega_0) &= -\left[-I_x(2\dot{\varepsilon}_2 - \omega_0)(2\dot{\varepsilon}_1 - 2\varepsilon_3\omega_0) + I_y(2\dot{\varepsilon}_2 - \omega_0)(2\dot{\varepsilon}_1 - 2\varepsilon_3\omega_0)\right] + B_y^o m_x - B_x^o m_y
\end{aligned} \tag{A.23}$$

and Equation A.16 becomes:

$$\begin{aligned}
\ddot{\varepsilon}_1 &= (1 - k_x)\omega_0\dot{\varepsilon}_3 - 4k_x\omega_0^2\varepsilon_1 + \frac{1}{2I_x}(B_z^o m_y - B_y^o m_z) \\
\ddot{\varepsilon}_2 &= -3k_y\omega_0^2\varepsilon_2 + \frac{1}{2I_y}(B_x^o m_z - B_z^o m_x) \\
\ddot{\varepsilon}_3 &= -(1 - k_z)\omega_0\dot{\varepsilon}_1 - k_z\omega_0^2\varepsilon_3 + \frac{1}{2I_z}(B_y^o m_x - B_x^o m_y)
\end{aligned} \tag{A.24}$$

with

$$\begin{aligned}
k_x &= \frac{I_y - I_z}{I_x} \\
k_y &= \frac{I_x - I_z}{I_y} \\
k_z &= \frac{I_y - I_x}{I_z}
\end{aligned} \tag{A.25}$$

Equation A.22 is represented by state-space representation in linear form in Equation A.26

$$\dot{x}(t) = Ax(t) + B(t)u(t) \tag{A.26}$$

where  $x = [\varepsilon_1 \quad \dot{\varepsilon}_1 \quad \varepsilon_2 \quad \dot{\varepsilon}_2 \quad \varepsilon_3 \quad \dot{\varepsilon}_3]$  and  $u = [m_x \quad m_y \quad m_z]^T$ .

The A matrix is found as given in Equation A.27.

$$A = \begin{bmatrix} 0 & 1 & 0 & 0 & 0 & 0 \\ -4k_x\omega_o^2 & 0 & 0 & 0 & 0 & (1-k_x)\omega_o \\ 0 & 0 & 0 & 1 & 0 & 0 \\ 0 & 0 & -3k_y\omega_o^2 & 0 & 0 & 0 \\ 0 & 0 & 0 & 0 & 0 & 1 \\ 0 & -(1-k_z)\omega_o & 0 & 0 & -k_z\omega_o^2 & 0 \end{bmatrix} \quad (\text{A.27})$$

The B matrix is found to be:

$$B(t) = \begin{bmatrix} 0 & 0 & 0 \\ 0 & \frac{1}{2I_x}B_z^o & -\frac{1}{2I_x}B_y^o \\ 0 & 0 & 0 \\ -\frac{1}{2I_y}B_z^o & 0 & \frac{1}{2I_y}B_x^o \\ 0 & 0 & 0 \\ \frac{1}{2I_x}B_y^o & -\frac{1}{2I_x}B_x^o & 0 \end{bmatrix} \quad (\text{A.28})$$

### A.3 Some Mathematical Models

#### A.3.1 Rate Sensors (Gyroscopes)

The relationship between the rate about the input axis and the angular displacement,  $\theta$ , about the output axis may be derived by the total angular momentum,  $H$ , of the gyro system, [8].

$$H = L + I_o \dot{\theta} \hat{O} \quad (\text{A.29})$$

Where  $L = L\hat{S}$ , is the angular momentum of the rotor,  $I_o$  is the moment of inertia of the gimbal system about the output axis,  $\hat{O}$  is a unit vector in the

direction of the gyro's output axis, and  $\hat{S}$  is a unit vector in the direction of the gyro's spin axis. When Newton's Laws applied to the system [8] ,

$$\sum Torques = \left(\frac{dH}{dt}\right)_{inertial} = \left(\frac{dH}{dt}\right)_{Gyro} + \omega \times H \quad (A.30)$$

The torque on the single-degree-of-freedom gyro is the sum of restoring and viscous damping terms,

$$\sum Torques = -(K\theta + D\dot{\theta})\hat{O} \quad (A.31)$$

then

$$I_o\ddot{\theta} + D\dot{\theta} + K\theta - \omega_l L = 0 \quad ; \quad \omega \equiv \omega_l \hat{I} + \omega_o \hat{O} + \omega_s \hat{S} \quad (A.32)$$

The steady state solution to equation above :

$$\theta = \frac{\omega_l L}{K} \quad (A.33)$$

The output of the RG is proportional to the angular rate about the input axis.

In BILSAT, control moment gyros are used. Therefore, below parts expresses gyroscope's mathematical model and calculation of angular velocity in detail.

### A.3.1.1 Mathematical Models for Gyroscopes

As stated before, gyroscopes are used in attitude propagation and control. This section describes the mathematical models for the estimation of spacecraft angular rates from gyro measurements.

The gyro output,  $\theta$ , represents a voltage proportional to the torque current in an analog rebalanced gyro. The relationship between  $\theta$  and  $\omega_i$ , the angular rate component in the direction of the gyros input axis depends on the gyro used. In rate gyros ,

$$\omega_i^M = K_R \theta_R \quad (\text{A.34})$$

where  $\omega_i^M$  is the gyro's measurement of  $\omega_i$  , and  $K_R$  is the rate gyro scale factor.

For rate-integrating gyros , the gyro's measurement of angular velocity over the interval is:

$$\omega_i^M = \frac{K_I \theta_I}{\delta t_I} \quad (\text{A.35})$$

where is the rate-integrating scale factor. The interval,  $\delta t_I$  , typically 200 to 500 ms.

The model for measured spacecraft angular velocity taken from Iwens and Farrenkopf [1971],

$$\omega_i^M = (1 + k_i)\omega_i + b_i + n_i \quad (\text{A.36})$$

$\omega_i$  is the spacecraft's angular velocity in the direction of the gyro's input axis,  $\omega_i^M$  gyro's measurement of this quantity,  $k_i$  is the small correction to the nominal scale factor,  $b_i$  is the drift rate,  $n_i$  is the white noise on the gyro output.

If the direction of the gyro's input axis is given by a unit vector,  $\hat{U}_i$ , in the spacecraft coordinate frame, then

$$\omega_i^M = (1 + k_i)\hat{U}_i\omega + b_i + n_i \quad (\text{A.37})$$

where  $\omega$  is the true spacecraft angular velocity vector.

N single-degree-of-freedom gyros with input axes oriented to measure the three components of angular velocity vector. For N gyros , the following vectors are constructed:

$$\omega_g^M = \begin{bmatrix} \omega_{i1}^M \\ \cdot \\ \cdot \\ \cdot \\ \omega_{iN}^M \end{bmatrix}; \quad b_g = \begin{bmatrix} b_{i1} \\ \cdot \\ \cdot \\ \cdot \\ b_{iN} \end{bmatrix}; \quad n_g = \begin{bmatrix} n_{i1} \\ \cdot \\ \cdot \\ \cdot \\ n_{iN} \end{bmatrix} \quad (\text{A.38})$$

$$U = \begin{bmatrix} U_{i1}^T \\ \cdot \\ \cdot \\ \cdot \\ U_{iN}^T \end{bmatrix}; \quad K = \begin{bmatrix} 1+k_{i1} & & & & 0 \\ & \cdot & & & \\ & & \cdot & & \\ & & & \cdot & \\ 0 & & & & 1+k_{iN} \end{bmatrix} \quad (\text{A.39})$$

$$\omega_g^M = KU\omega + b_g + n_g \quad (\text{A.40})$$

$\omega_g^M$  represents the collective output of the gyro configuration.

Below expression is an algorithm for the calculation of spacecraft angular velocities from gyro measurements.

$$\omega = C(\omega_g^M - b_g - n_g) \quad \text{where} \quad C = [U^T K^T KU]^{-1} U^T K^T \quad (\text{A.41})$$

$$C = [KU]^{-1} \quad (\text{A.42})$$

in case of three gyros,

$$\langle \omega \rangle = C \omega_g^M - b = (I - G)(C \omega_g^M - b) \quad (\text{A.43})$$

G is the misalignment/scale factor correction matrix.

## A.4 Modelling the Earth's Magnetic Field

### A.4.1 IGRF Model

There are mainly two ways to find the required equations on IGRF. First way is to determine the magnetic field equations directly as given in Equation A.44.

$$B_r = -\frac{\partial V}{\partial r} = \sum_{n=1}^{\infty} \left(\frac{a}{r}\right)^{n+2} (n+1) \sum_{m=0}^n P_n^m (g_{n,m} \cos m\phi + h_{n,m} \sin m\phi) \quad (\text{A.44})$$

$$B_\theta = -\frac{1}{r} \frac{\partial V}{\partial \theta} = -\sum_{n=1}^{\infty} \left(\frac{a}{r}\right)^{n+2} (n+1) \sum_{m=0}^n \frac{\partial P_n^m}{\partial \theta} (g_{n,m} \cos m\phi + h_{n,m} \sin m\phi)$$

$$B_\phi = -\frac{1}{r \sin \theta} \frac{\partial V}{\partial \phi} = \frac{1}{\sin \theta} \sum_{n=1}^{\infty} \left(\frac{a}{r}\right)^{n+2} (n+1) \sum_{m=0}^n P_n^m (-m g_{n,m} \cos m\phi + m h_{n,m} \sin m\phi)$$

Second way is to use orbit estimator facts to find magnetic field. Implementation of orbit estimator in Earth-Centered Earth Fixed Frame is expressed in Equation A.45.

$$r^E = R_Z(-\Omega + \theta) R_X(-i) R_Z(\omega) r^{OC} \quad ; \quad r^{OC} = a \begin{bmatrix} \cos E - e \\ \sqrt{1 - e^2} \sin E \\ 0 \end{bmatrix} \quad (\text{A.45})$$

where  $\Omega$  is the right ascension of Ascending Node,  $\omega$  is the argument of Perigee,

$\theta$  is the ascension of zero meridian ,  $i$  is the inclination of the satellite,  $E$  is the eccentric anomaly and  $e$  is the eccentricity. The Figure A.1, [17] briefly shows the relationship between these parameters.

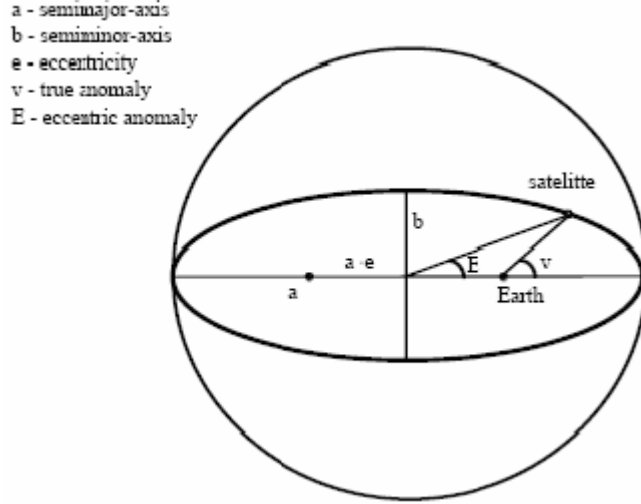


**Figure A.1:** Relationship Between Keplerian Elements.

By using Equation A.45 , magnetic field can be expressed as:

$$\begin{aligned} B^{OC} &= R_z(-\Omega + \theta)R_x(-i)R_z(\omega)B^{ECEF} \\ B^{OC} &= R_z(\omega)R_x(i)R_z(\Omega - \theta)B^{ECEF} \end{aligned} \quad (A.46)$$

where  $B^{ECEF}$  is the resultant vector from IGRF Model.

Finally, transformation to get the magnetic field in Orbit frame yields:

$$\begin{aligned} B^O &= R_x\left(\frac{\pi}{2}\right)R_z\left(v + \frac{\pi}{2}\right)B^{OC} \\ &= \begin{bmatrix} 1 & 0 & 0 \\ 0 & 0 & 1 \\ 0 & -1 & 0 \end{bmatrix} \begin{bmatrix} -\sin v & \cos v & 0 \\ -\cos v & -\sin v & 0 \\ 0 & 0 & 1 \end{bmatrix} B^{OC} \\ &= \begin{bmatrix} -\sin v & \cos v & 0 \\ 0 & 0 & 1 \\ \cos v & \sin v & 0 \end{bmatrix} B^{OC} \end{aligned} \quad (A.47)$$

## A.4.2 Dipole Model

Dipole Model is an alternative way to calculate magnetic field. Although it is not accurate as IGRF model, it can still be applied to the models.

Dipole model is calculated by using the spherical harmonic model to the first degree ( $n = 1$ ) and all orders ( $m = 0, 1$ ).

$$\begin{aligned} B_r &= 2\left(\frac{a}{r}\right)^3 [g_{1,0} \cos \theta + \sin \theta (g_{1,1} \cos m\phi + h_{1,1} \sin \phi)] \\ B_\theta &= \left(\frac{a}{r}\right)^3 [g_{1,0} \sin \theta - \cos \theta (g_{1,1} \cos m\phi + h_{1,1} \sin \phi)] \\ B_\phi &= \left(\frac{a}{r}\right)^3 [g_{1,0} \sin \phi - h_{1,1} \cos \phi] \end{aligned} \quad (\text{A.48})$$

Earth's magnetic field can also be found by the following equation. More detailed equations can be found in Reference [21].

$$B = \frac{M}{R^3} \begin{bmatrix} \cos \mu_m \\ 0 \\ 2 \sin \mu_m \end{bmatrix} \quad (\text{A.49})$$

where  $M$  is the Magnetic dipolar moment ( $7.9577 * 10^{15}$ ),  $\mu_m$  is the magnetic latitude and  $R$  is the radial coordinate ( $6971.2 * 10^3$ ).

## A.5 Some Facts About Tetrahedral Configuration

The general figure of the tetrahedral configuration is shown in Figure A.2.

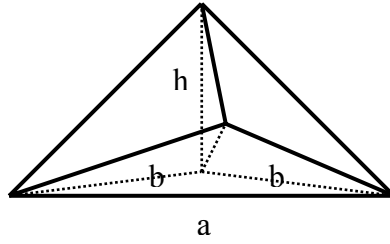


**Figure A.2 :** Tetrahedral Configuration.

The angle between reaction wheels can be calculated using the model given in Figure A.2. By using cosine theorem, the relationship between a and b sides can be derived as,

$$a^2 = b^2 + b^2 - 2b^2 \cos(120^\circ) \quad (\text{A.50})$$

Then,

$$a^2 = 2b^2 \left(1 + \frac{1}{2}\right) \Rightarrow b = \frac{a}{\sqrt{3}} \quad (\text{A.51})$$

Also,

$$h^2 + b^2 = a^2 \Rightarrow h^2 = a^2 - \frac{a^2}{3} \Rightarrow h = a\sqrt{\frac{2}{3}} \quad (\text{A.52})$$

Figure A.3 simply shows the geometric relationship between the angle  $\varphi$ , angle between reaction wheels, and the sides of the tetrahedral configuration.

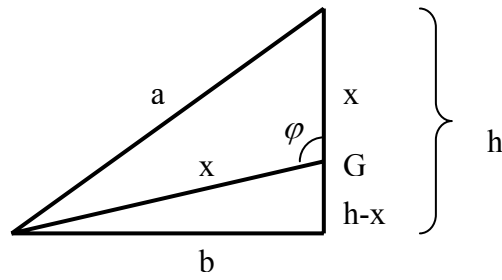


**Figure A.3:** Geometric Relationship Between the Angle  $\varphi$  and the Sides.

According to Figure A.3, following equations are derived.

$$x^2 = b^2 + (h - x)^2 \quad (\text{A.53})$$

Then,

$$x = \frac{b^2 + h^2}{2h} \quad (\text{A.54})$$

By applying Equations A.51 and A.52 to A.54, x can be found as,

$$x = \frac{\frac{a^2}{3} + 2\frac{a^2}{3}}{2a\sqrt{\frac{2}{3}}} \Rightarrow x = a\sqrt{\frac{3}{8}} \quad (\text{A.55})$$

Figure A.4 shows the geometric relationship between sides a and x.

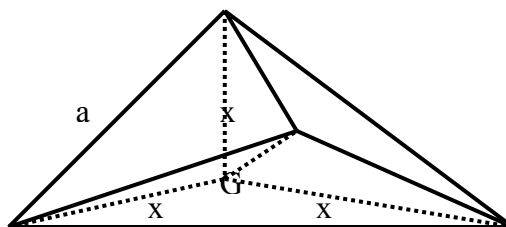


**Figure A.4 :** Geometric Relationship Between Sides a and x.

Again applying cosine law to Figure A.4, one obtains,

$$x^2 + x^2 - 2x^2 \cos \varphi = a^2 \quad (\text{A.56})$$

By applying Equation A.55 to Equation A.56, the angle  $\varphi$  is found as,

$$\cos \varphi = -\frac{1}{3} \Rightarrow \varphi = \cos^{-1}\left(-\frac{1}{3}\right) \Rightarrow \varphi = 109.47^\circ \quad (\text{A.57})$$

As stated before, T given in Equation A.58 stands for the tetrahedral configuration allocation matrix in the design.

$$T = \begin{bmatrix} 0 & 0 & \frac{1}{3}\sqrt{6} & -\frac{1}{3}\sqrt{6} \\ 0 & -\frac{2}{3}\sqrt{2} & \frac{1}{3}\sqrt{2} & \frac{1}{3}\sqrt{2} \\ -1 & \frac{1}{3} & \frac{1}{3} & \frac{1}{3} \end{bmatrix} \quad (\text{A.58})$$

The torques produced by four wheels are converted to torques in three reference axes by T. Tetrahedral configuration of reaction wheels is usually preferred for the following reasons: First of all, four reaction wheeled structure provides an accurate control of the three axis in case of failure of one of the reaction wheels on any axis. Let us denote the torques produced by four reaction wheels as  $T_1, T_2, T_3, T_4$  and the resulting torques produced in three axes by  $T_x, T_y$  and  $T_z$ . Let A be the maximum torque value produced by any reaction wheel. If the torque produced by the fourth reaction wheel is considered to be zero, the torque produced by the third reaction wheel is considered to be A, the torque produced by the second wheel is taken as  $-0.365A$  and the torque produced by the first wheel is selected as  $-0.604 A$ , then,

$$\begin{bmatrix} T_x \\ T_y \\ T_z \end{bmatrix} = \begin{bmatrix} 0 & 0 & \frac{1}{3}\sqrt{6} & -\frac{1}{3}\sqrt{6} \\ 0 & -\frac{2}{3}\sqrt{2} & \frac{1}{3}\sqrt{2} & \frac{1}{3}\sqrt{2} \\ -1 & \frac{1}{3} & \frac{1}{3} & \frac{1}{3} \end{bmatrix} \begin{bmatrix} T_1 \\ T_2 \\ T_3 \\ T_4 \end{bmatrix} \quad (\text{A.59})$$

Equation A.59 becomes,

$$\begin{bmatrix} 0.816A \\ 0.816A \\ 0.816A \end{bmatrix} = \begin{bmatrix} 0 & 0 & \frac{1}{3}\sqrt{6} & -\frac{1}{3}\sqrt{6} \\ 0 & -\frac{2}{3}\sqrt{2} & \frac{1}{3}\sqrt{2} & \frac{1}{3}\sqrt{2} \\ -1 & \frac{1}{3} & \frac{1}{3} & \frac{1}{3} \end{bmatrix} \begin{bmatrix} -0.604A \\ -0.365A \\ A \\ 0 \end{bmatrix} \quad (\text{A.60})$$

The other advantage of this configuration comes from the geometry of the location of the angular momentum vectors. That's, it is possible to obtain twice as much as torque in one axis with this configuration. For example, if the torques produced by the fourth, the third and the second wheel are taken as A, and the torque produced by the first wheel is selected as -A, then Equation A.59 becomes,

$$\begin{bmatrix} 0 \\ 0 \\ 2A \end{bmatrix} = \begin{bmatrix} 0 & 0 & \frac{1}{3}\sqrt{6} & -\frac{1}{3}\sqrt{6} \\ 0 & -\frac{2}{3}\sqrt{2} & \frac{1}{3}\sqrt{2} & \frac{1}{3}\sqrt{2} \\ -1 & \frac{1}{3} & \frac{1}{3} & \frac{1}{3} \end{bmatrix} \begin{bmatrix} -A \\ A \\ A \\ A \end{bmatrix} \quad (\text{A.60})$$

Also, it's possible to prove that the net torque on three axis will be zero if all the reaction wheels produce same amount of torque, A, as seen from Equation A.61.

$$\begin{bmatrix} 0 \\ 0 \\ 0 \end{bmatrix} = \begin{bmatrix} 0 & 0 & \frac{1}{3}\sqrt{6} & -\frac{1}{3}\sqrt{6} \\ 0 & -\frac{2}{3}\sqrt{2} & \frac{1}{3}\sqrt{2} & \frac{1}{3}\sqrt{2} \\ -1 & \frac{1}{3} & \frac{1}{3} & \frac{1}{3} \end{bmatrix} \begin{bmatrix} A \\ A \\ A \\ A \end{bmatrix} \quad (\text{A.61})$$

## A.6 Conversions Between Unit Quaternions and Euler Angles

Rotations in three dimensions can be represented using both Euler angles and unit quaternions. A unit quaternion can be described as:

$$q = [q_0 \quad q_1 \quad q_2 \quad q_3]^T \quad (\text{A.62})$$

where,

$$\begin{aligned} q_0 &= \cos(\alpha/2) & ; & & q_1 &= \sin(\alpha/2)\cos(\beta_x) \\ q_2 &= \sin(\alpha/2)\cos(\beta_y) & ; & & q_3 &= \sin(\alpha/2)\cos(\beta_z) \end{aligned} \quad (\text{A.63})$$

$\alpha$  is a simple rotation angle and  $\beta_x$ ,  $\beta_y$ ,  $\beta_z$  are the direction of cosines locating the axis of rotation.

The orthogonal matrix corresponding to a rotation by the unit quaternion  $q$  is given by

$$\begin{bmatrix} 1 - 2(q_2^2 + q_3^2) & 2(q_1q_2 - q_0q_3) & 2(q_0q_2 + q_1q_3) \\ 2(q_1q_2 + q_0q_3) & 1 - 2(q_1^2 + q_3^2) & 2(q_2q_3 - q_0q_1) \\ 2(q_1q_3 - q_0q_2) & 2(q_0q_1 + q_2q_3) & 1 - 2(q_1^2 + q_2^2) \end{bmatrix} \quad (\text{A.64})$$

The orthogonal matrix corresponding to a rotation with Euler angles is given by

$$\begin{bmatrix} \cos\theta \cos\psi & -\cos\phi \sin\psi + \sin\phi \sin\theta \cos\psi & \sin\phi \sin\psi + \cos\phi \sin\theta \cos\psi \\ \cos\theta \sin\psi & \cos\phi \cos\psi + \sin\phi \sin\theta \sin\psi & -\sin\phi \cos\psi + \cos\phi \sin\theta \sin\psi \\ -\sin\theta & \sin\phi \cos\theta & \cos\phi \cos\theta \end{bmatrix} \quad (\text{A.65})$$

By comparing the terms in the two matrices, we get

$$q = \begin{bmatrix} \cos(\frac{\phi}{2}) \cos(\frac{\theta}{2}) \cos(\frac{\psi}{2}) + \sin(\frac{\phi}{2}) \sin(\frac{\theta}{2}) \sin(\frac{\psi}{2}) \\ \sin(\frac{\phi}{2}) \cos(\frac{\theta}{2}) \cos(\frac{\psi}{2}) - \cos(\frac{\phi}{2}) \sin(\frac{\theta}{2}) \sin(\frac{\psi}{2}) \\ \cos(\frac{\phi}{2}) \sin(\frac{\theta}{2}) \cos(\frac{\psi}{2}) + \sin(\frac{\phi}{2}) \cos(\frac{\theta}{2}) \sin(\frac{\psi}{2}) \\ \cos(\frac{\phi}{2}) \cos(\frac{\theta}{2}) \sin(\frac{\psi}{2}) - \sin(\frac{\phi}{2}) \sin(\frac{\theta}{2}) \cos(\frac{\psi}{2}) \end{bmatrix} \quad (\text{A.66})$$

For Euler angles we obtain:

$$\begin{bmatrix} \phi \\ \theta \\ \psi \end{bmatrix} = \begin{bmatrix} \arctan \frac{2(q_0 q_1 + q_2 q_3)}{1 - 2(q_1^2 + q_2^2)} \\ \arcsin(2(q_0 q_2 - q_3 q_1)) \\ \arctan \frac{2(q_0 q_3 + q_1 q_2)}{1 - 2(q_2^2 + q_3^2)} \end{bmatrix} \quad (\text{A.67})$$

## **APPENDIX B**

### **DATASHEETS OF SOME OF THE BILSAT-1'S ADCS COMPONENTS**

In this section, data sheets of the SSTL 2 axis sun sensor, Altair-Hb star tracker, SSTL 3-axis fluxgate magnetometer, minisatellite reaction wheel and SSTL-Weitzmann 6 m. deployable boom are given in the next pages. All the information given in Appendix B can be found in web page, [www.sstl.uk.co](http://www.sstl.uk.co).

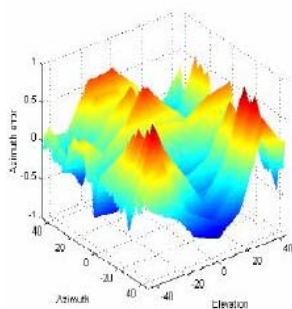
# 2-Axis Sun Sensor



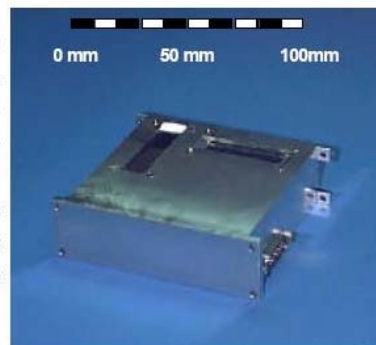
The SSSL 2-axis Sun sensor is a low-cost attitude determination sensor suitable for a wide range of space missions. The sensor measures the sun angle in two orthogonal axes.

The Sun sensor measures the sun angle in both azimuth and elevation. A custom made solar cell detector and small slit is used for each measurement axis. The output from each axis consists of 3 analogue 0 - 5 Volt signals (A, B, C) which can easily be combined and linearised using a calibration polynomial function to obtain the relevant sun angles. The third analogue signal comes from a temperature sensor within the unit.

SSSL has been producing Sun sensors since UoSAT-3 and has accumulated over 63 orbit-years experience in the field. The latest evolution was flight qualified on FASAT-Bravo, launched in 1998.



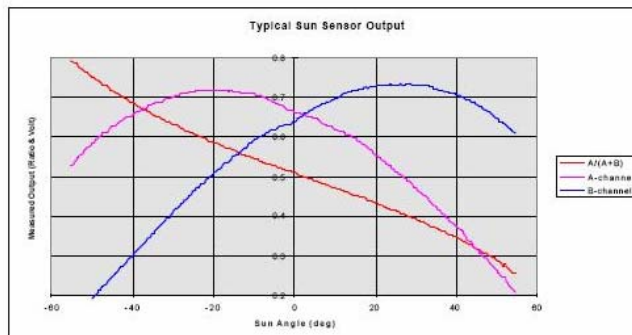
Errors in azimuth and elevation following calibration



Bare sun sensor unit, can be supplied with a variety of applied thermal surfaces

## Sun Sensor Features

- **Low cost** parts and construction inherent to design
- **Low power, volume, mass** for easy integration on any platform
- **Testing and PA** plans available. Adaptable Environmental Testing, Acceptance Testing and PA plans



## Other SSSL Products

- **ADCS equipment** including: star trackers; 3-axis quartz rate gyros; magnetometers; magnetorquers; reaction/momentum wheels.
- **Complete low cost small satellite solutions**, based on SSSL range of nano, micro, enhanced micro and mini satellites, including know-how transfer and rapid and affordable access to space
- **Sub-systems** (CD&H, Power, Communications, ODCS) and various **payloads**

affordable access to space

## Specifications

- Sensors: 2 orthogonal axes
- Sensor Field of View: +/- 50°
- Accuracy: 0.5° (3σ)
- Analogue output: 6 x 5 V channels

## Environmental (Acceptance Level)

- Random Vibration: 15 g rms
- Operating Temp.: -50°C to +80°C
- Cumulative radiation dose: 20 kRad
- EMC: as per MIL-STD-462

## Physical Characteristics

- Dimensions: 95x107x35 mm
- Mounting Interface: Flat
- 4 x M3 clearance holes
- Mass: 0.30 kg

## Power Supply

- Power Consumption: Sunlit: <100 mW; Dark: <1 mW
- Power Supply: +/- 12 V

## Contact



**Surrey Space Centre**  
University of Surrey  
Guildford, Surrey GU2 7XH  
United Kingdom

Tel: (44) 1483 259278  
Fax: (44) 1483 259503  
E-mail: [ssstl@sstl.co.uk](mailto:ssstl@sstl.co.uk)  
www: [www.sstl.co.uk](http://www.sstl.co.uk)

## Issue Number & Notice

SSSTL-9004-02. 21-06-2000. This data sheet is for preliminary information purposes and can be changed without any notice. Please contact SSSL (see above) for further information.

# Altair-HB Star Tracker



The SSTL Altair-HB Star Tracker is a low cost, wide field of view unit capable of providing reliable attitude determination to demanding missions. It is part of the SSTL control systems sensor range. SSTL star trackers have been employed on a number of missions previously and the design of this star tracker draws on that heritage.

SSTL Star Trackers have been previously flown on the PoSat and UoSat-12 missions.

The Altair-HB will have its inaugural flight on the BilSat mission for Tubitek in Turkey, in 2003 (TBC). Two Altair-HBs are used on BilSat to meet the demanding pointing requirements of that mission while keeping the mission affordable.

The Altair-HB connects to the OBDH via a CAN bus, but can be modified to support RS 232 or RS 422/485. The Altair-HB output data consists of pairs of matching measurement and star catalogue reference vectors. These can then be supplied at 1 second intervals to the satellite's attitude determination and control system.



Altair-HB



Altair-HB Optical Head

The hardware for the Altair-HB consists of the camera assembly and a processor assembly with all the required interfaces and peripheral circuits to interface with an AOCS or other controller. The processor used on the Altair-HB is a StrongARM SA-1100 with 4 Mbytes of EDAC protected processor RAM. There is also 2 Mbytes of processor Flash RAM and 2 Mbytes of image RAM.

The Altair-HB will track up to 15 stars at one time and has a matching success rate of 99.8 %.

The Altair-HB will track up to 15 stars at one time and has a matching success rate of 99.8 %. The maximum tracking rate is 0.5 %/s - below that rate with suitable filtering it will provide an excellent rate estimate. On BilSat a dynamic filtering scheme will be used to improve the attitude estimates by almost an order of magnitude.



Altair-HB Processor Board

#### Other AODCS products:

##### Actuators:

- ✓ Reaction Wheels
- ✓ Momentum Wheels
- ✓ Magnetorquer Rods
- ✓ Control Moment Gyros
- ✓ Gravity Gradient Booms

##### Sensors:

- ✓ Fine Sun Sensors
- ✓ Magnetometers

#### Applications

- Satellite attitude determination

#### Specifications

- Field of view: 15.74° x 10.53°
- Pointing accuracy (1  $\sigma$ ):
  - Normal to boresight: 15 arcsec
  - Around boresight: 50 arcsec
- Sensitivity: Down to mag 6.0
- Operating bandwidth: 1 Hz
- Exclusion angles:
  - Sun: 40°
  - Earth: 30°
- Max tracking rate: 0.5 %/s

#### Mechanical / Power

- Mass: 1.8 kg (including baffle)
- Size: 144 x 144 x 280 mm (including baffle)
- Power Supply: 16-50 V<sub>DC</sub>
- Power: 2.8 W (@ 28 V) average
- Temperature: -20 to +50°C

#### Contact



**Surrey Space Centre**  
University of Surrey  
Guildford, Surrey GU2 7XH  
United Kingdom

Tel: +44 (0)1483 689278  
Fax: +44 (0)1483 689503  
E-mail: [info@sstl.co.uk](mailto:info@sstl.co.uk)  
www: [www.sstl.co.uk](http://www.sstl.co.uk)

#### Issue Number & Notice

ISSUE-9033-1. 31-07-2002. This data sheet is not contractual and can be changed without any notice. Please contact SSTL (see above) for further information.

affordable access to space

# 3-axis Fluxgate Magnetometer



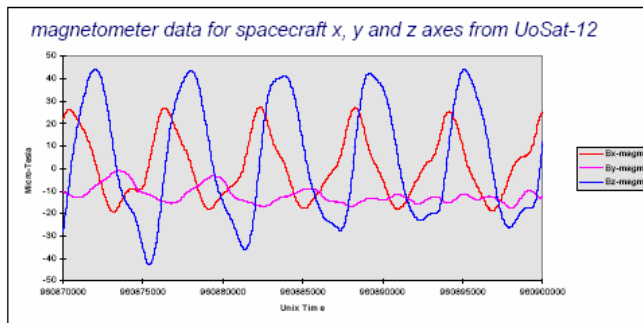
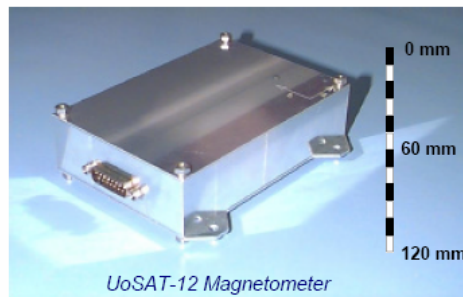
The magnetometer is suitable for wide range of missions in LEO. It is housed in a compact unit and provides analogue readings on the magnetic field from three sensors in orthogonal axes. It has been qualified over numerous missions.

The magnetic field encountered by the satellite is measured by the 3-axis fluxgate magnetometer. The magnetometer returns data via three analogue (0 to 5 V) lines, one for each axis of measurement. Additionally, an analogue (0 to 5 V) temperature sensor provides case temperature for telemetry.

A total of 40 SSTL magnetometers are employed on 14 satellites in orbit with an accumulated well over a 100 orbit-years of operation. The unit has a reliability figure of 0.984 for a three year LEO mission.

SSTL has developed a miniature version based on similar electronics. The unit's mass and dimensions will be in the region of 94 g and 85 x 35 x 32 mm, with similar performance specifications to this existing unit (a datasheet is already available). The first unit will fly on the UKDMC mid-2003, with another unit supplied for TopSat.

- **Low cost** product
- **Low power, volume, mass** for easy integration on any platform
- **Testing and PA** plans available. Adaptable Environmental Testing, Acceptance Testing and PA plans



## Other SSTL Products

- **ADCS equipment** including: sun sensors, star trackers; 3-axis quartz rate gyros; magnetometers; magnetorquers; reaction and momentum wheels.
- **Sub-systems** (C&DH, Power, Communications, RF, propulsion) and various payloads
- **Complete low cost small satellite solutions**, based on SSTL range of nano, micro, enhanced micro and mini satellites, including know-how transfer and rapid and affordable access to space

**affordable access to space**

## Applications

- Spacecraft in LEO

## Specifications

- Sensitivity: -10 to +10 nT
- Range: -60 to +60  $\mu$ T
- Update Rate: 10 Hz maximum

## Environmental

- Random Vibration: 15 g rms
- Operating Temp: -50 to +80 °C
- Cumulative radiation dose: 20 kRad
- EMC: as per MIL-STD-462

## Physical Characteristics

- Dimensions: 130 x 90 x 36 mm
- Mass: 295 g
- Finish: none (options available e.g. Alocrome, black)

## Power Supply

- Power supply:  
8 mA @ -10.5 V  
and  
14 mA @ +10.5 V

## Contact



**Surrey Space Centre**  
University of Surrey  
Guildford, Surrey GU2 7XH  
United Kingdom

Tel: +44 (0)1483 689278  
Fax: +44 (0)1483 689503  
E-mail: [info@sstl.co.uk](mailto:info@sstl.co.uk)  
www: [www.sstl.co.uk](http://www.sstl.co.uk)

## Issue Number & Notice

SSTL-9013-02. 17-03-2003. This data sheet is for preliminary information purposes and can be changed without any notice. Please contact SSTL (see above) for further information.

# Minisatellite Reaction Wheel



The minisatellite reaction wheel is a low cost unit capable of providing reliable attitude control and stabilisation to demanding missions. It is part of the SSSL control systems actuator range. SSSL reaction wheels have been employed on missions with a broad spectrum of requirements from nanosatellites to interplanetary vehicles.

The minisatellite reaction wheels were first flown on UoSAT-12, launched in 1999. The unit has been designed according to SSSL's extremely successful design principle covering twenty small satellite missions. The minisatellite wheel is part of a range of wheels which were first used on TMSat in 1998 and have since featured on the SNAP-1 nanosatellite, various microsatellites and also supplied to ESA for the Rosetta Comet Lander interplanetary mission.

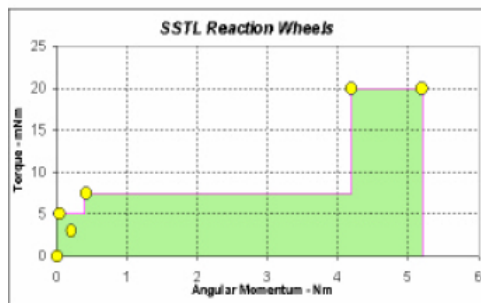


Minisatellite Reaction Wheel

The wheels can be used as reaction or momentum wheels and are run in torque control or speed control modes. They are controlled via a CAN bus, but can be modified to support RS 232 or RS 422/485. The unit provides telemetry on wheel speed, current and PCB temperature via these interfaces.

Missions (number of wheels)	Chronology	Max Wheel Momentum	Max Wheel Torque	Mass	Power – Constant Speed	Power – Max Accel	Power – Zero Speed
FASat-Alpha (1 Wheel) / FASat-Bravo (1)	1995	0.04 Nms	5mNm	0.5 kg	1.2 W		
TM-Sat (1) / Tiungsat-1 (1) / Tsinghua-1 (3)	1997	0.21 Nms	3 mNm	0.75 kg	0.4 W	3 W	0.2 W
UoSAT-12 (2)	1998	4.2 Nms	20 mNm	3.2 kg	3.3 W	14 W	1.5 W
SNAP-1 (1)	1999	0.01 Nms		0.08 kg	0.1 W	0.5 W	<0.1 W
Alsat-1 (2) / UK-DMC (2) / Bilsat (4) / Topsat (4) / NigeriaSat-1 (2)	2001	0.42 Nms	7.5 mNm	1.1 kg	1.2 W	5 W	0.8 W
Rosetta (1)	2001	5.2 Nms	20 mNm	2.6 kg	< 5 W	14 W	N/A

Summary of SSSL reaction wheels to date – Minisatellite Wheel is highlighted



Other AODCS products:

#### Actuators:

- ✓ Reaction Wheels
- ✓ Momentum Wheels
- ✓ Magnetorquer Rods
- ✓ Control Moment Gyros
- ✓ Gravity Gradient Booms

#### Sensors:

- ✓ Fine Sun Sensors
- ✓ Magnetometers

## Applications

- Attitude control for minisatellites

## Specifications

- Max. wheel momentum: 4.2 Nms
- Max. wheel torque: 20 mNm
- Motor torque constant: 0.044 Nm/A
- Wheel MOI: 0.008 kgm<sup>2</sup>
- Max. wheel speed: +/- 5000 rpm
- Speed control: +/- 1 rpm
- Drive motor type: 3-Phase Brushless DC
- Motor drive method: 4-Quadrant PWM current loop

## Mechanical / Power

Mass: 3.2 kg

Size: 190 x 190 x 110 mm

Housing: Aluminium (Dural L93)

Power Supply: 24 - 32 V<sub>DC</sub>

Power:

- 1.5 W at 0 rpm
- 3.3 W at constant speed
- 14 W at max. acceleration

## Contact



### Surrey Space Centre

University of Surrey  
Guildford, Surrey GU2 7XH  
United Kingdom

Tel: +44 (0)1483 689278

Fax: +44 (0)1483 689503

E-mail: [info@sstl.co.uk](mailto:info@sstl.co.uk)

www: [www.sstl.co.uk](http://www.sstl.co.uk)

## Issue Number & Notice

ISSUE-9017-1. 31-07-2002. This data sheet is not contractual and can be changed without any notice. Please contact SSSL (see above) for further information.

affordable access to space

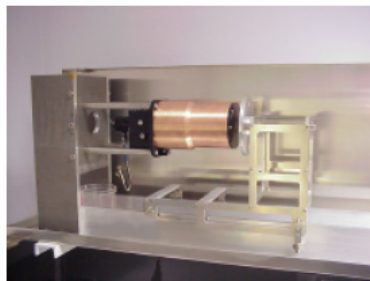
# SSTL-Weitzmann 6m Deployable Boom



The SSTL-Weitzmann boom is a compact system for deploying payloads or instruments, or to form the basis of a gravity gradient attitude system, on a 6 metre rigid boom. The STACER tube, on which it is based, has a heritage of over 25 years, during which more than 600 units have been used on a variety of spacecraft and sounding rockets.

The SSTL-Weitzmann boom is a deployable boom system capable of extending a tip mass or payload by up to 6 metres. It is typically used to provide spatial distance between sensors and their platform (spacecraft or sounding rockets) or with a tip mass on gravity gradient stabilised satellites.

The system is extremely compact when stowed (102 x 115 x 264 mm) and lightweight (2.2 kg), making it ideally suited for small satellite missions where volume and mass are at a premium. Deployment is initiated by applying power to dual redundant pyro-cutters which release the STACER mechanism. A deployment switch is toggled as the boom extends, where the number of transitions indicates the deployed length.



During deployment the STACER forms one coil at a time, thus at the end of deployment a fully tubular structure is in place, with a good level of overlap between adjacent coils. Once deployed, the boom is a very rigid structure, with similar behaviour to a thin walled tube. In comparison to longitudinally 'split tape' type booms the SSTL-Weitzmann boom exhibits uniform cantilever bending stiffness and significantly improved torsion and thermal characteristics.

The boom has an extensive heritage, dating back for over 25 years, during which over 600 STACER units have been used on a variety of sounding rocket and spacecraft missions. As well as producing the SSTL-Weitzmann booms, SSTL extensive and valuable experience in their integration and operation on spacecraft which can be passed on to users of the boom - so far 9 SSTL spacecraft have already successfully deployed such booms.



## Features

- **Flexible payload** accommodation
- Available as a complete **gravity gradient system** with tip mass
- **Low cost, short lead time** mean the boom is ideally suited for small missions
- **Rigid structure** - the tubular design results in a rigid structure with low thermal deflection
- **Flight proven**- over 600 STACER units sold
- **Non-magnetic** materials used throughout the boom
- **Test & Performance Data** available on request

affordable access to space

## Applications

- Deployable tip mass system for gravity gradient stabilised spacecraft
- One-off deployment use for extended lifetime ADCS
- Aerodynamic stabilisation
- Instrument boom for sensors on spacecraft or sounding rockets are available from Kaleva Design ([www.kalevadesign.com](http://www.kalevadesign.com)).

## Specification

- Maximum deployable distance: 6000 mm +305 / -0 mm
- Stowed volume: 102 x 115 x 264 mm
- Deployed volume: 102 x 115 x 6264 mm
- Mass (excluding tip mass): 2.2kg
- Available tip masses: 1.0 to 13.0 kg
- Deployed flexural stiffness: 3 (tip) to 12 (base) Nm<sup>2</sup>
- Flexible payload accommodation
- Deployment speed controllable, typically 0.3 metres / second
- Available deployment thrust: 17 Newtons
- Switch indicates deployed length

## Qualification / Heritage

- Over 600 STACER units in the last 25 years
- Successfully deployed on these SSTL missions: UoSAT -5, KITSAT-1, S80/T, HealthSat, POSAT, CERISE, FASAT-Bravo, TMSAT, CLEMENTINE
- Selected for UoSAT-12, TiungSat, PICOSat, Tsinghua-1

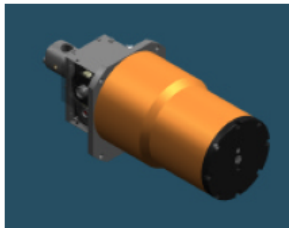
# SSTL-Weitzmann 6m Deployable Boom



## Description

The mechanism consists of two major sub-assemblies, separated by a circular mounting plate. Ahead of the mounting plate (in the deployment direction), the STACER element in its canister is located centrally, surrounded by a spring loaded telescopic section whose purpose it is to reliably initiate the deployment sequence, and to extend the boom support nozzles which provide pointing accuracy and cantilever stiffness.

The canister shaped tip mass is placed coaxially over the telescopic section and is seated in a circumferential recess in the mounting plate. Located aft of the mounting plate is a flyweight brake mechanism which acts through a spool-wound restraint line connected internally to the STACER tip shaft to limit the deployment speed to a desired level. A cam-operated limit switch senses spool rotations and monitors deployment speed an distance.



Deployment is initiated with a pyrotechnic bolt cutter located aft of the brake mechanism. The cutter acts on a shear bolt loaded in tension to the STACER tip shaft which is connected to the tip mass. The resulting compressive load on the tip mass is reacted by the mounting plate interface and thereby holds the tip mass securely. A cap placed over the shear bolt head provides a positive lock on the bolt and also captures the severed bolt head with an energy-absorbing lead slug.

A safety locking screw is provided which secures the tip mass to the mounting plate and thus prevents accidental deployment. To increase reliability, the unit is fitted with a redundant backup cutter.

## Other SSTL Products

- **ADCS** - magnetometers, Sun and Earth sensors, star mappers, quartz rate gyros, wheels, magnetorquers.
- **ODCS** - GPS receivers for orbit and attitude determination, cold gas and resistojet propulsion systems. Hybrid rockets currently in development.
- **Gravity gradient ADCS module** - An ADCS module based on the UoSAT gravity gradient stabilisation well proven low cost system.
- **Complete low cost small satellite solutions**, based on SSTL range of nano, micro, enhanced micro and mini satellites, including technology/know-how transfer and rapid and affordable access to space.
- Complete **spacecraft sub-systems**, unit level equipment and Ground Segments

**affordable access to space**

## Environmental (Acceptance Level)

- Random Vibration: 15 g, 3 axes
- Pressure: atmospheric to hard vacuum
- Radiation: not affected after deployment
- Thermal:
  - <100 °C prior to deployment
  - no requirements once deployed

## Electrical Interface & Pyrotechnics

- Dual redundant pyro-cutters placed in series
- Pyro-cutters classed as "Class C" explosives safe for flight and train travel
- 4-pin connector
- Pyro-cutter actuation:
  - No-fire current: 1.0 A for 1 min.
  - All-fire current: 5 A for >10 msec.

## Contact



**Surrey Space Centre**  
University of Surrey  
Guildford, Surrey GU2 7XH  
United Kingdom

Tel: +44 (0)1483 259278  
Fax: +44 (0)1483 259503  
E-mail: [info@sstl.co.uk](mailto:info@sstl.co.uk)  
www: [www.sstl.co.uk](http://www.sstl.co.uk)

## Issue Number & Notice

SSTL-9007-04. 11-10-2001. This data sheet is not contractual and can be changed without any notice. Please contact SSTL (see above) for further information.

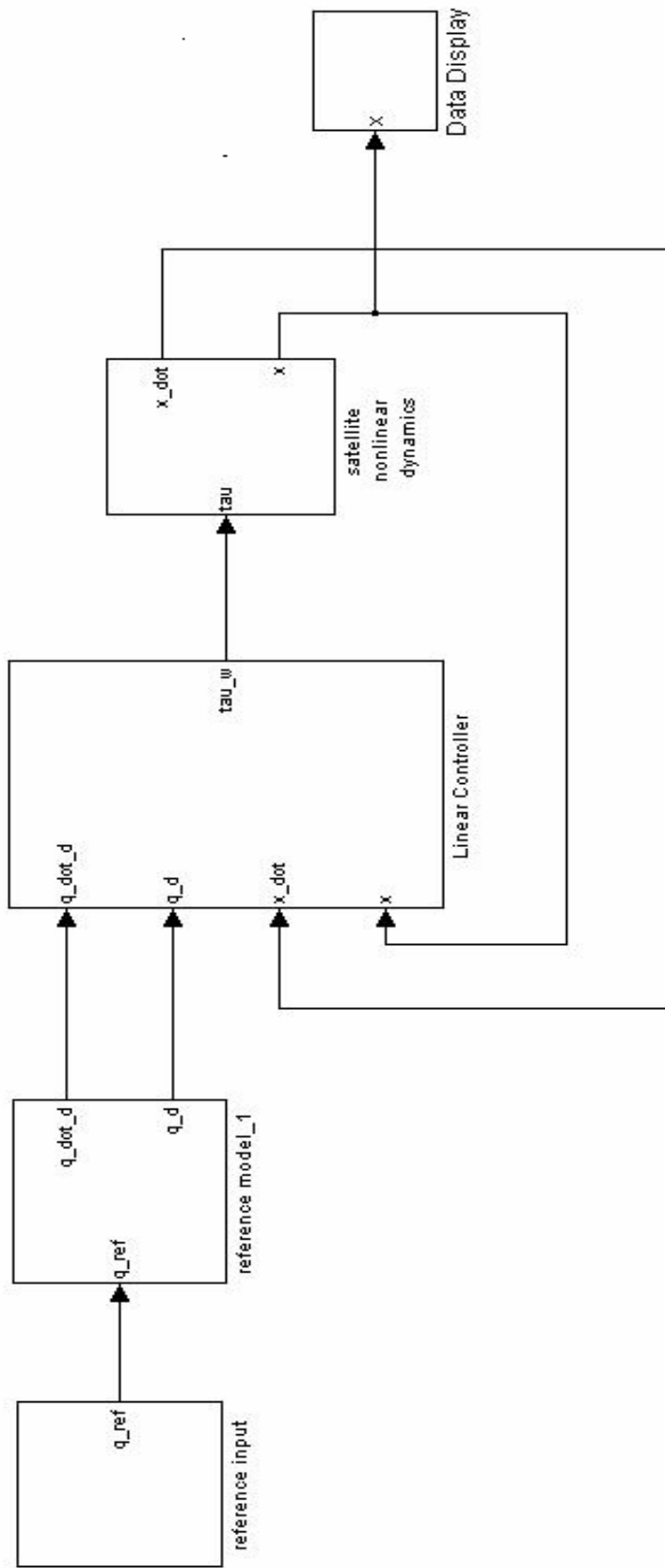
## **APPENDIX C**

### **SIMULINK MODELS AND MATLAB CODES**

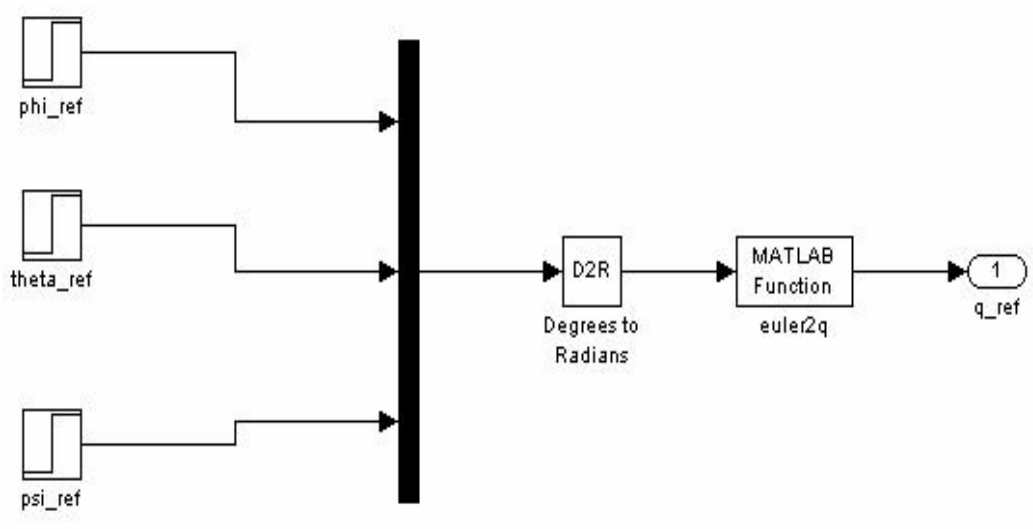
#### **C.1 Simulink Model of the Linear Controller with Reaction Wheels as Actuators**

In this section, MATLAB codes and SIMULINK model of the linear controller with reaction wheels is given on the next pages.

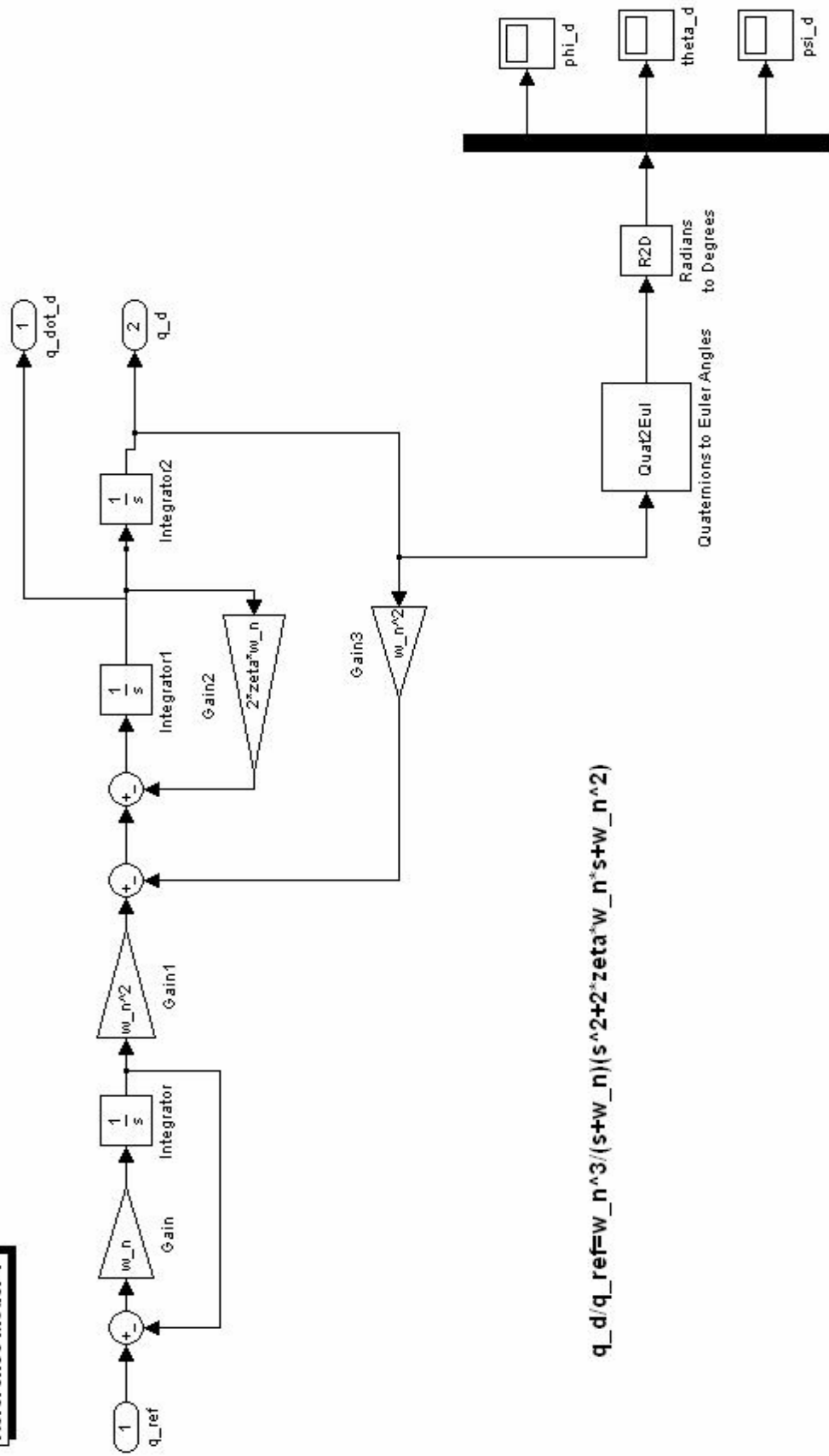
### Satellite Control Model



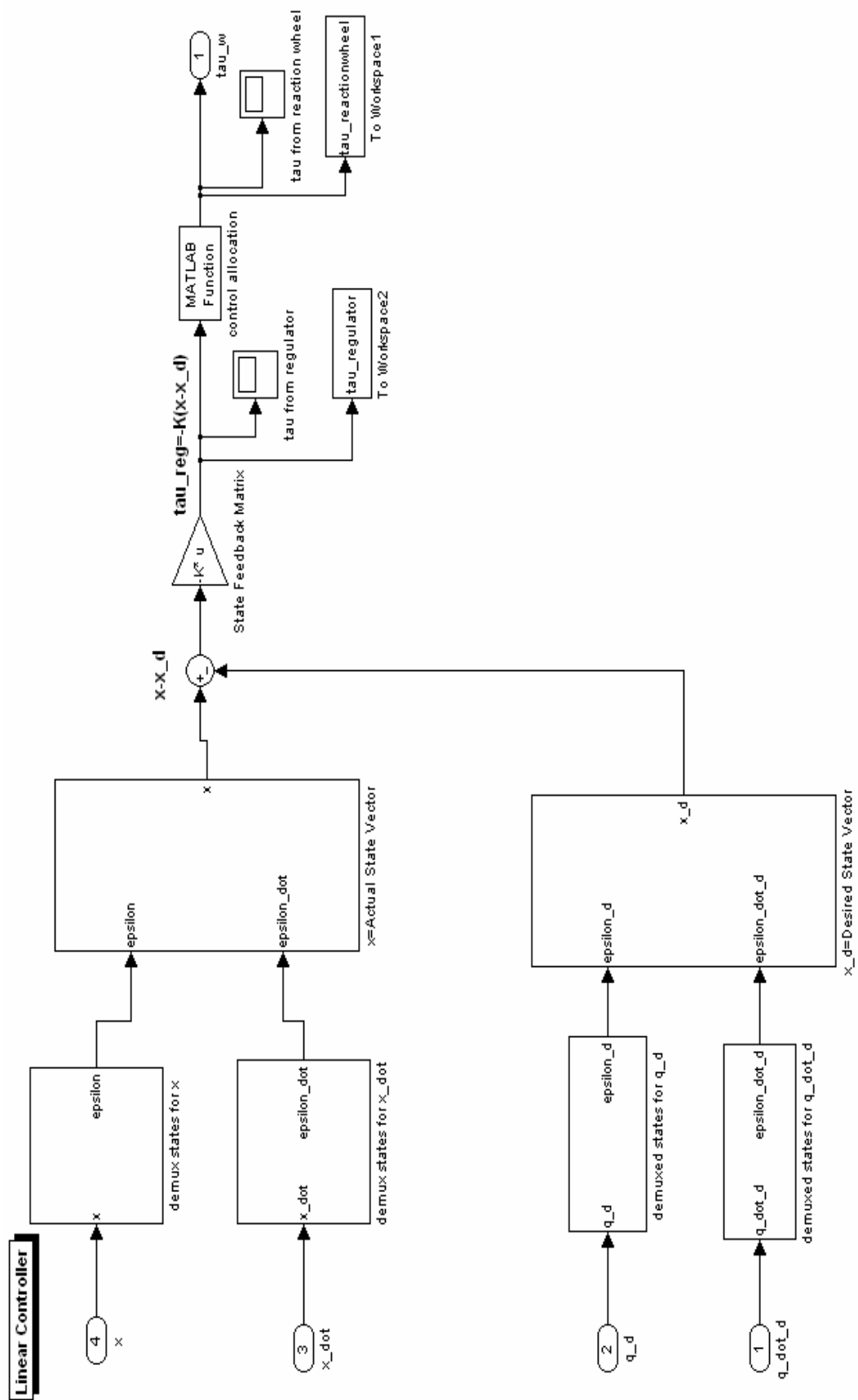
### Reference Input Angles



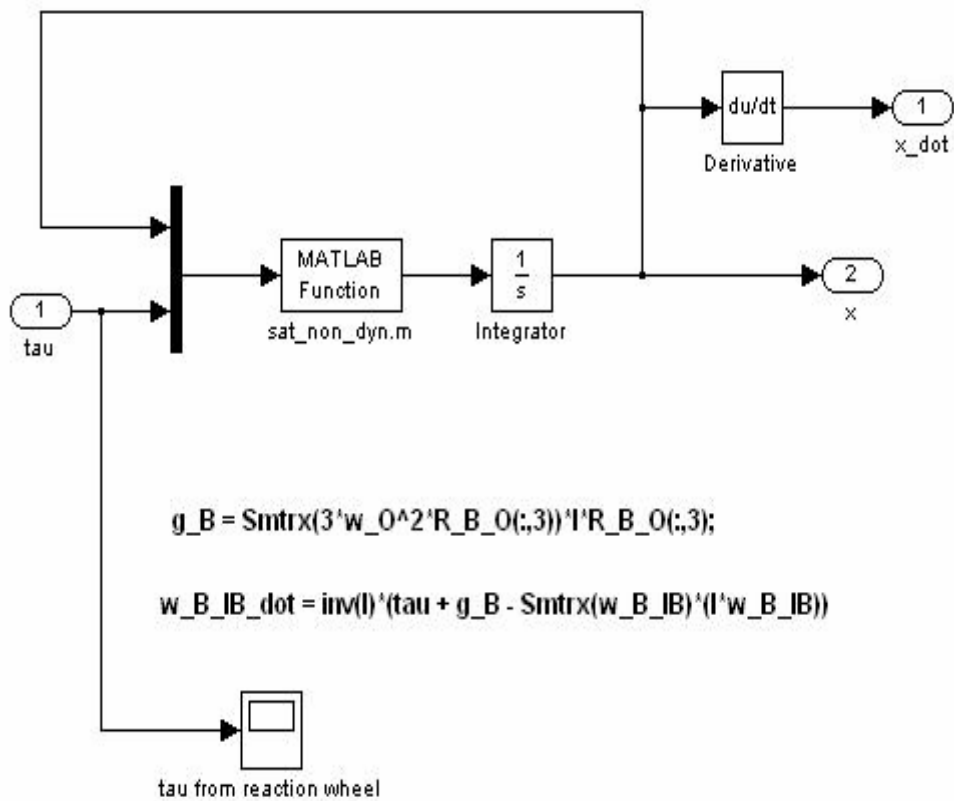
**Reference Model-1**

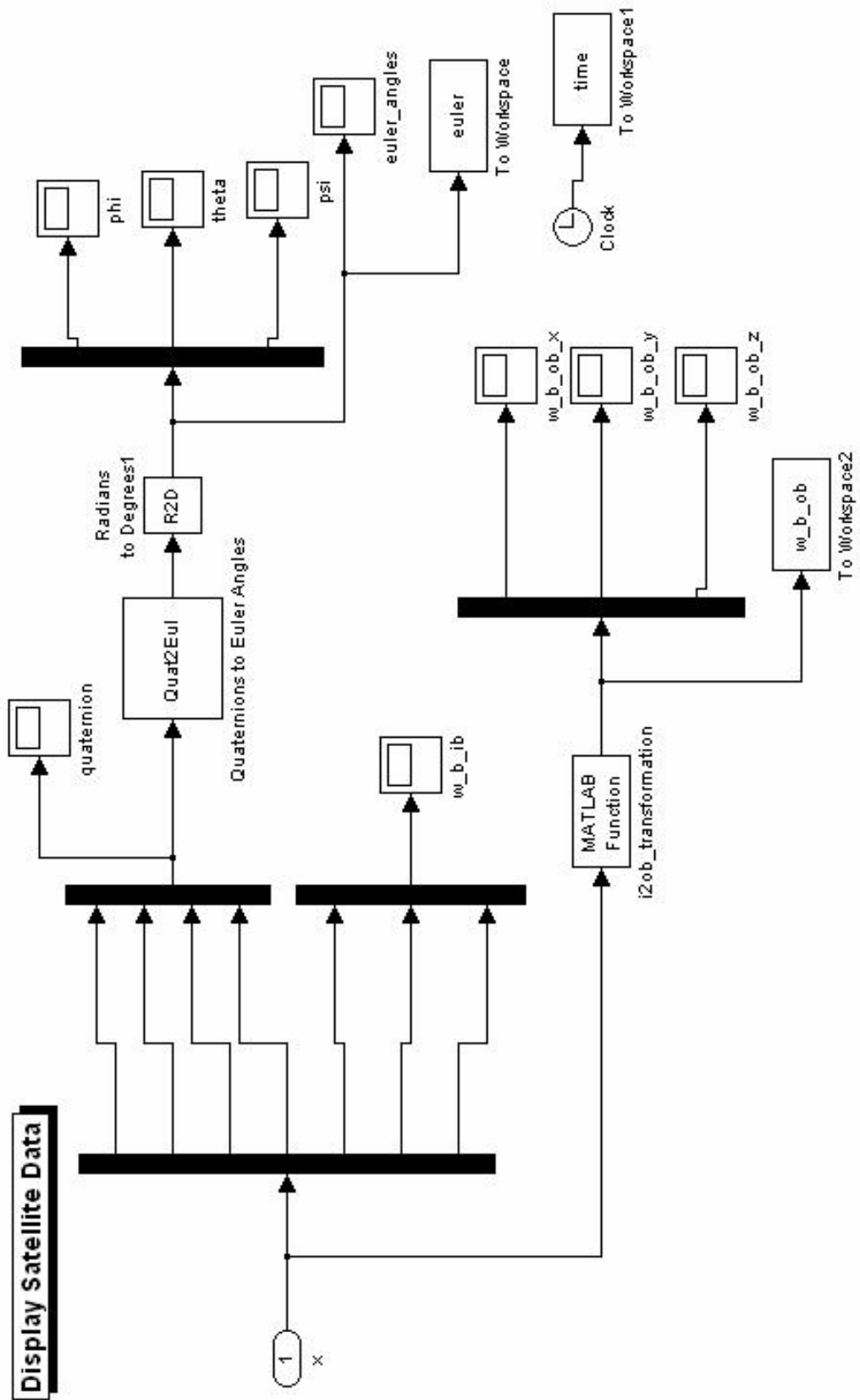


$$q_d/q_{ref} = \omega_n^3 / (s^2 + 2 \cdot \zeta \cdot \omega_n \cdot s + \omega_n^2)$$



## Satellite Nonlinear Dynamic

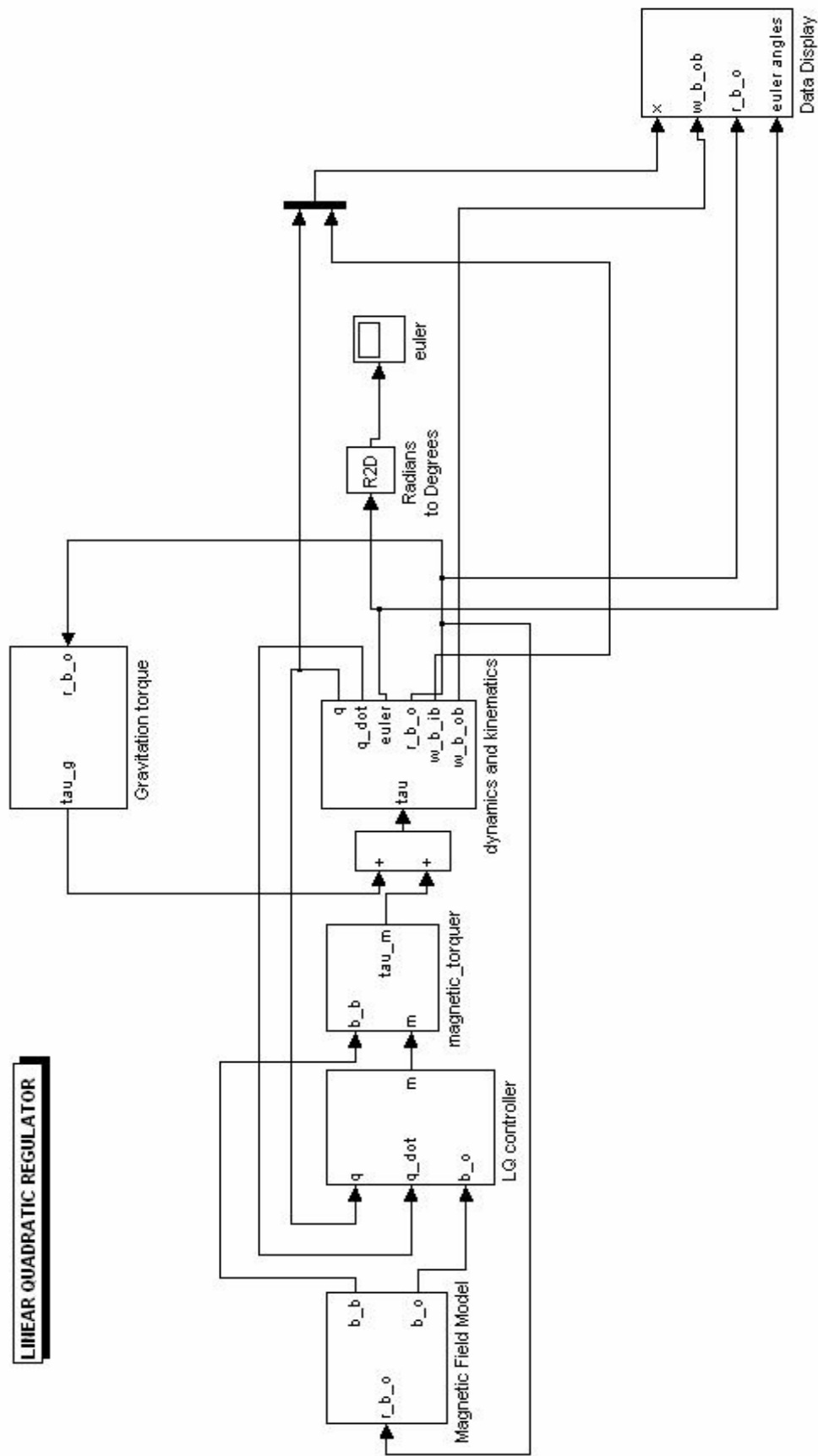




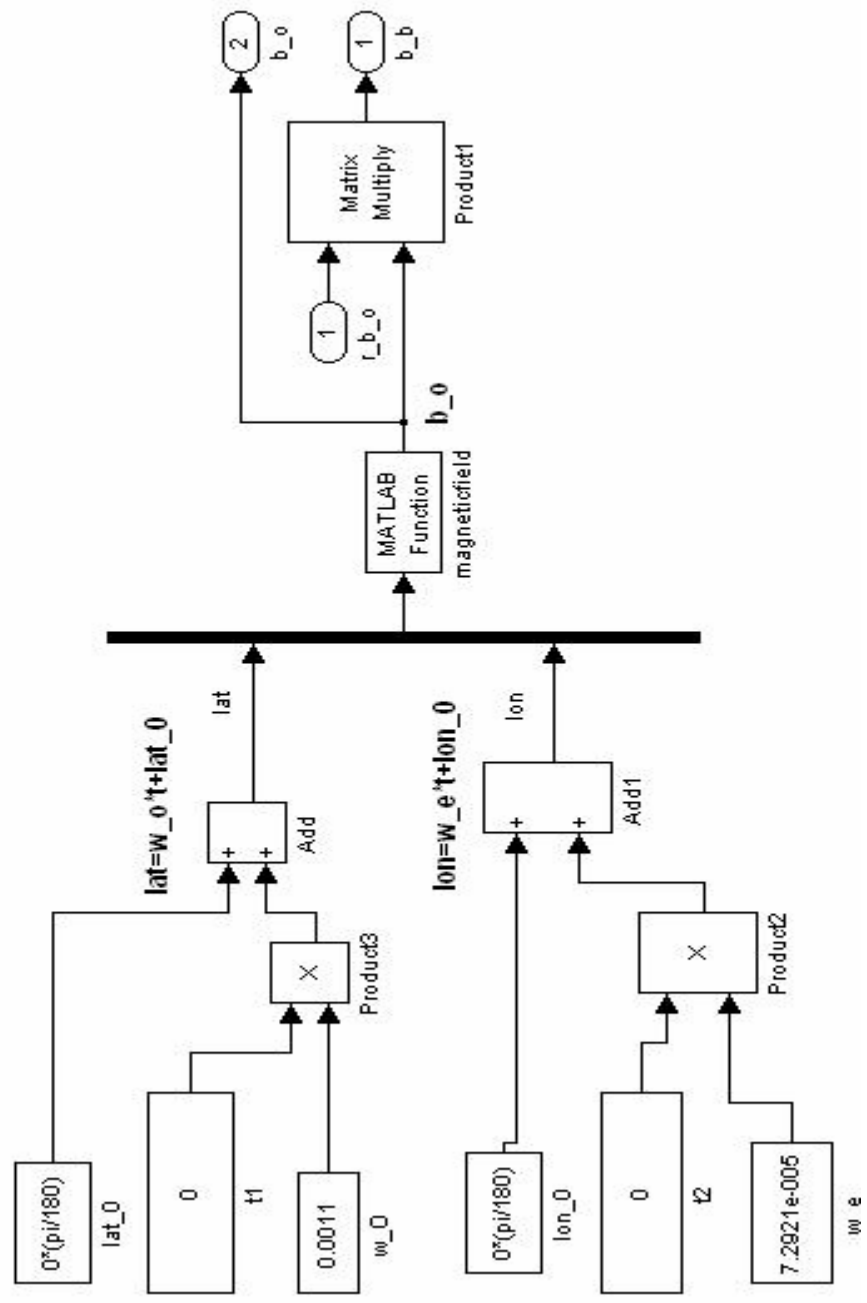
## **C.2 Simulink Model of the Linear Quadratic Regulator with Magnetic Torquers as Actuators**

In below sections, MATLAB codes and SIMULINK model of the linear quadratic regulator with magnetic torquers as actuators are given.

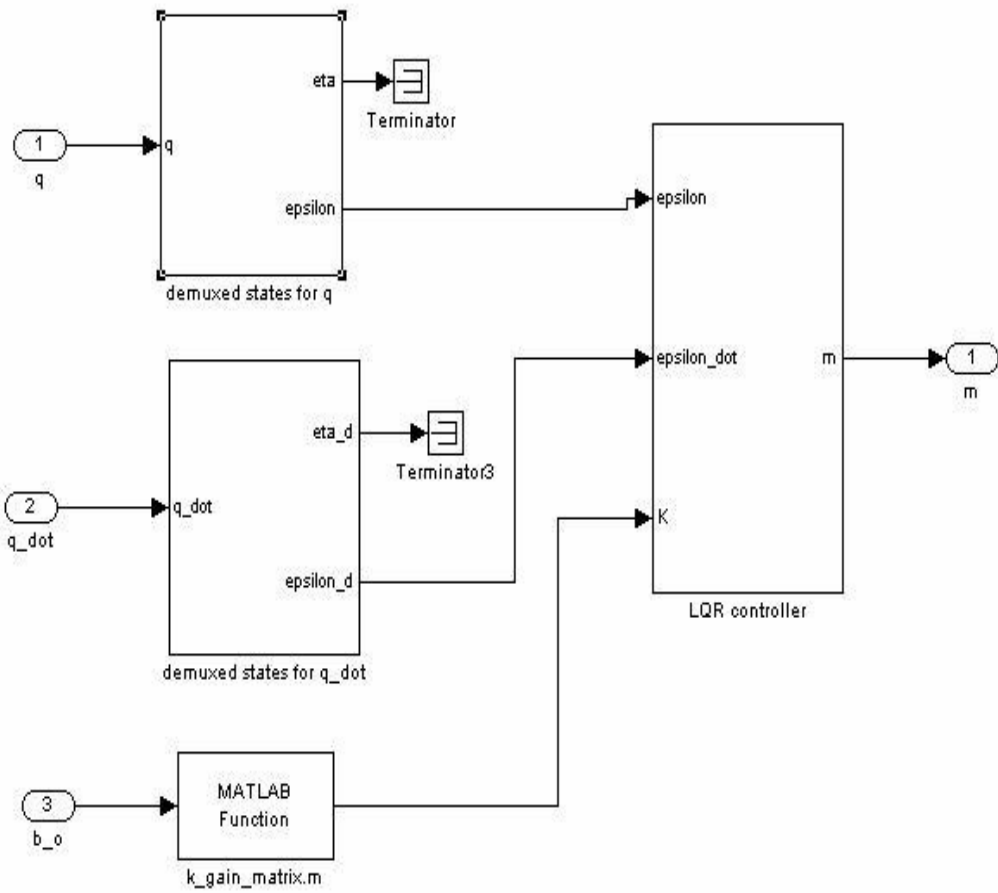
# LINEAR QUADRATIC REGULATOR

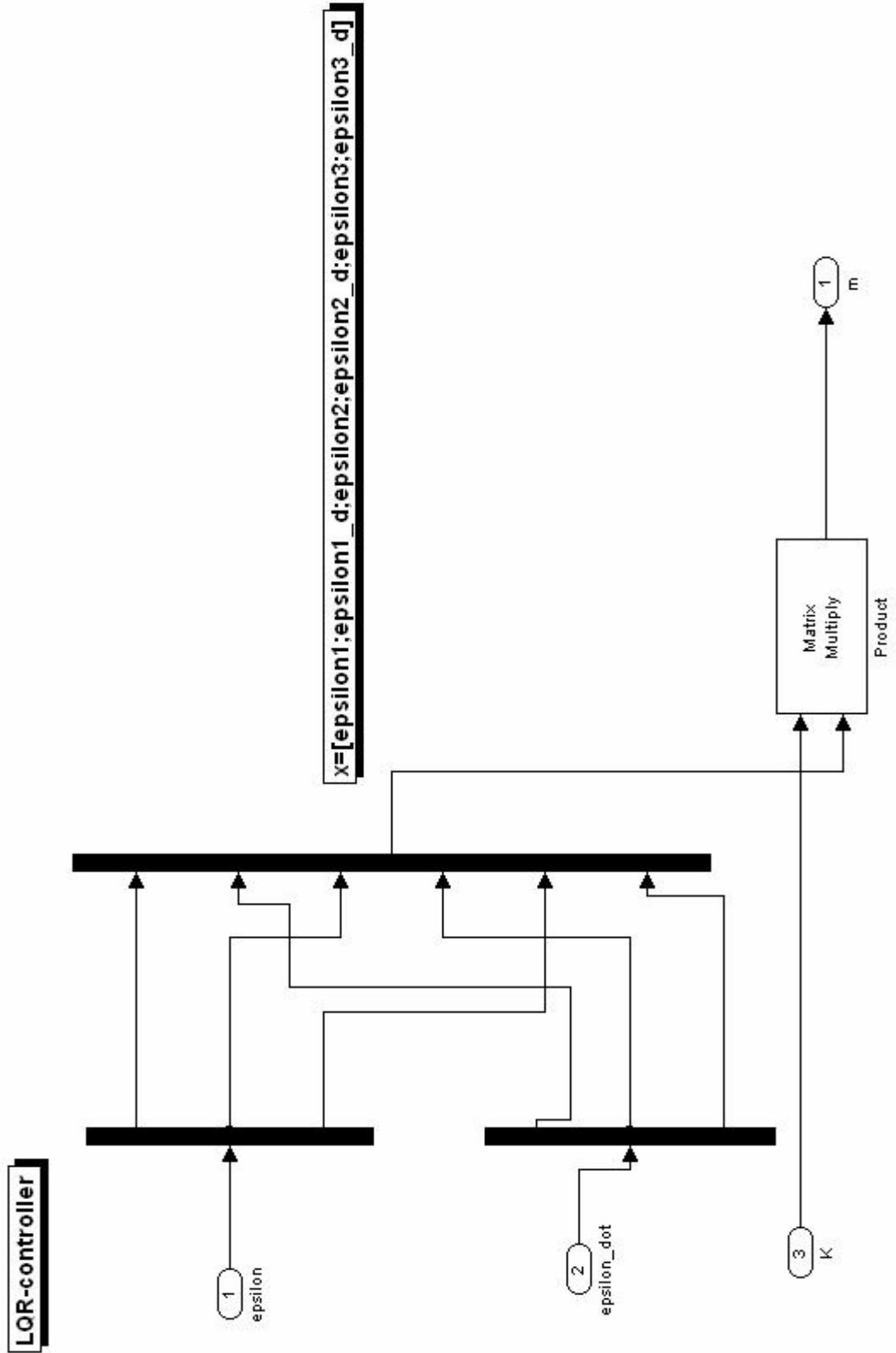


### Magnetic field model

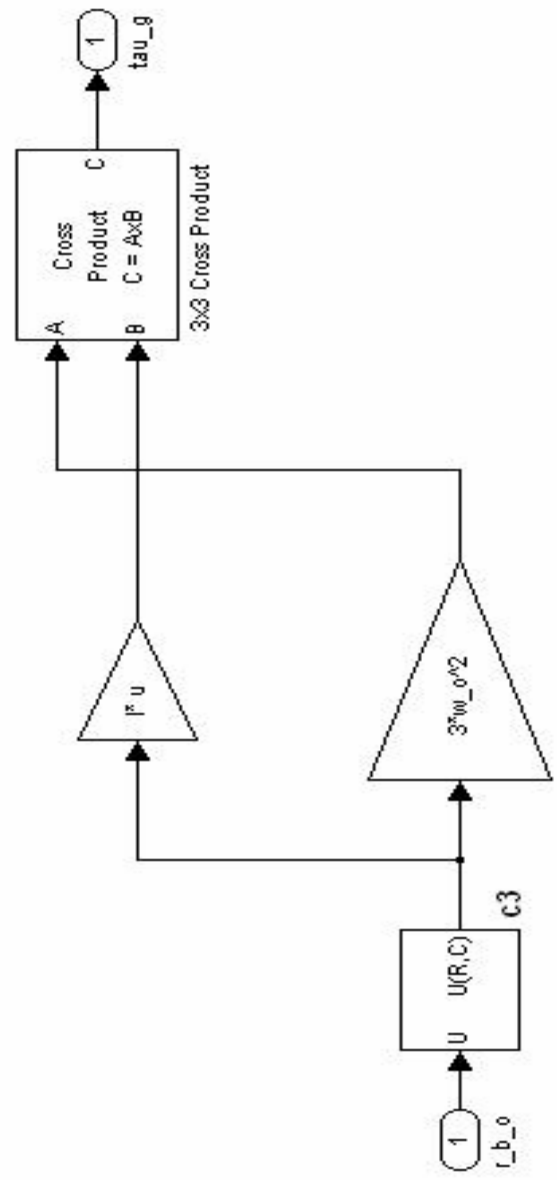


## LQ-controller



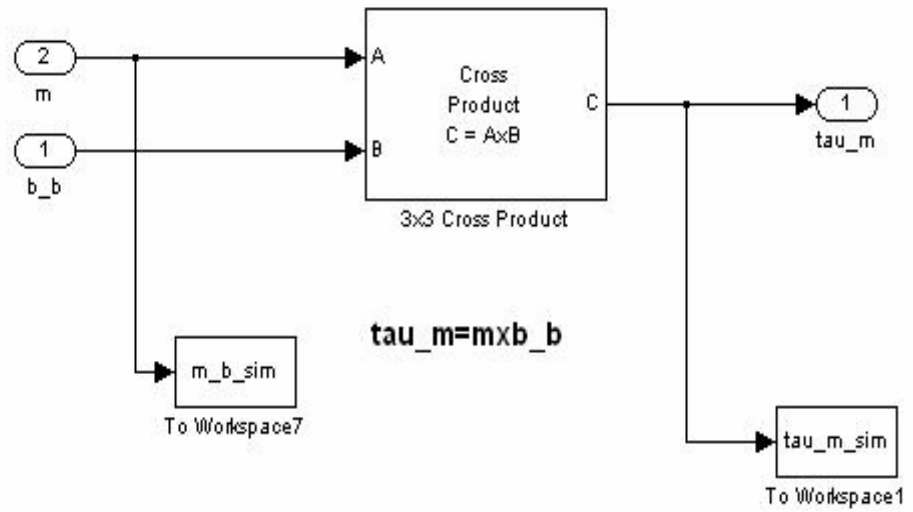


**Gravitation torque**

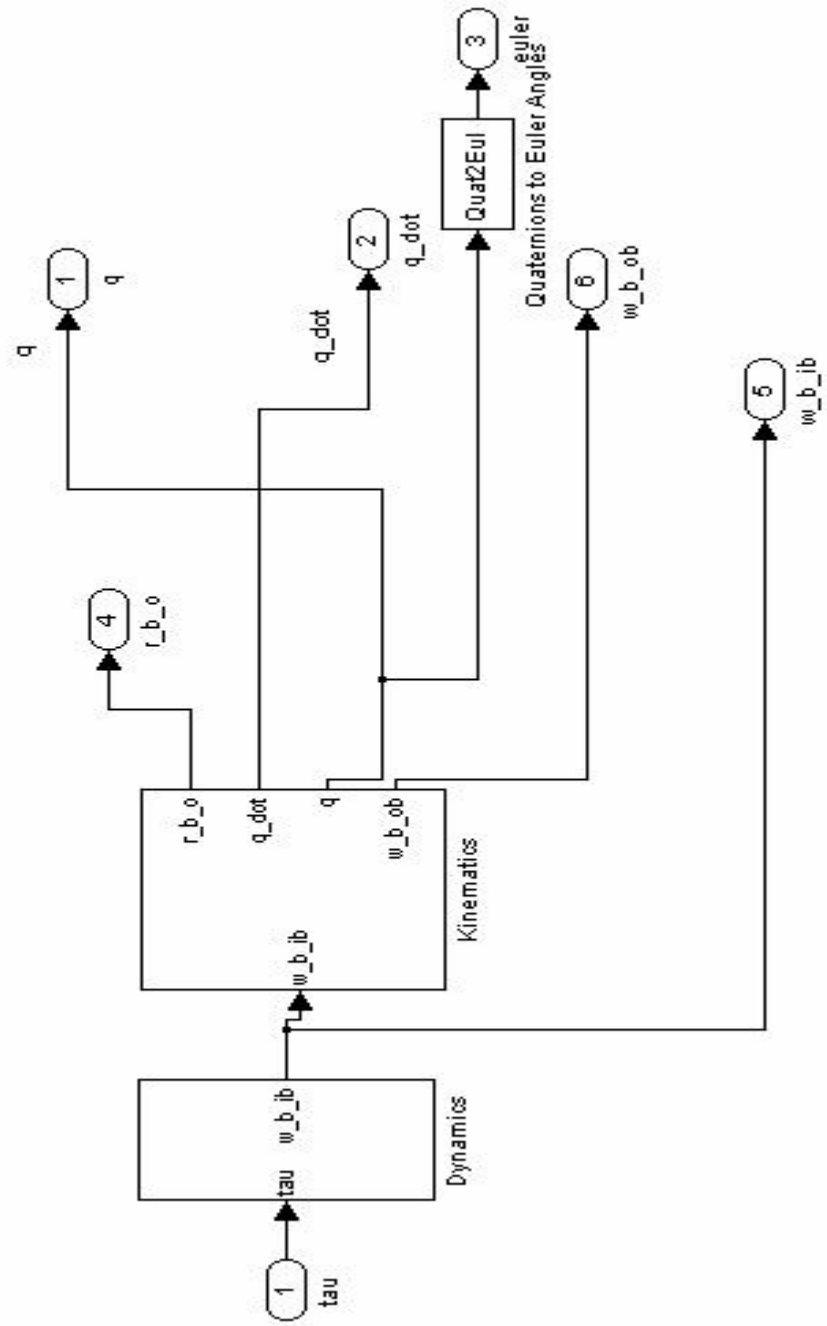


$$\tau_{g_{grav}} = 3 \cdot w_o^2 \cdot c_3 \cdot b_x (I^* c_3 \cdot b)$$

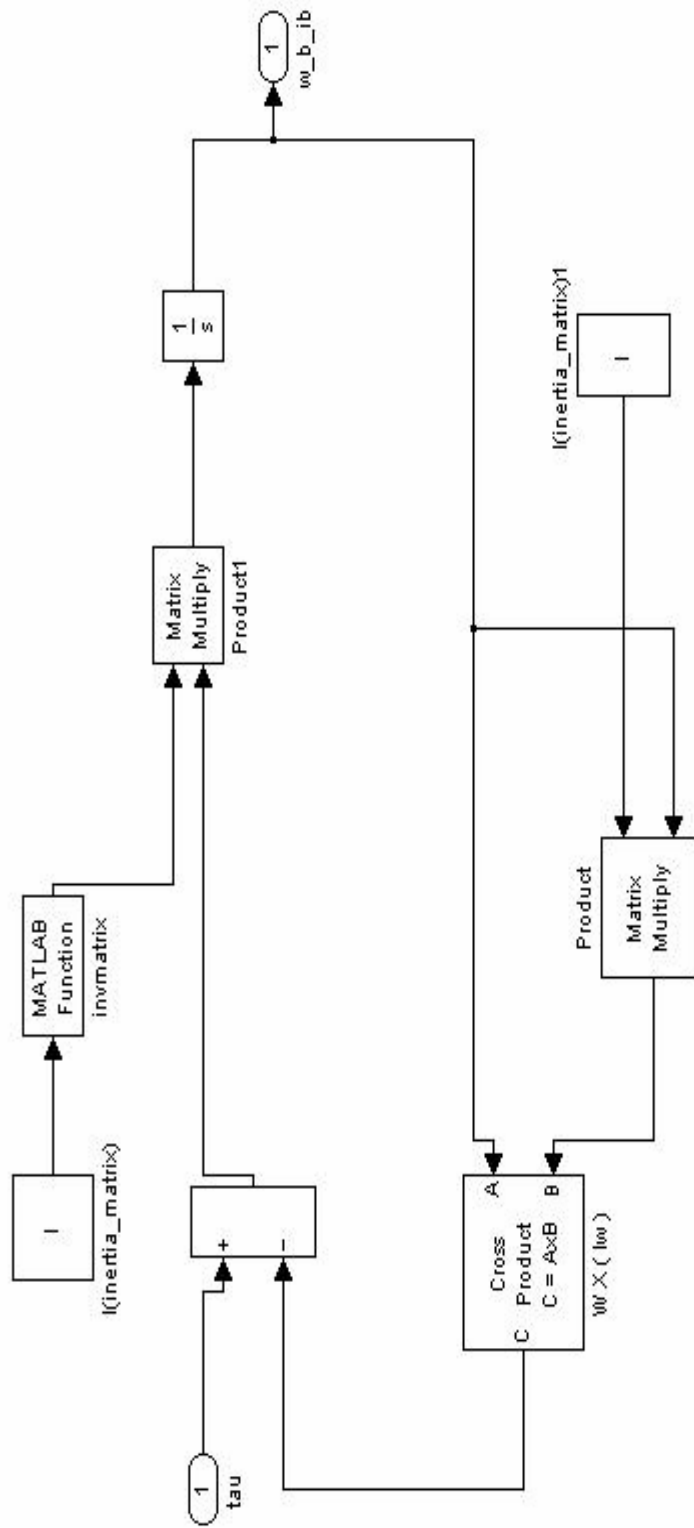
## Magnetic Torquers Model



# Satellite Nonlinear Dynamics



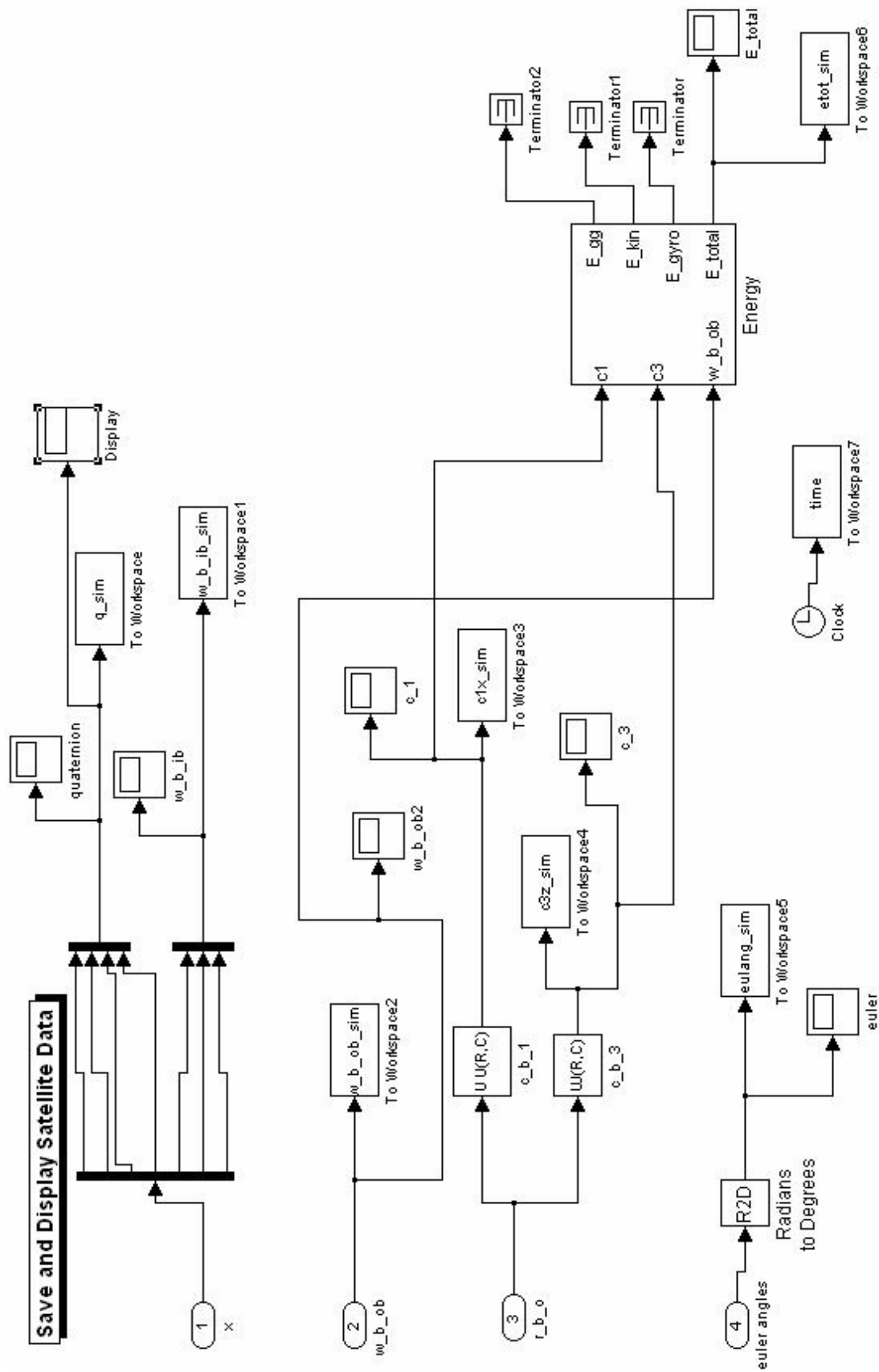
**Dynamics**



**Dynamics  $I.w \ b \ ib \ dot+s(w \ b \ ib).I.w \ b \ ib=T \ b$**

**Dynamics  $[T \ b-s(w \ b \ ib).I.w \ b \ ib]/I=w \ b \ ib \ dot$**





## **APPENDIX D**

### **CD CONTENT**

- LINEAR QUADRATIC REGULATOR SIMULINK MODELS AND MATLAB CODES
- LINEAR CONTROLLER SIMULINK MODELS AND MATLAB CODES